

INELASTIC DEFORMATION OF METALS AND STRUCTURES
UNDER DYNAMIC AND QUASI-STATIC CYCLIC LOADING

Final Technical Report



A.M. Eleiche

May 1984

Accession For	
NTIS GRA&I	<input checked="" type="checkbox"/>
DTIC TAB	<input type="checkbox"/>
Unannounced	<input type="checkbox"/>
Justification	
By	
Distribution/	
Availability Codes	
Dist	Avail and/or Special
A-1	

United States Army

EUROPEAN RESEARCH OFFICE OF THE U.S. ARMY

London England

CONTRACT NUMBER DAJA37-81-C-0236

Faculty of Engineering
Cairo University

Approved for public release; distribution unlimited

DTIC
ELECTE
AUG 29 1985
S D E

INELASTIC DEFORMATION OF METALS AND STRUCTURES
UNDER DYNAMIC AND QUASI-STATIC CYCLIC LOADING

by

A.M. Eleiche

ABSTRACT

In Part I of the present investigation, the modified version of the torsional split Hopkinson bar apparatus was further exploited to generate new data bases for OFHC copper and mild steel related to their stress-strain characteristics at ambient temperature under sequential reverse loading at impact strain rates, and different large values of the constant cyclic strain amplitude. The observed response was compared with that obtained under similar but quasi-static strain rate conditions. All data were evaluated in terms of various Bauschinger effect parameters. It is shown that the common practice of using quasi-static reverse loading characteristics in the analysis of problems where impact strain rates are predominant can yield to an overly safe and non-economical design, particularly if strain rate sensitive materials are being used. As expected, the present data do not conform with the predictions of classical plasticity theories, since experimental conditions involved essentially large, high strain-rate and adiabatic deformations. An examination of the currently widening literature on advanced constitutive equations for metals through many of the recent comparative reviews seems to indicate that the theories of Bodner and associates and of Cernocky and Krempl offer the greatest promises for modeling the present data. Further in-depth studies in that direction are being recommended.

In Part II, the problem of the simple thick-walled tube subjected to steady internal pressure and cyclic thermal gradient was investigated. A new numerical procedure was constructed to solve the same problem. The validity of this procedure was extensively verified through comparisons with available analytical solutions based on the kinematic hardening assumption for an elastic-linearly hardening tube material and the uniaxial model

of the tube. This numerical technique is further elaborated to accomodate the isotropic hardening rule and to utilize a more generalized biaxial tube model. This model is found to be more accurate and superior to the uniaxial model being widely used in similar analyses.

FOREWORD

This technical report was prepared by Professor A.M. Eleiche of the Department of Mechanical Design and Production, Faculty of Engineering, Cairo University, Egypt. The work reported herein was supported, in part, by the European Research Office of the U.S. Army, London, England, under contract number DAJA37-81-C-0236.

The report summarizes briefly the work detailed in the previous first and second annual reports, dated May 1982 and May 1983, respectively. More emphasis and full accounts are given on new results and findings in the two main research areas supported by the contract, namely: (a) material characterization of copper and mild steel under sequential reversed torsional impact and quasi-static loading at ambient temperature, and (b) ratchetting of pressurized tubes subjected to radial cyclic thermal gradient. These results are original and may be regarded as a new contribution to the field of cyclic behavior of materials and structures.

The author would like to express his appreciation for the fruitful discussions held with Dr. M.M. Megahed, who left the Department on a leave of absence after his involvement for the first two years as co-principal investigator in the project.

The author is also grateful to Mr. M.M. Mostafa El-Kady, Mr. A.F. Bastawros and Mr. M.A. El-Kabbany, graduate students in the Department, for their assistance in the various stages of the experimental work, the numerical computations and the preparation of this report.

TABLE OF CONTENTS

<u>SECTION</u>	<u>PAGE</u>
GENERAL INTRODUCTION	1
<u>PART I - Behavior of OFHC Copper and Mild Steel Under Sequential Reversed Torsional Loading at Ambient Temperature</u>	
1 INTRODUCTION	6
2 EXPERIMENTAL DETAILS	7
2.1 Description of Apparatus	7
2.2 Materials and Specimens	9
2.3 Testing Program	9
2.4 Testing Procedure	12
2.5 Typical Test Records	12
2.6 Data Reduction	13
3 RESULTS AND DISCUSSIONS	15
3.1 Copper	15
3.1.1 Sequential reverse loading response	15
3.1.2 Analysis of behavior in terms of B.E. parameters	17
3.2 Steel	19
3.2.1 Sequential reverse loading response	19
3.2.2 Analysis of behavior in terms of B.E. parameters	20
3.3 Application of Anisotropic Hardening Theories to Results	21
3.4 Identification from the Literature of Constitutive Equations Suitable for Modeling Bauschinger Effects in Metals	24
4 CONCLUSIONS AND RECOMMENDATIONS	27
5 REFERENCES	30
<u>PART II - Ratchetting of Pressurized Tubes Subjected to Radial Cyclic Thermal Gradient</u>	
1 INTRODUCTION	80
2 BIAxIAL FORMULATION OF THE TUBE PROBLEM	81
2.1 Generalized Plane Strain Formulation	81
2.2 Plasticity Relations	83

<u>SECTION</u>	<u>PAGE</u>
2.2.1 Kinematic hardening	83
2.2.2 Isotropic hardening	86
3 NUMERICAL PROCEDURE	87
3.1 Determination of the Temperature Level at which First Yield Occurs	87
3.2 Continuation of Thermal Load Incrementation to Determine the Elastic Plastic Solution	88
4 RESULTS AND DISCUSSIONS	93
4.1 Choice of Numerical Experiments	93
4.2 Results	95
4.2.1 Kinematic hardening results	95
4.2.2 Isotropic hardening results	98
4.2.3 Results for load conditions used in Corum's test	99
5 CONCLUSIONS AND RECOMMENDATIONS	103
6 REFERENCES	107

LIST OF TABLES

<u>TABLE</u>		<u>PAGE</u>
<u>PART I</u>	<u>Behavior of OFHC Copper and Mild Steel Under Sequential Reversed Torsional Loading at Ambient Temperature</u>	
I	Composition of materials tested	34
II	List of specimens tested	35
III	Oscilloscope records calibration values	36
IV	Calculated values of K and n in the equation $\tau = K \gamma^n$ for copper	37
V	List of some parameters representative of Bauschinger effect and hardening for reverse loading on copper	38
VI	List of some parameters representative of Bauschinger effect and hardening for sequential loading on copper (for the 2nd and 4th loadings)	39
VII	Calculated values of K and n in the equation $\tau = K \gamma^n$ for steel	37
VIII	List of some parameters representative of Bauschinger effect and hardening for reverse loading on steel	40
IX	List of some parameters representative of Bauschinger effect and hardening for sequential loading on steel (for the 2nd and 4th loadings)	41
X	Comparison of Uniaxial Models of Viscoplastic Constitutive equations (Beek, Allen and Milly /50/)	42
XI	Ability of viscoplastic constitutive equations to model certain phenomena (Beek, Allen and Milly /50/)	44
XII	Required material parameter characterization in various viscoplastic constitutive equations (Beek, Allen and Milly /50/)	45
<u>PART II</u>	<u>Ratchetting of Pressurized Tubes Subjected to Radial Cyclic Thermal Gradient</u>	
I	Internal pressure - temperature difference combinations and corresponding increment of temperature difference and expected mode of behavior used for inspecting the uniaxial program with kinematic hardening assumption	108
II	Internal pressure - temperature difference combinations and corresponding increments of temperature difference used in the uniaxial program with isotropic hardening assumption	108
III	Summary of numerical results for the load conditions (p = 700 psi and $\Delta T = 167^\circ F$) used by Corum in his tube ratchetting tests.	108

LIST OF ILLUSTRATIONS

<u>FIGURE</u>		<u>PAGE</u>
<u>Part I</u>	<u>Behavior of OFHC Copper and Mild Steel Under Sequential Reversed Torsional Loading at Ambient Temperature</u>	
1	Schematic drawing of torsional SHB with insets showing various details	46
2	Closeup of CRO and related instrumentation	47
3	Schematic drawing of quasi-static torsional apparatus	48
4	General view of quasi-static torsional apparatus	48
5	General view of quasi-static rotational drive unit	49
6	Overall view of the instrumentation used in quasi-static testing	49
7	Configuration and nominal dimensions of test specimens	50
8	Characteristic x-t diagrams showing locations of clamp in positions I, II and III and corresponding useful pulse durations	51
9	Experimental verifications of calculated useful pulse durations for the clamp at positions I, II and III, using a dummy specimen	52
10	Flow chart summarizing the procedure used in sequential reverse impact loading tests on the SHB	53
11	Typical records of quasi-static reverse loading on copper specimens	54
12	Typical records of quasi-static reverse loading on steel specimens	54
13	Typical oscilloscope records of impact reverse loading on copper specimens,	55
14	Typical oscilloscope records of impact reverse loading on steel specimens	56
15(a)	Stress-strain curves for copper under sequential reverse loading at $\dot{\gamma} = 1100 \text{ s}^{-1}$, for a constant strain amplitude $\gamma_0 \sim 0.45$	57
15(b)	Stress-strain curves for copper under sequential reverse loading at $\dot{\gamma} = 1100 \text{ s}^{-1}$, for a constant strain amplitude $\gamma_0 \sim 0.60$	58

<u>FIGURE</u>		<u>PAGE</u>
15(c)	Stress-strain curves for copper under sequential reverse loading at $\dot{\gamma} \sim 1100 \text{ s}^{-1}$, for a constant strain amplitude $\gamma_0 \sim 0.97$	59
16(a)	Stress-strain curves for copper under sequential reverse loading at $\dot{\gamma} \sim 550$, for a constant strain amplitude $\gamma_0 \sim 0.24$	60
16(b)	Stress-strain curves for copper under sequential reverse loading at $\dot{\gamma} \sim 550 \text{ s}^{-1}$, for a constant strain amplitude $\gamma_0 \sim 0.322$	61
16(c)	Stress-strain curves for copper under sequential reverse loading at $\dot{\gamma} \sim 550 \text{ s}^{-1}$, for a constant strain amplitude $\gamma_0 \sim 0.508$	62
17(a)	Stress-strain curves for copper under forward and reverse loading at $\dot{\gamma} \sim 10^{-3} \text{ s}^{-1}$, for a constant strain amplitude $\gamma_0 \sim 0.43$	63
17(b)	Stress-strain curves for copper under forward and reverse loading at $\dot{\gamma} \sim 10^{-3} \text{ s}^{-1}$, for a constant strain amplitude $\gamma_0 \sim 0.76$	63
17(c)	Stress-strain curves for copper under forward and reverse loading at $\dot{\gamma} \sim 10^{-3} \text{ s}^{-1}$, for a constant strain amplitude $\gamma_0 \sim 1.1$	63
18	Definition of terms used in describing the Bauschinger effect phenomenon	64
19	Variation of reverse yield stress, τ_{yr} , and Bauschinger stress, τ_B , for copper, with strain amplitude, γ_0 , for various strain rates	65
20	Variation of Bauschinger effect indicator, $\tau_B/\Delta\tau$, for copper, with strain amplitude, γ_0 , for various strain rates	65
21	Variation of reverse yield stress, τ_{yr} , and Bauschinger stress, τ_B , for copper, with cumulative strain, γ_c , for various strain rates	66
22	Variation of Bauschinger effect indicator, $\tau_B/\Delta\tau$, for copper, with cumulative strain, γ_c , for various strain rates	66
23(a)	Stress-strain curves for steel under sequential reverse loading at $\dot{\gamma} \sim 760 \text{ s}^{-1}$, for a constant strain amplitude $\gamma_0 \sim 0.262$	67

<u>FIGURE</u>		<u>PAGE</u>
23(b)	Stress-strain curves for steel under sequential reverse loading at $\dot{\gamma} \sim 760 \text{ s}^{-1}$, for a constant strain amplitude $\gamma_o \sim 0.46$	68
23(c)	Stress-strain curves for steel under sequential reverse loading at $\dot{\gamma} \sim 760 \text{ s}^{-1}$, for a constant strain amplitude $\gamma_o \sim 0.65$	69
24(a)	Stress-strain curves for steel under sequential reverse loading at $\dot{\gamma} \sim 350 \text{ s}^{-1}$, for a constant strain amplitude $\gamma_o \sim 0.15$	70
24(b)	Stress-strain curves for steel under sequential reverse loading at $\dot{\gamma} \sim 350 \text{ s}^{-1}$, for a constant strain amplitude $\gamma_o \sim 0.25$	71
24(c)	Stress-strain curves for steel under sequential reverse loading at $\dot{\gamma} \sim 350 \text{ s}^{-1}$, for a constant strain amplitude $\gamma_o \sim 0.312$	72
25(a)	Stress-strain curves for steel under forward and reverse loading at $\dot{\gamma} \sim 10^{-3} \text{ s}^{-1}$, for a constant strain amplitude $\gamma_o \sim 0.135$	73
25(b)	Stress-strain curves for steel under forward and reverse loading at $\dot{\gamma} \sim 10^{-3} \text{ s}^{-1}$, for a constant strain amplitude $\gamma_o \sim 0.26$	73
26	Variation of reverse yield stress, τ_{yr} , and Bauschinger stress, τ_B , for steel, with strain amplitude, γ_o , for various strain rates	74
27	Variation of Bauschinger effect indicator, $\tau_B/\Delta\tau$, for steel, with strain amplitude, γ_o , for various strain rates	74
28	Variation of reverse yield stress, τ_{yr} , and Bauschinger stress, τ_B , for steel, with cumulative strain, γ_c , for various strain rates	75
29	Variation of Bauschinger effect indicator, $\tau_B/\Delta\tau$, for steel, with cumulative strain, γ_c , for various strain rates	75
30	Comparison between the measured Bauschinger effect and predictions from kinematic hardening theory	76
31	Effect of prestrain amplitude on the Bauschinger parameter m/τ_y	77

FIGUREPAGEPART II - Ratchetting of Pressurized Tubes Subjected to Radial
Cyclic Thermal Gradient

1	Total thermal gradient incrementation	109
2	Simplified flow chart for the biaxial program	109
3	Full interaction diagram for a tube made of 304 SS with kinematic hardening assumption and bilinear temperature distribution ($\beta = 0.0253$, $h = 0.328$)	110
4	Cyclic stress distributions and strain growth for $p = 100$ psi $\Delta T = 50^{\circ}\text{F}$ (Regime S)	110
5	Cyclic stress distributions and strain growth for $p = 100$ psi and $\Delta T = 200^{\circ}\text{F}$ (Regime F_1)	111
6	Cyclic stress distributions and strain growth for $p = 100$ psi and $\Delta T = 300^{\circ}\text{F}$ (Regime F_2)	111
7	Cyclic stress distribution and strain growth for $p = 100$ psi and $\Delta T = 100^{\circ}\text{F}$ (Regime F_3)	112
8	Cyclic stress distributions for $p = 900$ psi and $\Delta T = 50^{\circ}\text{F}$ (Regime R_1)	112
9	Cyclic stress distributions for $p = 200$ psi and $\Delta T = 300^{\circ}\text{F}$ (Regime R_2)	112
10	Cyclic stress distributions for $p = 900$ psi and $\Delta T = 100^{\circ}\text{F}$ (Regime R_3)	113
11	Cyclic stress distributions for $p = 900$ psi and $\Delta T = 300^{\circ}\text{F}$ (Regime R_4)	113
12	Cumulative strain growth for the different ratchetting regimes	113
13	Cyclic stress distributions for $p = 700$ psi and $\Delta T = 167^{\circ}\text{F}$ (K.H. - uniaxial version with $h = 0.328$)	114
14	Cyclic stress distributions for $p = 700$ psi and $\Delta T = 167^{\circ}\text{F}$ (K.H. - uniaxial version with $h = 0$)	114
15	Ratchet strain growth for $p = 700$ psi and $\Delta T = 167^{\circ}\text{F}$ (K.H. - uniaxial version for both $h = 0$ and $h=0.328$)	115
16	Cyclic stress distribution for $p = 700$ psi and $\Delta T = 167^{\circ}\text{F}$ (I.H. - uniaxial version with $h=0.328$)	115
17	Cyclic stress distributions for $p = 700$ psi and $\Delta T = 167^{\circ}\text{F}$ (I.H. - uniaxial version with $h = 0$)	116
18	Ratchet strain growth for $p = 700$ psi and $\Delta T = 167^{\circ}\text{F}$ (I.H. - uniaxial version for both $h=0$ and $h = 0.328$)	116
19	Cyclic hoop stress distributions for 700 psi/167°F (K.H. - biaxial version with $h = 0.328$)	117

<u>FIGURE</u>		<u>PAGE</u>
20	Cyclic hoop stress distribution for 700 psi/167°F (K.H. - biaxial version with $h = 0$)	117
21	Ratchet hoop strain growth for 700 psi/167°F for both K.H. and I.H. biaxial programs with $h = 0$ and 0.328	118
22	Uniaxial, biaxial and experimental results for $p = 700$ psi and $\Delta T = 167^\circ\text{F}$	118
23	Typical stress-strain curve for reversed yielding as predicted by various hardening theories	119
24	Mroz's hardening (Mroz /10/)	119
25	Dafalias and Popov model (Dafalias and Popov /12/)	119

LIST OF SYMBOLS

PART I - Behavior of OFHC Copper and Mild Steel Under Sequential Reversed Torsional Loading at Ambient Temperature

c_o	elastic shear wave speed
d_s	specimen mean diameter
G_b	shear modulus of bar material
J_b	polar moment of area of bar
J_s	polar moment of area of specimen
K	strain-hardening coefficient
l_s	specimen gage length
m	Bauschinger effect constant
n	strain-hardening exponent
r_b	bar radius
r_s	specimen mean radius
T	torque
T_s	stored torque
t	wall thickness; also, time
t_s	specimen wall thickness
t_u	useful loading time of incident pulse
x	Lagrangian coordinate along the bar length
γ	engineering shear strain
γ_o	total constant strain amplitude in cyclic loading
γ_s	total specimen shear strain
$\dot{\gamma}$	shear strain rate
$\dot{\gamma}_s$	specimen shear strain rate
θ	angle of rotation
τ	shear stress
τ_s	specimen shear stress
τ_y	yield shear stress
τ_o	flow stress at end of prestraining
τ_{yr}	reverse yield stress
τ_B	Bauschinger stress
ϕ	elastic shear strain pulse
ϕ_i, r, t	incident, reflected and transmitted

PART II - Ratchetting of Pressurized Tubes Subjected to Radial Cyclic Thermal Gradient

A	Cross-sectional area
a	Inner radius of plastic front
a'	Plastic front
b	Outer radius of plastic front
D	Mean diameter
E	Young's modulus
E	Full elasticity region
F	Reversed plasticity region
f	Function of change of yield stress with temperature
h	Bilinear intersection
$I_{0,1,2,3}$	Integrals appearing in bilinear formulations
I.H.	Isotropic hardening
K	Parameter of strain hardening
K.H.	Kinematic hardening
M	Mechanical load parameter
n	Number of cycles
P	Axial force
p	Internal pressure
R	Mean radius or ratchetting region
S	Shakedown region
$S_{r,\theta,z}$	Deviatoric stresses
T	Temperature
t	Thickness
u	Radial displacement
x	Radial distance
y	Plastic front
z	Plastic front
α	Coefficient of linear thermal expansion
$\alpha_{r,\theta,z}$	Coordinates of yield surface
β	Strain hardening coefficient
γ	Area ratio of the two bars
ΔT	Full temperature difference
ΔT	Increment of temperature difference
ΔT_1	Temperature difference in the equivalent uniaxial model

ϵ	Axial strain
ϵ^P	Plastic strain
$\bar{\epsilon}^P$	Equivalent plastic strain
ϵ_R^P	Plastic ratchet strain
ν	Poisson's ratio
η	Length ratio of the two bars
θ	Thermal load parameter
σ	Axial stress
$\bar{\sigma}$	Equivalent stress
σ_p	Stress due to mechanical load
σ_t	Equivalent thermal stress
σ_y	Yield stress

GENERAL INTRODUCTION

Rigorous understanding of the effects of impact loading on the mechanical response of materials and structures is essential for the optimum design and safe operation of many sophisticated engineering systems and components, such as industrial high-energy-rate fabrication processes and nuclear reactor containments.

Extensive data are available at present on the dynamic behavior of most metals in uniaxial tension, compression, torsion and pure shear, when they are subjected to a variety of loading conditions, ranging from those characterised by monotonic constant strain rates, to those involving forward or reverse strain-rate jumps of several orders of magnitude. What is missing in the present data banks, however, is detailed information concerning the mechanical response under reversed sequential cyclic loading at impact strain rates. Such data are badly needed for engineering design purposes, and also to help in the formulation of proper constitutive equations and the accurate modeling of deformation processes.

On the other hand, much effort has been directed in recent years towards an understanding of the mechanism of cyclic inelastic deformation of structures. Whilst it has been realized that purely elastic design of structures is both wasteful of material and often impractical, the presence of cyclic inelastic strains (ratchetting) may lead to the failure of structures by excessive distortion or low cycle fatigue. This is particularly the case in components subjected to continuous mechanical loading together with cyclic thermal loading, such as the tubular fuel cans used in liquid metal fast breeder reactors, aeroplane wings and off-shore structures. Present design codes require that a design at specified operating conditions shall be free from ratchetting, or if ratchetting does occur, that the strain accumulation shall be less than a specified limit during the expected operating lifetime of the component.

It is against this background that the research program carried out under the present contract was established. Two main objectives were identified:

- (a) The novel adaptation of a well-established impact testing technique to the generation of new data bases for OFHC copper and mild steel regarding their behavior under sequential reverse loading. This is followed by an examination of the results vis-a-vis the classical plasticity theories, and the more realistic constitutive equations recently proposed in the literature.
- (b) The study of ratchetting in the simple but practical example of a pressurized tube subjected to radial cyclic thermal gradient, as affected by the model used to describe its material cyclic behavior.

Various activities were performed in the three years of the contract to achieve these two objectives. These are detailed in the previous annual reports, as well as in the current final one.

The first annual report, dated May 1982, presented a detailed description of the modified split Hopkinson torsional bar designed and manufactured, partly under the present contract. The performance, trouble shooting and refinements of this apparatus were also delineated. Moreover, results collected with this new testing facility on an aluminium alloy were presented and analysed. The report also included the new generalized plane-strain formulation proposed for analyzing the case of a thick walled-cylinder subjected to a steady internal pressure and a cyclic temperature gradient. A review of cyclic phenomena in metals indicated that the kinematic and isotropic hardening hypotheses provide extreme limits of material modeling, and therefore may be used in the analysis of mechanical components subjected to cyclic loading. Results obtained with the kinematic hardening assumption for 304 stainless steel were also provided.

The second annual report, dated May 1983, presented a variety of results obtained in the area of analysis of structures subjected to cyclic loading. First, the problem the tube under internal pressure and cyclic non-linear thermal gradient was investigated using a uniaxial model. Numerical results were also presented for kinematic and isotropic hardening theories of behavior. The previously proposed generalized plane-strain formulation was also used together with kinematic hardening assumption, and results compared for this biaxial model with those of the uniaxial one, as well as with experimental

results. Next, a study of kinematic hardening analysis of ratchet strain in the "Pulley Test" was presented. This is used to simulate the uniaxial model of a thin tube subjected to combined internal pressure and cyclic thermal stress across its wall. Finally, the concept of the reference stress method (RSM) and its applications in cyclic plasticity analysis were presented.

The present final report is divided in two parts, and provides additional new results collected under the contract. In Part I, the current status of the modified split Hopkinson torsional bar is briefly described. Results collected for OFHC copper and mild steel are then presented and discussed. These are contrasted with predictions of classical plasticity theories. Recently proposed constitutive equations are also examined to identify those most probably fitting the present experimental data. In Part II, the biaxial model of the thick walled tube previously studied is being considered together with isotropic hardening theory, and numerical results compared with those previously obtained. Using the biaxial model and the developed numerical method, the full solution map for any specific problem can be numerically constructed for any given form of temperature distribution and any well mathematically-founded hardening rule.

PART I

Behavior of OFHC Copper and Mild Steel Under Sequential Reversed
Torsional Loading at Ambient Temperature

SECTION 1

INTRODUCTION

Conventional-type apparatus, in which the stress may vary considerably along the length of the specimen due to inertia effects, cannot be used in the impact range of strain rates. The most popular experimental device which can meet the high-speed test requirements is the split-Hopkinson-bar (SHB) apparatus. Over the past two decades, the SHB has been used repeatedly for testing materials at fairly constant strain rates, and also adapted successfully to study history effects by performing incremental strain-rate change tests/1-3/.

For cyclic loading at impact strain rates, the SHB needs further modifications. For small plastic straining in the tension-compression or torsional mode, the adaptation of the SHB is simply based on the one-dimensional elastic wave propagation theory/4-6/. This can be done by introducing suitable discontinuities at specific locations along the testing bar system which cause reflections of proper magnitudes in the travelling elastic waves, and consequently unloading and reverse loading in the test specimen.

On the other hand, subjecting a material specimen in the SHB to reversed sequential loading causing large plastic strains is not a straightforward procedure. In the tension-compression mode, two major difficulties exist. The first is related to the specimen itself, where a particular geometry is usually required for the case of tension which drastically differs from that required for compression. The second difficulty relates to the two input and output bars which should be suitably modified to accommodate the corresponding specimen. Also, in this t-c mode, only a single sequence is possible. Thus, a specimen can be first loaded dynamically in tension. Thereafter, compression tests are conducted on suitable wafers machined from this previously strained tensile specimen. This procedure is accompanied by two inherent limitations, namely: (a) the long elapsed time necessary between loadings, and which is usually of the order of a few hours at least, and (b) the relatively small values of plastic strain involved to ensure uniform deformation, away from necking in tension during prestraining, and from barrelling in compression during the reverse straining.

It seems timely at this point to list some of the essential general requirements needed for the generation of relevant data on material behavior under cyclic loading at impact strain rates. These are: (a) the development of a testing system capable of both forward and reverse loading at fairly constant strain rates and up to large values of strain, and (b) the capability of subjecting the same specimen to load reversals of small or large strain amplitudes within a reasonable amount of elapsed time. These considerations automatically favour the torsion of thin-walled tubes as the ideal mode of loading. This, in addition, offers the following advantages:

1. The achievement of a homogeneous stress state and a large range of uniform deformation without significant change in the specimen shape.
2. The performance of forward and reverse loading on the same specimen, and its sequential repetition for more than one cycle, up to fracture.
3. For dynamic testing, the torsional version of the SHB has proved its superiority^{2,7/}, particularly since many of the difficulties which accompany the axial versions are eliminated.

Satisfactory dynamic cycling testing of materials can therefore be accomplished by twisting a tubular specimen at an impact strain rate in a torsional SHB, up to a given strain, and unloading. The same specimen can then be retwisted in the reverse direction by simply reversing the direction of the loading torsional wave propagating in the system from clockwise to anti-clockwise or vice-versa. This procedure may then be repeated again and again on the same specimen until fracture.

SECTION 2

EXPERIMENTAL DETAILS

2.1 Description of Apparatus

In its final form, the torsional SHB system designed and manufactured under the present contract for reversed sequential testing of materials is shown in the schematic drawing of Fig. 1. Design considerations and complete description of each one of the system components as well as related instrumentation, all in their preliminary status, have been presented in full details elsewhere^{8,9/}. To avoid repetition, therefore, only a brief description is given here, with emphasis being made on the main modifications introduced on

the system since then, and on the main adjustments found necessary to carry out the present experimental program.

The apparatus essentially consists of the two input and output bars sandwiching the specimen, a frictional clamping device, an actuator arrangement and a slow rotational drive unit. The actuator arrangement is of a particularly novel design and represents the salient feature of the apparatus. It allows the rotation of the input bar in either the clockwise or anticlockwise direction. Dynamic torsional straining is achieved by the release of a pre-stored torque pumped by the actuator into a portion of the input bar. One-half of this stored torque travels down the input bar to load the specimen, while the other half, after reflection at the fixed end of the input bar, unloads it. The loading incident wave, characterized by a short rise time and a constant amplitude thereafter, is partly reflected and partly transmitted at the specimen. The axial position of the frictional clamp controls the useful loading duration of the incident wave, and consequently determines the amount of straining a specimen may be subjected to before being unloaded.

The stored torque in the input bar was measured by an electrical resistance strain-gage bridge cemented to its surface. The bridge output was fed to a digital hybrid multimeter calibrated to measure torque. On the other hand, the incident and transmitted waves were measured by similar torque strain-gage bridges on the input and output bars, respectively. Outputs of these two bridges were fed to a Tektronix type 5111A storage oscilloscope, equipped with type 5A26 dual differential amplifier and type 5B12N dual time base. Displays on the oscilloscope were recorded photographically on type 665 Polaroid film using a type C-5C Tektronix camera (Fig. 2).

Quasi-static reversed sequential cyclic loading could be achieved using the same bars. Such configuration is particularly useful when performing tests involving a change in the strain rate. In the present work, however, a separate pair of shorter bars was used. As shown in Figs. 3 and 4, these bars were mounted on separate supports at the distal end of the SHB base. The inner end of each bar was provided with three jaws to engage with similar ones on a specimen holder in order to facilitate the mounting of the specimen assembly. The far end of the input bar was keyed to a quasi-static rotational drive unit, while the far end of the output bar was rigidly fixed in a

frictional clamp. The drive unit consisted of a 1-HP single-phase electric motor having a fixed speed of 1440 rpm, two compact speed-reduction units of 1:30 fixed reduction ratio each, a 4-speed gearbox of 1:2.66, 1:2, 1:1.6 and 1:1 reduction ratios, and an electro-magnetic brake. These components are shown separately in Fig. 5.

During a test, the torque and angular rotation were continuously plotted on an x-y recorder. This was done by feeding the output signals of a torque strain-gage bridge and a differential transformer (DCDT) to the vertical and horizontal channels of the recorder, respectively. By proper scaling, this plot was calibrated to provide a stress-strain curve for the specimen (Fig. 6). Elastic deformation of the specimen assembly and the loading system was also determined and deducted from the overall deformation during each test in the strain calculation process.

2.2 Materials and Specimens

As reported previously/8,9/, the present apparatus has been used successfully to investigate the dynamic hysteresis loop and the dynamic Bauschinger effect in an aluminum alloy corresponding very closely to American designation Al 6061.

In the present study, two other materials of practical importance and of different crystallographic structure were chosen, namely: Oxygen-free high-conductivity (OFHC) copper, and mild steel. Compositions of these materials are given in Table I. After machining to the nominal configuration shown in Fig. 7, each specimen was measured and its actual dimensions recorded. Mild steel specimens were tested without further heat treatment, while all copper specimens were annealed in a vacuum of 10^{-3} to 10^{-4} torr at 370°C for 1.5 hr. Temperature within the furnace did not vary by no more than $\pm 3^{\circ}\text{C}$ from one location to another. The furnace was then turned off and the specimens allowed to cool with the door closed. Average grain densities, as measured from microscopic examination, were found to be 161 mm^{-2} in annealed copper specimens and 266 mm^{-2} in steel specimens.

2.3 Testing Program

A main objective of the present research program was to collect experimental data on the sequential reversed loading behavior of OFHC copper and mild

steel, as affected by strain rate. Therefore, in designing the corresponding testing program, the following facts had to be accounted for :

- (a) Three different strain rates should be investigated, one quasi-static and two dynamic.
- (b) In using the SHB apparatus for dynamic torsional testing, it can be shown that the following simple expressions are reliable for calculating the specimen stress, strain rate and strain /10,7/:

$$\tau_s = G_b (r_s/r_b)(J_b/J_s) \phi_t \quad (1a)$$

$$\dot{\gamma}_s = 2 (r_s/r_b)(c_o/l_s) \dot{\phi}_r \quad (1b)$$

$$\gamma_s = 2 (r_s/r_b) (c_o/l_s) \int \dot{\phi}_r dt = \int \dot{\gamma}_s dt \quad (1c)$$

where

$$\dot{\phi}_i = \dot{\phi}_r + \dot{\phi}_t. \quad (2)$$

Since the relative magnitudes of ϕ_i , ϕ_r and ϕ_t depend essentially on the physical properties of the material specimen, it is therefore expected that, for a given specimen geometry and a given ϕ_i (i.e. fixed value of stored torque in the input bar), upon sequential loading in the same or reverse direction:

- (i) the same strain rate and total strain will be repeatedly achieved in a non strain-hardening material specimen.
- (ii) slightly decreasing values of strain rate and total strain amplitude will sequentially take place in a strain-hardening material. In the latter case, however, a slight incremental increase in the stored torque (and hence in ϕ_i) will keep the strain rate and total strain constant upon repeated loading. Hence, with the SHB used in the present investigation, sequential reverse loading of fixed strain rate and strain amplitude can always be performed.
- (c) For a given specimen strain rate, it is also important to study the effects of changing the value of the fixed strain amplitude characterizing the series of reverse sequential impacts. This can only be achieved in the present apparatus by changing the total useful duration of the loading pulse through a physical change in the axial location of the friction clamp along the system, as shown in Fig. 8. Upon reaching the specimen,

the reflected waves caused by the fixed hydraulic actuator terminate the useful duration of the loading wave and force the specimen to unload from the maximum stress already reached.

In the present work, three different locations were chosen for the friction clamp. These are designated as Position I, II and III, yielding a useful loading time in the incident wave of 530, 770 and 1100 μ s respectively. Experimental verifications of these values are shown in the records of Figs. 9 (a), (b) and (c) corresponding to the three clamp positions, respectively. These records were obtained by using a dummy specimen between the two bars and simultaneously measuring the travelling pulses at the input bar strain gage station (top trace) and the output bar strain gage station (bottom trace).

- (d) Changing the strain rate in the present setup can be achieved simply by increasing the amount of stored torque in the input bar. Further complications and disturbances were found to accompany this procedure, however, which forced the use of a constant value, within the range of 13.3 - 14.5 kgm, for the stored torque in all dynamic testing. Instead, the strain, where as indicated by Eq. (1b), a higher strain rate is induced by a smaller gage length and vice versa. Two different values of nominal specimen gage length were used, namely 1.1 and 3.0 mm.

Based on the above considerations, the following characteristics accompanied the dynamic testing program of the present research:

- Stored torque : 13.3 - 14.5 kgm
- Axial position of clamp from actuator end : 75, 108 and 155 cm
- Corresponding useful duration of incident wave : 530, 770 and 110 μ s
- Nominal specimen gage length : 1.1 and 3.0 mm
- Type of test : Forward, reverse, forward, reverse;
alternatively referred to as (+), (-), (+), (-).
- Testing temperature : 22°C.

All specimens used in the present work, together with their nominal and actual dimensions, as well as the test conditions they were subjected to, are listed in Table II.

2.4 Testing Procedure

In each dynamic test, the procedure involved many steps which may be grouped into three main phases : (a) setup preparation involving mainly the fixation of the friction clamp at the proper axial position, the mounting of the specimen between the two bars with Araldite epoxy adhesive, and the adjustment of the hydraulic actuator; (b) instrumentation checkup; and (c) specimen loading. The two last phases are repeated on the same specimen for further loading in the reverse direction, according to the previous program. The whole testing procedure is summarized in the flow chart of Fig. 10.

Quasi-static testing involved the separate fixation of the specimen in its holder with Araldite epoxy adhesive, and the fixation of this assembly to the pair of jaws of the two short input and output bars. The distal end of the output bar is then clamped, the instrumentation checked and the electric motor started to load the specimen at the required slow speed to a pre-selected plastic strain in the forward direction. The clamp is then opened to release the stored torque in the system, re-tightened, and the torque re-applied at the same rotational speed to the same value of plastic strain in the reverse direction. This procedure is then repeated any number of times as required, with the torque versus angle of rotation at the motor end of the input bar being plotted on the x-y recorder, in each case.

2.5 Typical Test Records

2.5.1 Quasi-static loading

Figures 11 and 12 represent typical torque-twist angle records obtained on copper and steel, respectively. Each record was obtained on a separate specimen which was loaded in the forward direction up to a given value of strain, unloaded by the release of the friction clamp, then immediately reloaded at the same twisting rate in the opposite reverse direction. Ripples exhibited on the traces do not indicate intrinsic yield point behavior or material instabilities, but are essentially due to the relatively high amplification used on the x-y recorder. Traces were smoothed out upon data reduction.

Forward yielding of copper is very much undefined and seems to occur at very low torque. The reverse loading is characterised by a much higher slope of the elastic line and a sharper yield point than in forward loading. In

contrast, the forward yield of steel is more well defined, while the elastic behaviour has almost the same slope in reverse and forward loading.

2.5.2 Dynamic loading

A representative collection of dynamic test records, reduced in scale for ease in comparison, is presented in the matrix of Figs. 13 and 14 for copper and steel, respectively. Each matrix consists of 24 records. Any four records gathered together in one row are the results of testing on a single specimen in the following sequence: forward, reverse, forward, reverse. The first three rows correspond to dynamic testing at the same impact strain rate $\dot{\gamma}_1$, while they differ among themselves in the value of the constant strain amplitude, γ_0 , achieved in each of their four sequential loadings. These same three values of strain amplitude were also achieved in the tests represented by the records of the second set of three rows; the impact strain rate for this set, however, being smaller than $\dot{\gamma}_1$.

In all oscillograms, the upper trace shows the input bar gage signal (i.e. the incident and reflected torque), while the lower trace shows the output-bar gage signal (i.e. output torque). For all traces in both Figs. 13 and 14, the horizontal sweep was kept the same at 200 μ s/div. The vertical sensitivity for the upper traces shown in the four records in each row were identical, but smaller than that used for the lower traces in the same row. Traces of corresponding records in different rows, however, are not directly comparable, since the amplitudes obtained, besides being function of the oscilloscope settings, depend also on the excitation voltage of the strain gage bridges which, being provided by dry batteries, varied from one test to the other. Table III gives in detail the calibration of the vertical traces in all records. It should also be noted in Figs. 13 and 14 that, before each impact in the loading sequence, the positions of the baseline of the top and bottom traces were changed in order to accommodate the expected trace motion.

2.6 Data Reduction

2.6.1 Quasi-static response

In quasi-static testing, the elastic response of the system, apart from the specimen, was drawn as a straight line on the same torque-twist diagram obtained, whether in the forward or reverse loading, in order to give the

elastic-plastic specimen behavior. Shear stress was calculated from the relation:

$$\tau = T/2 \pi r^2 t_s, \quad (3)$$

whereas shear strains were calculated by measuring, at various values of the torque, offset twist values between the experimental total torque-twist plot and using the equation :

$$\gamma = \theta r / l_s. \quad (4)$$

It should be noted that throughout this report, "engineering" shear strains are quoted, i.e. twice the tensor values.

2.6.2 Dynamic response

In this case, oscilloscope records in each impact loading were analysed in terms of specimen stress, strain and strain rate following the usual technique for a SHB test. This is based on the assumption of uniform stress state in the short specimen gage length, which can be justified in particular when a torsional pulse of constant amplitude is applied as in the present apparatus.

Specimen stress-time behavior is usually determined from the transmitted pulse as measured on the output bar, while the strain rate-time characteristic, and consequently strain by integration, can be obtained from the reflected pulse if this can be completely measured on the input bar. As shown in Fig. 1, the strain-gage bridge on the input bar is positioned far enough from the specimen, so that a large proportion of the incident pulse can be measured and judged in quality before the reflected pulse from the specimen arrives at the gages. This incident pulse was always found to be of constant amplitude immediately following a short rise time, as can be seen from the oscilloscope traces shown previously in Figs. 9(a)-(c). Therefore, the amplitudes of the reflected pulse were calculated as the difference between the absolute values of the incident and transmitted pulses taken at coincident times. This eliminated the necessity of a separate direct measurement of the reflected pulse with another set of strain gages.

The analysis of the test records was carried out by using the standard expressions given by Eq. (1), relating shear stress, shear strain rate and shear strain to the incident and transmitted pulses; calibration being effected by using shunt resistances across the strain gauges/7/.

All calculations were performed on a Sinclair ZX Spectrum desk-top calculator equipped with an Alpha 32 printer. The computer program used is very similar to that used previously and listed elsewhere/11/.

SECTION 3

RESULTS AND DISCUSSIONS

3.1 Copper

3.1.1 Sequential reverse loading response

The stress-strain characteristics of OFHC copper specimens of 1.1 mm nominal gage length under sequential reverse twisting at the strain rate of about 1100 s^{-1} are presented in Figs. 15(a), (b) and (c) for the cyclic strain amplitude of about 0.46, 0.68 and 0.97, corresponding to clamp position I, II and III, respectively. Four loading sequences are shown in each of the three cases, causing a total cumulative strain of about 1.32, 1.75 and 3.7, respectively, after which the test was stopped although the specimen did not show any sign of failure or flow instability. The elapsed time between any two consecutive loadings did not exceed five minutes in all cases. Note that the curves resulting from reverse loadings (-) are plotted in the figures upward, instead of downward, for ease of comparison with the curves resulting from forward loadings (+). As discussed above, it is difficult with strain-hardening materials to achieve the same strain rate by using the same amount of stored torque in consecutive loadings. A decreasing strain rate is obtained instead, as observed in Figs. 15(a) and (b). A slight increase in the amount of stored torque, however, can help in keeping the strain rate constant, as seen in Fig. 15(c). The effects of this decrease in strain rate between consecutive loadings were judged to be of secondary importance and, therefore, neglected in the present analysis.

Close examination of the response reveals the following behavioral features:

- (a) The first loading is characterized by an elastic behavior of small slope and an undefined transition to plastic flow. Yield stress level was taken at the limit of proportionality, and is pointed at in the figures by a short horizontal arrow. Following this initial yield, plastic deformation takes place with considerable work hardening, as it is well known for annealed pure copper. This is described by an equation of the form:

$$\tau = K \gamma^n ; \quad \gamma > \gamma_y \quad (5)$$

where K and n are the strain-hardening coefficient and exponent, respectively, whose calculated values are shown in Table IV. Eq. (5) was assumed to be valid for large strains, and was consequently used to extrapolate the flow curve beyond the level reached upon first loading, as shown by dotted lines in Figs. 15(a), (b) and (c).

- (b) Sequential reverse loadings are characterized by initial elastic behavior with a slope considerably larger than that of first loading and unloading. The limit of proportionality is taken as the yield point, whose level is always found lower than the maximum stress level reached in the previous loading, indicative of the existence of a Bauschinger effect.
- (c) In Fig. 15(a), where the strain amplitude is the smallest, the flow curve upon sequential reverse loading starts by being higher than the level expected by extrapolation from continuous forward loading, but subsequently gets closer to this extrapolated level, and ultimately ends up below it in the fourth loading, indicative of continuous "softening" of the material with reverse loading. Moreover, the flow curve flattens out with increasing sequential loading, probably reaching saturation at a later stage. This same trend is also seen to occur, but more rapidly, in the case of the larger strain amplitude of Fig. 15(b), whereas "softening" starts from the first reverse loading in the case of the largest strain amplitude of Fig. 15(c). In all three cases, it also appears that, irrespective of the previous loading history, the flow curve in sequential reverse loading assumes a lower level than that of continuous forward loading starting from a total cumulative strain of about 0.95.

The stress-strain characteristics of OFHC copper specimens of 3.0 mm nominal gage length under sequential reverse twisting at the strain rate of about 550 s^{-1} are presented in Figs. 16(a), (b) and (c) for the cyclic strain amplitude of 0.23, 0.33 and 0.46, corresponding to clamp position I, II and III, respectively. Exactly the same characteristics and behavioral features are exhibited here, as those discussed above pertaining to the higher strain rate of 1100 s^{-1} . In the present case, however, the flow curve in sequential reverse loading assumes a lower level than that of continuous forward loading starting from a total cumulative strain of about 0.60.

At the quasi-static strain rate of about 0.001 s^{-1} , the stress-strain characteristics of OFHC upon forward and reverse twisting for the prestrain of 0.43, 0.76 and 1.1 are presented in Figs. 17(a), (b) and (c) respectively. Similar characteristics are exhibited with respect to forward loading. Upon reverse loading at the smallest prestrain, the flow curve also assumes a higher level than that of the continuous forward loading obtained by extrapolation, but the difference is not large. For larger values of prestraining, the reverse flow curve is characterized after the transition to plastic flow by an almost constant stress level plateau, which lasts for longer reverse deformations, the larger the forward prestrain. This plateau is then followed by strain hardening, but the flow curve level remains lower than that of continuous forward loading.

At all strain rates, therefore, sequential reverse loading causes the flow curve to flatten out and to ultimately reach saturation. This can be attributed, as suggested by Armstrong et al/12/ who exposed annealed 1100 aluminum specimens to slow multiaxial straining, to the large accumulated plastic strain and to an enhancement of 'softening' or "recovery" processes.

3.1.2 Analysis of behavior in terms of B.E. parameters

Some of the features discussed above may now be described quantitatively, as shown in Fig. 18 defining different parameters which may be used for that purpose. $\Delta\tau = \tau_o - \tau_y$ is the amount of strain hardening during prestraining. τ_{yr} is the reverse yield stress, and $\tau_B = \tau_o - |\tau_{yr}|$ is the decrease of yield stress, commonly denoted as "Bauschinger stress". In the present analysis, the magnitude of the Bauschinger effect is expressed by two indicators: τ_B and $\tau_B/\Delta\tau$, the latter parameter being more important from the viewpoint of microscopic aspects of the phenomenon/13/. On this basis, Table V lists various quantities as calculated from the first reversal in Figs. 15, 16 and 17.

The reverse yield stress, τ_{yr} , and the Bauschinger stress, τ_B , are both plotted versus the prestrain γ_o , for various strain rates, in Fig. 19. By definition, τ_{yr} should equal τ_y and take the values 40, 25 and 20 MPa for the three strain rates 1100, 550 and 0.001 s^{-1} , respectively, at $\gamma_o = \gamma_y \sim 0$, while $\tau_B (= \tau_o - \tau_{yr})$ should always vanish at $\gamma_o \sim 0$; such trends are exhibited to some extent if the shown curves are extrapolated, as shown by the dashed lines, to zero prestrain. As can be seen from Fig. 19, for a given γ , increasing γ_o

results in an increase in τ_{yr} and in τ_B . On the other hand, at any given γ_0 , increasing γ increases τ_{yr} and τ_B .

Figure 20 shows the effect of prestrain and strain rate on the second Bauschinger effect indicator $\tau_B/\Delta\tau$. This ratio increases with increasing prestrain, and decreases with increasing the impact strain rate. The present results are obtained at large values of prestrain, in contrast to those available in the literature for copper which are at much lower prestrains /12/; moreover, the definition used for the yield stress in materials like copper seems to affect the trend of behavior. On the other hand, comparing the present results with those obtained previously for an aluminum alloy /9/ does not indicate any close correspondence, although the two materials have an FCC crystallographic structure. This essentially indicates the effect of other structural parameters, particularly the stacking-fault energy (SFE), on the behavior of metals, as discussed by previous investigators /12,13,14/; aluminum being known to have high SFE, whereas copper is known to have a low SFE.

The effect of sequential reversal of loading is also examined by calculating the Bauschinger effect parameters corresponding to the fourth loading, and contrasting them with those presented and studied above for the second loading. All relevant quantities are listed in Table VI, as calculated from the data shown in Figs. 15 and 16. The reverse yield stress is plotted versus the cumulative strain γ_c , for the two impact strain rates, in Fig. 21. Shown in solid lines are the values calculated for the second loading, while in dashed lines are the values corresponding to the fourth loading. For each strain rate, values of τ_{yr} seem to fall on the same continuous curve which tends to a steady-state or saturation value with increasing cumulative shear strain; this saturation value, is higher the higher the strain rate, and is also expected to be a function of the value of the cyclic strain amplitude. Such trend falls within the general observations associated with fatigue and multidirectional testing of metals /12,15-17/ at low strain rates.

Also in Fig. 21, the variation of the Bauschinger stress at the three strain rates with cumulative strain, γ_c , is shown in solid lines for the second loading, and in dashed lines for the fourth loading. It should be noted here that, in both cases, $\tau_B = \tau_0 - \tau_{yr}$ where τ_0 is the maximum stress level reached on the immediate previous loading. With both τ_0 and τ_{yr} tending to almost steady

state values at large cumulative strains, the same trend is also approximately observed for τ_B . Similar observations are also made from Fig. 22 for the variation of the B.E. indicator, $\tau_B/\Delta\tau$, with γ_c , where $\Delta\tau = \tau_o - \tau_y$.

3.2 Mild Steel

3.2.1 Sequential reverse loading response

The stress-strain characteristics of mild steel specimens of 1.1 mm nominal gage length under sequential reverse twisting at the strain rate of about 760 s^{-1} are presented in Figs. 23(a), (b) and (c) for the cyclic amplitude of about 0.262, 0.46 and 0.65, corresponding to clamp position I, II and III, respectively. Four loading sequences are shown in each case, except in the case of cyclic strain amplitude of 0.262 shown in Fig. 23(a) where the test was ended only after two loadings due to the fracture of the specimen flange-to-input bar epoxy joint. Total cumulative strains of about 1.7 and 2.1 were achieved in the last two cases, respectively, and caused the specimen to fracture. The elapsed time between any two consecutive loadings, like with copper, did not exceed five minutes in all cases. Note that here also, the curves resulting from reverse loadings (-) are plotted in the figures upward, instead of downward, for ease of comparison with the curves resulting from forward loadings (+). Because strain hardening is quite small in mild steel in comparison to copper, the strain rate can be seen to vary very little upon sequential loading.

Close examination of the response reveals the following behavioral features:

- (a) The first loading is characterized by an elastic behavior of a large slope as expected. Yield stress was taken at the limit of proportionality, and is pointed at in the figures by a short horizontal arrow. Following yielding, plastic deformation takes place and work hardening quickly assumes its steady-state value, which is quite smaller than for copper. A power law can also be used to describe plastic flow in mild steel. Corresponding calculated values of K and n in Eq. (5) are listed in Table VII. This equation was assumed to be valid for large strains, and was used to extrapolate the flow curve beyond the level reached upon first loading, as shown by dotted lines in Figs. 23(a), (b) and (c).

- (b) Sequential reverse loadings are characterized by initial elastic behavior with a slope almost similar to that in first loading and unloading. The limit of proportionality, also pointed at with a short arrow, was taken as the yield point.
- (c) Plastic flow following reverse yielding proceeds always at a level below that expected by extrapolation from continuous forward loading. This level gets lower and lower with subsequent reverse loading, indicative of continuous softening of the material. Also, the flow curve flattens out with increasing sequential loading, most probably reaching saturation had the specimen not fractured.

The stress-strain characteristics of mild steel specimens of 3.0 mm nominal gage length under sequential reverse twisting at the strain rate of 350 s^{-1} are presented in Figs. 24(a), (b) and (c) for the cyclic strain amplitude of 0.15, 0.25 and 0.312, corresponding to clamp position I, II and III, respectively. Exactly the same characteristics are exhibited here, as those discussed above pertaining to the higher strain rate.

At the quasi-static strain rate of about 0.001 s^{-1} , the stress-strain characteristics upon forward and reverse twisting for the prestrains of 0.135 and 0.26 are presented in Figs. 25(a) and (b), respectively. Similar features as those discussed above for the impact strain rates are also exhibited in the present case.

At all strain rates, therefore, sequential reverse loading causes the flow curve to continuously deviate from the unidirectional continuous flow curve, and to flatten out progressively reaching saturation.

3.2.2 Analysis of behavior in terms of B.E. parameters

Table VIII lists various quantities describing the Bauschinger effect phenomenon, as calculated from the first reversal in Figs. 23, 24 and 25. The reverse yield stress and the Bauschinger stress are both plotted versus prestrain for the three strain rates in Fig. 26. Both quantities increase with increasing strain rate, at any given prestrain. Thus, the loss of strength is greater, the higher the strain rate. This is also greater the larger the prestrain. The same trends are also substantiated in the plots of Fig. 27 showing the variation of the second B.E. parameter $\tau_B/\Delta\tau$ with prestrain.

To contrast these results with those corresponding to the fourth sequential loading, all relevant quantities were calculated for both cases from Figs. 23 and 24 and listed in Table IX. τ_{yr} and τ_B are plotted in Fig. 28, while $\tau_B/\Delta\tau$ is plotted in Fig. 29, versus cumulative shear strain, for the two impact strain rates, as solid lines for the second loading and as dashed lines for the fourth loading. A steady-state or saturation value seems to exist for τ_{yr} , of a level being higher for the larger strain rate. This is also dependent on the value of the cyclic strain amplitude but to a lesser extent than with copper due to the difference in SFE and consequently in the recovery processes involved, as has been suggested in the literature by comparing the behavior of copper and iron under fatigue testing at low strain rates /12/. τ_B and $\tau_B/\Delta\tau$, used in the present context as Bauschinger effect indicators, exhibit a similar trend of behavior as function of cumulative strain. Both increase with increasing sequential loading, but seem to stabilize at large values of strain. Comparing also the behavior exhibited in Fig. 29 with that for copper in Fig. 22, it is clear from the shown values of $\tau_B/\Delta\tau$ at a given γ_c and the lowest impact strain rate that the Bauschinger effect phenomenon is more appreciable in mild steel than in copper.

From the present results of both copper and mild steel, as well as from those previously reported for aluminum /9/, it is possible to conclude that sequential reverse loading at large plastic strains progressively weakens the material, more seriously so at impact strain rates than at the quasi-static ones. These results should be accounted for in the design of structural engineering components, as well as in the planning of metal forming operations.

3.3 Application of Classical Anisotropic Hardening Theories to Results

It is clear from the results presented above that the flow stress of copper and mild steel at quasi-static and at impact rates of straining is direction dependent. This fact has been known for long for many materials subjected to a non-proportionate loading path, at low strain rates. Various theories have been proposed to account for this deformational anisotropy. Those used in the present comparison are listed and discussed briefly in the following. Bauschinger effect in shear is also defined as predicted in each case for later comparison with the present experimental results. Further details of derivations can be found elsewhere /18,19/.

3.3.1 Prager's kinematic hardening rule /20/

Here, linear work hardening is assumed with the initial yield surface translating rigidly in the direction of the exterior normal at the stress point. This predicts that the difference between τ_o and τ_{yr} which defines the elastic range, upon unloading and reverse loading from τ_o , is a constant $2 \tau_y$, cf. Fig. 9.

3.3.2 Ziegler's rule /21/

The proposal here is that the initial yield surface translates rigidly in the direction of the vector connecting its centre to the stress point on it. This, together with the linear work hardening law, predict an identical Bauschinger effect in torsion as in Prager's rule.

3.3.3 Baltov and Sawczuk /22/

These authors used the kinematic hardening rule to develop a hardening model which allows an initial von Mises yield surface to translate, expand and rotate in stress space. A hardening constant H indicates whether the surface expands ($H < 0$) or contracts ($H > 0$). With linear work-hardening, and proper boundary conditions, the Bauschinger effect in torsion associated with this rule is given by

$$\frac{\tau_{yr}}{\tau_y} = \frac{\tau_o}{\tau_y} \left[\frac{\sqrt{\left(\frac{\tau_o}{\tau_y} - 1\right)^2 + H \left(\frac{\tau_o}{\tau_y} - 1\right)^4} - 1}{\sqrt{\left(\frac{\tau_o}{\tau_y} - 1\right)^2 + H \left(\frac{\tau_o}{\tau_y} - 1\right)^4} + 1} \right]. \quad (6)$$

When $H = 0$, Eq. (6) reduces to kinematic hardening.

3.3.4 Edelman and Drucker /23/

Here, an anisotropic yield function is developed which is based upon the interaction of prestrain and yield stress components. The associated Bauschinger effect is given by

$$\tau_{yr} = -(\tau_o - m \gamma_o^P), \quad (7)$$

where m is an empirical constant describing the translation of the initial yield locus, and γ_o^P is the plastic prestrain.

3.3.5 Comparison with experimental results

Although the present data are collected mostly at high strains and strain rates, which are not been accounted for in the classical plasticity theories where deformations are assumed to be small, slow and isothermal, it seems worthwhile to make the comparison and to appreciate the deviations, if any. Consequently, the values of τ_{yr} and τ_o have been normalized with respect to τ_y and listed together with previous data in Tables V and VIII for copper and mild steel, respectively.

Values of τ_{yr}/τ_y are plotted versus τ_o/τ_y in Fig. 30 for the present data on copper and mild steel, and also for the previously reported data on aluminum /9/. Various lines are shown in this figure. One of these lines corresponds to isotropic hardening, for which $\tau_{yr}/\tau_y = -\tau_o/\tau_y$; this is of course unrealistic with the data points. Another line has the equation: $\tau_{yr}/\tau_y = (\tau_o/\tau_y) - 2$, which represents Prager's and Ziegler's kinematic hardening rule; as discussed above, this is also represented by Eq. (6) with $H = 0$. Kinematic hardening is seen to be an improvement, but underestimates the magnitude of the Bauschinger effect. Eq. (6) representing Baltov and Sawczuk's rule is plotted also in Fig. 30 for different values of the hardening constant H . Some further improvement seems to be introduced in the predictions of the relation between τ_{yr}/τ_y and τ_o/τ_y , but still no complete agreement seems to exist, as expected, particularly for copper whose work hardening characteristic is well rounded and cannot be expressed by a linear law. Reasonable agreement is noticed with aluminum for a value of $H \sim 10 - 100$. Interestingly enough, this material was found to be almost insensitive to strain rate and to have an approximately linear strain hardening /9/. On the other hand, the trend of the agreement between data points and theory seems to indicate that the values of H corresponding to the three materials are positive, which qualitatively indicate the Bauschinger effect corresponds to a contraction and a translation of the initial yield locus. Similar overall conclusions have been also reported recently for quasi-static data on a mild steel and two aluminum alloys /24/.

Equation (7) can be rewritten in normalized form as

$$\frac{m}{\tau_y} = \frac{\tau_{yr} + \tau_o}{\tau_y} \cdot \frac{1}{\gamma_o^p} \quad (8)$$

Checking the validity of the Bauschinger constant m in the theory of Edelman and Drucker can be done by calculating m/τ_y from the data listed in Tables V

and VIII for copper and mild steel, and from previous data on aluminum /9/, and plotting m/τ_y versus γ_o^P . This is shown for the data collected at various strain rates for the three materials in Fig. 31. For all three materials and all rates, it is clear that a large variation exists in m/τ_y , indicating that Bauschinger effect cannot be controlled by a single constant m as in Edelman and Drucker's theory. Other parameters and functions may be used as implied by the modifications introduced by Yoshimura /25/, Williams and Svensson /26/ as well as others, but these are not discussed further in this report. The main conclusion is that theories of work hardening based on classical plasticity concepts are not capable of describing faithfully the reverse loading characteristics exhibited by metallic materials, particularly when rate effects are also predominant.

3.4 Identification from the Literature of Constitutive Equations Suitable for Modeling Bauschinger Effect in Metals

As illustrated from the experimental results, the mechanical response of aluminum, copper and mild steel under the present testing conditions of sequential reverse twisting at large strains and quasi-static as well as impact strain rates has been found to be generally strain-history dependent as well as sensitive to various degrees to strain rate. The evaluation of this response in the light of current constitutive equations for metals is not straightforward nor simple, as will be soon appreciated.

Presently available constitutive models for predicting inelastic behavior in metals are quite diverse but it seems possible to place them into a common framework. Accordingly /26/, these theories can be grouped into one of three general categories, namely:

- (a) Extensions of classical rate-independent plasticity theories which are based on the concept of a yield function. These can be divided into: (i) the uncoupled theories in which the inelastic deformation is assumed to be decomposable into rate-dependent creep and rate-independent plasticity components /27-29/, and (ii) the unified theories, wherein all inelastic deformation is embodied in a single term /30-33/.
- (b) Non-linear viscoelasticity theories which are usually based on macrophenomenological thermodynamics or resulting mechanical analogs /34-38/.

(c) Microphenomenological theories which find their origin in microphysics /39-46/.

Of all these theories, those falling in the last category have been found more feasible since, in the most part, they are fundamentally based in the micromechanisms causing inelastic deformation, such as dislocation glide and climb, dislocation pileups, cross slip, grain-boundary sliding, diffusion, etc. Consequently, many of these theories were subjected recently to considerable study, and evaluation by comparing their theoretical predictions with the actual experimental response for simple as well as complex input histories. Some of these recent comparative investigations are those of Walker /47/ (Walker /38/, Krieg et al /41/, Miller /44/), Cernocky /48/ (Bodner and Partom /42/, Cernocky and Krempl /37/, Lin and Wu /35) and /49/ (Bodner et al /42,43/, Cernocky and Krempl /37/, Cernocky /48/), Beek, Allen and Milly /50/ (Allen and Haisler /28/, Valanis /34/, Cernocky and Krempl /37/), Walker /38/, Hart /40/, Krieg et al /41/, Bodner et al /42,43/, Miller /44, Robinson /45/ and Cescotto and Leckie /46/), and Eftis and Jones /19/ (most of the theories in /26/-/46/). Criteria used for evaluating each theory include. (a) the facility of its calibration, i.e. determination of material constants from experimental data; (b) its predictive capabilities of: monotonic, cyclic hysteresis, creep, stress relaxation and multiaxial responses; (c) its sensitivity to numerical integration; and (d) the sensitivity of the response to small changes in material constants.

The conclusions of the comparative study of various constitutive theories made by Beek, Allen and Milly /50/ are particularly interesting. These are given in Tables X, XI and XII taken from their report. The uniaxial formulation of each model is listed in Table X, using a common notation. Beek et al /50/ showed that, within a thermodynamic framework, all models are consistent with the internal state variable formulation. Thus, any model can be written in the following uniaxial form:

$$\sigma = E (\epsilon - \alpha_1 - \epsilon^T) \quad (9)$$

where σ , E , ϵ , α_1 and ϵ^T are the stress, Young's modulus, strain, inelastic strain (considered as an internal state variable) and thermal strain, respectively. In each theory, a growth law for the internal state variable α_1 is further postulated, and α_1 is obtained by time integration. Thus:

$$\dot{\alpha}_1 = \frac{d\alpha_1}{dt} = \dot{\alpha}_1 (\epsilon, T, \alpha_2, \alpha_3, \dots, \alpha_m) \quad (10)$$

and

$$\alpha_1 = \int_{-\infty}^t \dot{\alpha}_1 (t') dt', \quad (11)$$

where t is the time, T : the temperature, α_2 : the back stress which is related to dislocation arrangement and thus produces kinematic hardening and Bauschinger effect, and α_3 : the drag stress which represents the dislocation density and produces isotropic hardening.

Differences between various models are due to the number of internal state variables and their growth laws. Also, the experimental data needed for characterization vary greatly between models. From the assessment made by Beek et al /50/, the model of Cernocky and Krempl /37/ seems to be complex enough to model viscoplastic behavior in metals, for low temperature and monotonic load conditions. The theory proposed by Bodner et al /42,43/ seems to be extremely useful, simple to construct and to give good results for high strain rate applications as verified recently by Bodner and coworkers. This theory has also been applied recently by the present author with satisfactory results on quasi-static to dynamic strain-rate change in tension on AISI 316 stainless steel at ambient temperature /51/. On the other hand, Stouffer and Bodner /52/ and more recently Bodner /53/ attempted to introduce anisotropic hardening into the original formulation of the theory. Experimental verifications of these modifications have not been reported yet in the literature.

Based on the previous review and discussions, it may be concluded that possible models to recommend for fitting the present experimental results would be those of Cernocky and Krempl, and Bodner and associates. Neither of the two should be expected to give complete satisfactory results, however, mainly because of the large plastic strains achieved in the present tests, and accompanying non-linearities which would require a rigorous theoretical approach.

SECTION 4

CONCLUSIONS

A major part of this work was to establish new data bases for OFHC copper and plain carbon steel, related to their strain-history dependence, particularly in terms of the hysteresis loop upon load reversals and the associated Bauschinger effect, at quasi-static as well as impact strain rates. Such information should be accounted for and used to remedy the present practice in which many fabricated components used in mechanical, civil or aeronautical applications, experience loads during their service life which pay no heed to previous deformation history.

The phenomenological behavior of the two materials was obtained through a series of sequential reverse torsional shear tests at impact strain rates using a modified split Hopkinson bar and a quasi-static strain rate using a slow rotational drive unit. The observed response was next evaluated in terms of various Bauschinger effect parameters, and also in the light of predictions from classical plasticity theories as first and crude approximation. Finally, the excellent reviews available in the literature on modern constitutive equations recently proposed for metals were examined and those most probably suited to model the present results were identified.

The main results of the present investigation are hereafter emphasized again as main conclusions:

- (a) Cyclic loading of materials at intermediate or large constant strain amplitudes and at impact strain rates can be achieved with the minimum amount of difficulty in torsional shear using a properly-modified classical stored-torque split Hopkinson bar apparatus. The value of the strain amplitude can be controlled by the position of the friction clamp along the system. The strain rate achieved, and hence also the strain, is essentially controlled by the amount of stored torque and also the specimen gage length.
- (b) On ductile materials like aluminum and copper, sequential reverse impact torsion can be continued for a large number of cycles until instabilities limit further deformation. With materials of limited ductility, like steel, this ends in fracture after a few cycles.

- (c) Of the three materials tested, the aluminum alloy has the least strain-rate sensitivity, under monotonic loading, whereas mild steel is the most sensitive. This is in line with our current knowledge of the strain-rate sensitivity of metals.
- (d) The stress-strain behavior of all three materials is affected by strain history. The effect is more appreciable, however, for highly strain-rate sensitive materials.
- (e) For copper, irrespective of previous loading history, the flow curve in sequential reverse loading assumes a lower level than that of continuous forward loading starting from a total cumulative strain of 0.95. In mild steel, however, plastic flow following reverse yielding proceeds always at a level below that expected from continuous forward loading. For both materials, the flow curve flattens out with increasing sequential loading, ultimately reaching saturation.
- (f) Reverse loading characteristics, particularly the Bauschinger phenomenon, can be described at all strain rates by means of quantitative parameters, such as τ_{yr} , τ_B and $\tau_B/\Delta\tau$. In general, values of each parameter vary with strain rate. Consequently, it is inaccurate to describe the reverse loading behavior of strain-rate sensitive metallic materials by using data collected at the quasi-static strain rate, as it is often followed in the analysis of structural engineering problems. Instead, it will be much more accurate and economical to use values of the yield stress ratio, $YSR = \tau_{yr}/\tau_o$ which, for a given prestrain, do not vary much with strain rate (cf. Tables V and VIII).
- (g) Comparing the present experimental results with predictions of the classical anisotropic hardening theories indicate that reasonable agreement does not seem to exist when comparison is made with various modified versions of the original Prager's kinematic hardening rule. This is not unexpected, given the fact that the present data were collected at fairly large strains, high strain rates and generally non-isothermal conditions.
- (h) Reviewing the literature on advanced constitutive models recently proposed for metals, and examined in more details by other investigators, it appears that the theories of Bodner and associates and of Cernocky and Krempl offer the greatest promises for fitting the present experimental data. However, because of the finite strains involved in the present data, such statement

should be checked by actual comparisons in order to provide directions for more rigorous theoretical treatments, if needed. This should be a worthy research area to explore in future studies in dynamic plasticity.

SECTION 5

REFERENCES

- 1- Duffy, J., "The J.D. Campbell Memorial Lecture: Testing Techniques and Materials Behavior at High Rates of Strain", in J. Harding (Ed.) Mechanical Properties of Materials at High Rates of Strain, 1-15, Conference Series NO. 47, The Institute of Physics, London (1979).
- 2- Duffy, J., "The Dynamic Plastic Deformation of Metals: A Review", Technical Report AFWAL-TR-82-4024, Materials Laboratory, Air Force Wright Aeronautical Laboratories, Wright-Patterson Air Force Base, Ohio, U.S.A. (1982).
- 3- Nicholas, T., "Material Behavior at High Strain Rates", in Impact Dynamics, J.A. Zukas, T. Nicholas, H.F. Swift, L.B. Greszczuk and D.R. Curran, Chapter 8, 277-232, John Wiley & Sons (1982).
- 4- Campbell, J.D., "A Double-Pulse Torsional Hopkins on Bar Technique for Investigating Strain-Rate Effects", Technical Report AFML-TR-72-207, Air Force Materials Laboratory, Wright-Patterson Air Force Base, Ohio, U.S.A. (1972).
- 5- Percy, J.H., "New Techniques for Testing Materials at High Strain Rates", in Stress and Strain in Engineering, 219-223, National Conference Publication No. 73/5, Institution of Engineers, Australia (1973).
- 6- Tanaka, K. and Nojima, T., "Strain Rate Effect on the Strength of Aluminum", in S. Taira and M. Kunugi (Eds.) Mechanical Behaviour of Materials, Vol. 1, 176-183, Soc. Mat. Sci., Japan (1971).
- 7- Duffy, J., Campbell, J.D. and Hawley, R.H., "On the Use of a Torsional Split Hopkinson Bar to Study Rate Effects in 1100-O Aluminum", J. Appl. Mech., 38, 83-91 (1971).
- 8- Eleiche, A.M. and El-Kady, M.M., "A Modified Split Hopkinson Bar for the Cyclic Loading of Materials at Dynamic Strain Rates", in R. Wagoner (Ed.) Novel Techniques in Metal Deformation Testing, 323-340, A.I.M.E., Warren, Ohio (1983).
- 9- Eleiche, A.M. and Megahed, M.M., "Inelastic Deformation of Metals and Structures Under Dynamic and Quasi-Static Cyclic Loading", Annual Technical Report to ERO, Contract Number DAJA37-81-C-0236, May 1982.
- 10- Lindholm, U.S., "Some Experiments with the Split Hopkinson Bar", J. Mech. Phys. Solids, 12, 317-335 (1964).
- 11- El-Kady, M.M.M., A Torsional Split Hopkinson Bar Apparatus Adapted for Cyclic Loading at Impact Strain Rates, M.Sc. Thesis, Dept. of Mechanical Design and Production, Faculty of Engineering, Cairo University, Egypt, June 1982.
- 12- Armstrong, P.E., Hockett, J.E. and Sherby, O.D., "Large Strain Multi-directional Deformation of 1100 Aluminum at 300 K", J. Mech. Phys. Solids, 30, 37-58 (1982).
- 13- Gokyu, I. and Kishi, T., "On the Bauschinger Effect of Polycrystals", Proc. 13th Japan Congress on Materials Research, 125-128 (1970).

- 14- Abel, A. and Muir, H., "The Bauschinger Effect and Stacking Fault Energy", Phil. Mag., 27, 585-594 (1973).
- 15- Coffin, L.F., Jr., and Tavernelli, J.F., "The Cycling Straining and Fatigue of Metals", Trans. AIME, 215, 794 (1959).
- 16- Pratt, J.E., "Dislocation Substructure in Strain - Cycled Copper", Journal of Materials, 1, 77-88 (1966).
- 17- Thomsen, E.G., "Stress-Strain Properties of Tough-Pitch Copper after Multi-Pass Drawing and Extruding", J. Eng. Mats & Tech., Trans. ASME, 105, 178-181 (1983).
- 18- Martin, J.B., Plasticity: Fundamentals and General Results, MIT Press, U.S.A. (1975).
- 19- Eftis, J. and Jones, D.L., "Evaluation and Development of Constitutive Relations for Inelastic Behavior," Final Technical Report, GWU/CME/TR-83/1, Air Force Office of Scientific Research, Washington, D.C., U.S.A. (1983).
- 20- Prager, W., "A New Method of Analysing Stress and Strains in Work-Hardening Plastic Solids", J. Appl. Mech., 23, 493-496 (1956).
- 21- Ziegler, H., "A Modification of Prager's Hardening Rule", Quart. Appl. Math., 17, 55-65 (1959).
- 22- Baltov, A. and Sawczuk, A., "A Rule of Anisotropic Hardening", Acta Mechanica, 1, 81-92 (1965).
- 23- Edelman, F. and Drucker, D.C., "Some Extensions to Elementary Plasticity Theory", J. Franklin Inst., 251, 581-605 (1951).
- 24- Rees, D.W.A., "Anisotropic Hardening Theory and the Bauschinger Effect", Journal of Strain Analysis, 16, 85-95 (1981).
- 25- Yoshimura, Y., "Hypothetical Theory of Anisotropy and the Bauschinger Effect Due to a Plastic Strain History", Aeron. Res. Inst. Tokyo Univ., 349, 224-246 (1959).
- 26- Allen, D.H., "A Thermodynamic Framework for Comparison of Current Thermo-viscoplastic Constitutive Models for Metals at Elevated Temperatures", Proc. Int. Conf. Constitutive Laws for Engineering Materials, University of Arizona, Tucson, Arizona, 61-69 (1983).
- 27- Yamada, Y. and Sakurai, T., "Basic Formulation and a Computer Program for Large Deformation Analysis", Pressure Vessel Tech. Trans. ASME, 341-352 (1977).
- 28- Allen, D.H. and Haisler, W.E., "A Theory for Analysis of Thermoplastic Materials", Computers & Structures, 13, 129-135 (1981).
- 29- Allen, D.H., "Computational Aspects of the Nonisothermal Classical Plasticity", Computers and Structures, 15, 589-599 (1982).
- 30- Perzyna, P., "Fundamentals Problems in Viscoplasticity", Adv. Appl. Mech., 9, 243-377 (1966).
- 31- Zienkiewicz, O.C. and Courmeau, I.C., "Viscoplasticity-Plasticity and Creep in Elastic Solids - A Unified Numerical Approach", Int. J. Num. Meth. Engng., 8, 821-845 (1974).

- 32- Chaboche, J.L., "Viscoplastic Constitutive Equations for the Description of Cyclic and Anisotropic Behavior of Metals", Bulletin de l'Academie Polonaise des Sciences, Série des Sciences Techniques, Vol. XXV, 33 (1977).
- 33- Lee, D. and Zaverl, F., Jr., "A Generalized Strain Rate Dependent Constitutive Equation for Anisotropic Metals", Acta Met., 26, 1771-1780 (1978).
- 34- Valanis, K.C., "A Theory of Viscoplasticity Without a Yield Surface", Arch. Mech., 23, 517-551 (1971).
- 35- Lin, H.C. and Yu, H.C., "Strain-Rate Effect in the Endochronic Theory of Viscoplasticity", J. Appl. Mech., 43, 92-96 (1976).
- 36- Laflen, J.H. and Stouffer, D.C., "An Analysis of High Temperature Metal Creep", J. Eng. Mat. & Tech. 100, 363-380 (1978).
- 37- Cernocky, E.P. and Krempl, E., "A Theory of Viscoplasticity Based on Infinitesimal Total Strain", Acta Mech. 36, 263-289 (1980).
- 38- Walker, K.P., "Representation of Hastelloy-X Behavior at Elevated Temperature with a Functional Theory of Viscoplasticity", Presented at ASME Pressure Vessels Conference, San Francisco (1980).
- 39- Kocks, U.F. "Laws for Work Hardening and Low-Temperature Creep", J. Eng. Mat. & Tech., 98, 76-85 (1976).
- 40- Hart, E.W., "Constitutive Relations for the Non-Elastic Deformation of Metals", J. Eng. Mat. & Tech., 98, 193-202 (1976).
- 41- Krieg, R.D., Swearingen, J.D. and Rohde, R.W., "A Physically-Based Internal Variable Model for Rate-Dependent Plasticity", Proc. ASME/CSME PVP Conf., 15-27 (1978).
- 42- Bodner, S.R. and Partom, Y., "Constitutive Equations for Elastic-Viscoplastic Strain-Hardening Materials", J. Appl. Mech. 42, 385-389 (1975).
- 43- Bodner, S.R., Partom, I. and Partom, Y., "Uniaxial Cyclic Loading of Elastic-Viscoplastic Materials," J. Appl. Mech. 46, 85-810 (1979).
- 44- Miller, A.K., "An Inelastic Constitutive Model for Monotonic, Cyclic and Creep Deformation", J. Eng. Mat. & Tech., 98, 97-112 (1976).
- 45- Robinson, D.N., "A Unified Constitutive Relationship for the Time-Dependent Behavior of Fast-Breeder Alloys", Proc. Symp. Nonlinear Constitutive Relations for High Temperature Applications, Univ. of Akron, May 1982.
- 46- Cescotto, S. and Leckie, F., "Determination of Unified Constitutive Equations for Metals at High Temperature", Proc. Int. Conf. Constitutive Laws for Engineering Materials, University of Arizona, Tucson, Arizona, 105-111 (1983).
- 47- Walker, K.P. "Research and Development Program for Nonlinear Structural Modeling with Advanced Time-Temperature Dependent Constitutive Relationships", NASA CR-165533 (1981).
- 48- Cernocky, E.P. "An Examination of Four Viscoplastic Constitutive Theories in Uniaxial Monotonic Loading", Int. J. Solids Structures, 11, 989-1005 (1982).

- 49- Cernocky, E.P., "Comparison of the Unloading and Reversed Loading Behavior of Three Viscoplastic Constitutive Theories", Int. J. Non-Linear Mechanics, 17, 255-266 (1982).
- 50- Beek, J.M., Allen, D.H. and Milly, T.M., "A Qualitative Comparison of Current Models for Nonlinear Rate-Dependent Material Behavior of Crystalline Solids", MM4 246 T-83-14, Mechanics and Materials Center, Texas A&M University, College Station, Texas, November 1983.
- 51- Eleiche, A.M., Albertini, C. and Montagnani, M., "The Influence of Strain-Rate History on the Ambient Tensile Strength of AISI 316 Stainless Steel", in High Energy Rate Fabrication - 1984, ed. by I. Berman and J.W. Shroeder, 213-219, ASME (1984).
- 52- Stouffer, D.C. and Bodner, S.R., "A Constitutive Model for the Deformation Induced Anisotropic Plastic Flow of Metals", Int. J. Engng. Sci., 17, 757-764 (1979).
- 53- Bodner, S.R. "Evolution Equations for Anisotropic Hardening and Damage of Elastic-Viscoplastic Materials", Proc. Conf. on Plasticity Today, Udine, Italy, 1983.

TABLE I - Composition of Materials Tested

(a) Copper (OFHC) wt%)

Copper : 99.97

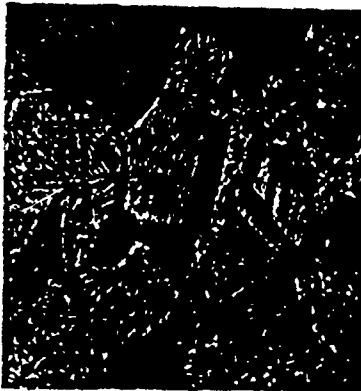
Fe : 0.03

Other elements : < 0.01

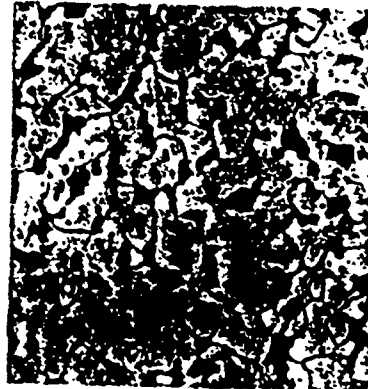
(b) Mild Steel

Typical composition as supplied (wt%)

C	Mn	S	P	Si	Ni	Cr
0.23	0.5	0.04	0.02	0.03	Not determined	



Copper



Steel

Typical microstructures before testing

TABLE II - List of Specimens Tested

Spec. No.	Nominal Dimensions (mm)			Actual Dimensions (mm)			Clamp Position	Useful Loading Time t_u (μs)	Average Expected Strain Rate $\dot{\gamma}$ (s^{-1})	Average Expected Strain† γ_o
	d_s	t_s	l_s	d_s	t_s	l_s				
C1	18.5	0.5	3	(a) OFHC Copper			I	530	530	0.23
C2	18.5	0.5	1.1	18.55	0.54	2.98	I	530	1100	0.46
C3	18.5	0.5	3	18.51	0.5	1.1	II	770	530	0.33
C4	18.5	0.5	1.1	18.49	0.48	3	II	770	1100	0.68
C5	18.5	0.5	3	18.51	0.5	1.1	III	1100	530	0.46
C6	18.5	0.5	1.1	18.49	0.48	2.98	III	1100	1100	0.97
S1	18.26	0.26	3	(b) Mild Steel			I	530	350	0.15
S2	18.26	0.26	1.1	18.27	0.26	2.96	I	530	760	0.32
S3	18.26	0.26	3	18.24	0.23	1.21	II	770	350	0.22
S4	18.3	0.3	1.1	18.27	0.26	2.95	II	770	760	0.46
S5	18.26	0.26	3	18.30	0.29	1.1	III	1100	350	0.31
S6	18.3	0.3	1.1	18.27	0.26	2.96	III	1100	760	0.67

† Calculated from t_u and $\dot{\gamma}$

N.B. Nominal inner diameter, d_i , is 18 mm; Actual inner diameter is 18.01 mm

TABLE III - Oscilloscope Records Calibration Values

<u>Record</u>	<u>Vertical Scales</u> (Nm/div)			
	<u>Copper</u> (Fig. 13)		<u>Steel</u> (Fig. 14)	
	Upper	Lower	Upper	Lower
A1 to A4	45	9	52	24
B1 to B4	46	18	46	21
C1 to C4	55	12	45	19
D1 to D4	45	18	55	27
E1 to E4	45	18	51.3	27
F1 to F4	55	26	45	18

NB. Horizontal sweep in all records is 200 μ s/div.

TABLE IV - Calculated values of K and n in the equation $\tau = K \dot{\gamma}^n$ for copper

$\dot{\gamma}$ (s^{-1})	K (MPa)	n
10^{-3}	130	0.28
550	175	0.43
1100	175	0.38

TABLE VII - Calculated values of K and n in the equation $\tau = K \dot{\gamma}^n$ for steel

$\dot{\gamma}$ (s^{-1})	K (MPa)	n
10^{-3}	324	0.14
350	331	0.08
760	364	0.06

TABLE V - List of Some Parameters Representative of Bauschinger Effect and Hardening for Reverse Loading on Copper

$\dot{\gamma}$ (s^{-1})	τ_y (MPa)	γ_o	τ_o (MPa)	$\Delta\tau =$ $\tau_o - \tau_y$ (MPa)	τ_{yr} (MPa)	$\tau_o - \tau_{yr}$ (MPa)	$YSR =$ $\frac{\tau_{yr}}{\tau_o}$	$\frac{\tau_B}{\Delta\tau}$	$\frac{\tau_{yr}}{\tau_B}$	$\frac{\tau_o}{\tau_B}$	$\frac{\tau_{yr}}{\tau_y}$	$\frac{\tau_o}{\tau_y}$	Relevant Quantities taken from
1100	40	0.45	131.5	91.5	127	4.5	0.966	0.049	28.2	29.22	3.18	3.29	Fig. 15(a)
		0.60	145	105	130	15	0.897	0.143	8.7	9.67	3.25	3.63	Fig. 15(b)
		0.97	170	130	138	32	0.812	0.246	4.3	5.31	3.45	4.25	Fig. 15(c)
550	25	0.24	97.5	72.5	94	3.5	0.964	0.048	26.8	27.86	3.76	3.90	Fig. 16(a)
		0.322	109	84	97	12	0.890	0.143	8.1	9.08	3.88	4.36	Fig. 16(b)
		0.508	129	104	101	28	0.783	0.269	3.6	4.61	4.04	5.16	Fig. 16(c)
10^{-3}	20	0.43	106	86	90	16	0.85	0.186	5.6	6.62	4.5	5.3	Fig. 17(a)
		0.76	118	98	96	22	0.813	0.224	4.3	5.36	4.8	5.9	Fig. 17(b)
		1.1	136	114	110	26	0.809	0.228	4.2	5.23	5.5	6.8	Fig. 17(c)

TABLE VI - List of Some Parameters Representative of Bauschinger Effect and Hardening for Sequential Reverse Loading on Copper (for the 2nd and 4th loadings)

$\dot{\gamma}$ (s ⁻¹)	τ_y (MPa)	γ_o	τ_o^+ (MPa)	$\Delta\tau = \tau_o - \tau_y$ (MPa)	τ_{yr} (MPa)	$\tau_o - \tau_{yr}$ (MPa)	$YSR = \frac{\tau_{yr}}{\tau_o}$	$\frac{\tau_B}{\tau_o}$	$\frac{\tau_{yr}}{\tau_B}$	$\frac{\tau_o}{\tau_B}$	$\frac{\tau_{yr}}{\tau_y}$	$\frac{\tau_o}{\tau_y}$	Relevant Quantities taken from
1100	40	0.45	131.5	91.5	127	4.5	0.966	0.049	28.2	29.22	3.18	3.29	Fig. 15(a)
		1.01	170	130	138	32	0.812	0.246	4.3	5.31	3.45	4.25	
		0.60	145	105	130	15	0.897	0.143	8.7	9.67	3.25	3.63	Fig. 15(b)
		1.33	163	123	140	23	0.859	0.187	6.1	7.09	3.50	4.08	
550	25	0.97	170	130	138	32	0.812	0.246	4.3	5.31	3.45	4.25	Fig. 15(c)
		2.79	189	149	147	42	0.778	0.282	3.5	4.50	3.68	4.73	
		0.24	97.5	72.5	94	3.5	0.964	0.048	26.8	27.86	3.76	3.90	Fig. 16(a)
		0.525	139	114	103	36	0.741	0.316	2.9	3.86	4.12	5.56	
550	25	0.322	109	84	97	12	0.890	0.143	8.1	9.08	3.88	4.36	Fig. 16(b)
		0.71	142	117	108	34	0.761	0.291	3.2	4.18	4.32	5.68	
		0.508	129	104	101	28	0.783	0.269	3.6	4.61	4.04	5.16	Fig. 16(c)
		1.325	148	123	115	33	0.777	0.268	3.5	4.48	4.60	5.92	

+ Represents the maximum stress level reached on the immediate previous loading

TABLE VIII - List of Some Parameters Representative of Bauschinger Effect and Hardening for Reverse Loading on Steel

$\dot{\gamma}$ (s ⁻¹)	τ_y (MPa)	γ_o	τ_o (MPa)	$\Delta\tau = \tau_o - \tau_y$ (MPa)	τ_{yr} (MPa)	$\tau_B - \tau_{yr}$ (MPa)	$YSR = \frac{\tau_{yr}}{\tau_o}$	$\tau_B \frac{\tau_{yr}}{\Delta\tau}$	$\frac{\tau_{yr}}{\tau_B}$	$\frac{\tau_o}{\tau_B}$	$\frac{\tau_{yr}}{\tau_y}$	$\frac{\tau_o}{\tau_y}$	Relevant Quantities Taken From
760	244	0.262	332	88	246	86	0.741	0.977	2.86	3.86	1.01	1.36	Fig. 23(a)
		0.46	344	100	240	104	0.698	1.040	2.31	3.31	0.98	1.41	Fig. 23(b)
		0.65	354	110	236	118	0.667	1.073	2.00	3.00	0.97	1.45	Fig. 23(c)
350	196	0.15	284	88	235	49	0.827	0.557	4.80	5.8	1.20	1.45	Fig. 24(a)
		0.25	294	98	220	74	0.748	0.755	2.97	3.97	1.12	1.50	Fig. 24(b)
		0.312	302	106	209	93	0.692	0.877	2.25	3.25	1.07	1.54	Fig. 24(c)
10 ⁻³	156	0.135	250	94	205	45	0.83	0.48	4.56	5.56	1.314	1.60	Fig. 25(a)
		0.26	268	112	194	74	0.72	0.66	2.62	3.62	1.24	1.71	Fig. 25(b)

TABLE IX - List of Some Parameters Representative of Bauschinger Effect and Hardening for Sequential Reverse Loading on Steel (for the 2nd and 4th loadings)

$\dot{\gamma}$ (s^{-1})	τ_y (MPa)	γ_o	γ_o^+ (MPa)	$\Delta\tau = \tau_o - \tau_y$ (MPa)	τ_{yr} (MPa)	$\tau_o - \tau_{yr}$ (MPa)	$\frac{\tau_{yr}}{\tau_o}$	YSR = $\frac{\tau_{yr}}{\tau_o}$	$\frac{\tau_B}{\Delta\tau}$	$\frac{\tau_{yr}}{\tau_B}$	$\frac{\tau_o}{\tau_B}$	$\frac{\tau_{yr}}{\tau_y}$	$\frac{\tau_o}{\tau_y}$	Relevant Quantities Taken From
760	244	0.262	332	88	246	86	0.741	0.977	2.86	1.01	1.36	-	-	Fig. 23(a)
		-	-	-	-	-	-	-	-	-	-			
		0.46	344	100	240	104	0.698	1.040	2.31	0.98	1.41	-	-	Fig. 23(b)
		1.4	315	71	230	85	0.730	1.197	2.71	0.94	1.29			
		0.65	354	110	236	118	0.667	1.073	2.00	0.97	1.45	-	-	Fig. 23(c)
		1.87	345	101	228	117	0.661	1.158	1.95	0.93	1.41			
350	196	0.15	284	88	235	49	0.827	0.557	4.80	1.20	1.45	-	-	Fig. 24(a)
		0.465	306	110	206	100	0.673	0.909	2.06	1.05	1.56			
		0.25	294	98	220	74	0.748	0.755	2.97	1.12	1.50	-	-	Fig. 24(b)
		0.745	250	94	198	92	0.683	0.979	2.15	1.01	1.48			
		0.312	302	106	209	93	0.692	0.877	2.25	1.07	1.54	-	-	Fig. 24(c)
		0.94	297	101	196	101	0.660	1.0	1.94	1.00	1.51			

+ Represents the maximum stress level reached on the immediate previous loading

TABLE A COMPARISON OF ORIGINALLY PROPOSED MODELS OF POLYMER CREEP

Theory	Stress-Strain Relaxation	Internal State Variable Growth Laws	Comments	Material Parameters
Gernocky and Krenpl	(T1) $\sigma = E(\epsilon - \epsilon_r) e^{-\frac{\sigma}{E}}$	(T2) $\dot{\epsilon}_1 = \frac{\sigma - \sigma_0}{E} e^{-\frac{\sigma}{E}}$	1. $G = G(\epsilon, T)$ is obtained from extrapolation of relaxation data. 2. k is curve-fit to $k = R_0 e^{\frac{R_1}{R_2} \epsilon} - \left[\frac{1 - G}{R_2} \right] R_3$	E, R_0, R_1, R_2, R_3
Krieg, Szwarczenko and Rohde	(T3) $\sigma = E(\epsilon - \epsilon_1)$	(T4) $\dot{\epsilon}_1 = c_1 \left[\frac{1 - \sigma_2}{\sigma_1} \right]^2 \text{sgn}(\sigma - \sigma_2)$ (T5) $\dot{\epsilon}_2 = c_2 c_3 \sigma_1 - c_4 \sigma_2^2 [e^{c_5 \sigma_2^2} - 1] \text{sgn}(\sigma_2)$ (T6) $\dot{\epsilon}_3 = c_6 \dot{\epsilon}_1 - c_7 [\sigma_3 - \sigma_3_0]^n$		$E, c_1, c_2, c_3, c_4, c_5, c_6, c_7, \sigma_2_0, n$
Bodner et al.	(T7) $\sigma = E(\epsilon - \epsilon_1)$	(T8) $\dot{\epsilon}_1 = \frac{2}{3} D_0 e^{-\left[\frac{n+1}{2n} \right] \left[\frac{\sigma}{\sigma_1} \right]^2} \text{sgn}(\sigma)$ (T9) $\dot{\epsilon}_3 = [\sigma_3 - \sigma_3_0] \dot{\epsilon}_2 - A \sigma_1 \left[\frac{\sigma_3 - \sigma_3_0}{\sigma_1} \right]^2$	1. $\dot{\epsilon}_p = \sigma_1^p$	$E, D_0, n, m, Z_1, \sigma_1, A, p$
Walker	(T10) $\sigma = E(\epsilon - \epsilon_1)$	(T11) $\dot{\epsilon}_1 = \dot{\epsilon}_2 \left[\frac{1 - \sigma_2}{\sigma_3} \right]^n \text{sgn}(\sigma - \sigma_2)$ (T12) $\dot{\epsilon}_2 = [n_1 + n_2] \dot{\epsilon}_1 - [2 \sigma_2 - n_1 \sigma_1] \left[\frac{1}{3} \left[(n_3 + n_4) \left(\ln \left(\frac{n_5 R}{1 + n_6} \right) + 1 \right) \right] + n_7 \sigma_2 - \sigma_2_0 ^{m-1} \right]$ (T13) $\dot{\epsilon}_3 = n_8 \dot{\epsilon}_1 - n_9 \dot{\epsilon}_2 \sigma_3 - n_{10} (\sigma_3 - \sigma_3_0)^q$	1. R is the cumulative inelastic strain: $R = \int_0^t \frac{1}{3} \dot{\epsilon}_2 dr$ 2. The growth law for σ_3 , eq. (T13), is not presently used in the model; σ_3 is assumed to be a constant.	$E, n, n_1, n_2, n_3, n_4, n_5, n_6, n_7, n_8, n_9, n_{10}, m, q, \sigma_2_0, \sigma_3_0$
Miller	(T14) $\sigma = E(\epsilon - \epsilon_1) e^{-\frac{\sigma}{E}}$	(T15) $\dot{\epsilon}_1 = \sigma_1 \left[\sinh \left(\frac{\sigma - \sigma_2}{\sigma_1} \right) \right]^{1.5} \text{sgn}(\sigma - \sigma_2)$ (T16) $\dot{\epsilon}_2 = n_1 \sigma_1 - n_1 \sigma_1 \sigma_3 \left[\sinh(\lambda_1 \sigma_2) \right]^n \text{sgn}(\sigma_2)$ (T17) $\dot{\epsilon}_3 = n_2 \dot{\epsilon}_1 [C_2 + \sigma_2 - \frac{A_2}{\lambda_1} \sigma_3^2] - n_2 C_2 \sigma_3 \left[\sinh(\lambda_2 \sigma_3) \right]^n$	1. $\sigma = \sigma_0 e^{-\frac{Q}{RT}}$ for $T > 0.6 T_m$ $\sigma = \sigma_0 e^{-\left[\frac{Q}{RT_m} \right] \left[\ln \left(\frac{0.6T}{T - T_m} \right) + 1 \right]}$ for $T < 0.6 T_m$ T_m is the melting temp. k is the gas constant.	$E, n, n_1, \lambda_1, \lambda_2, C_2, C_3, Q$

Coecotto and Leckle	(T18) $\sigma = E[\epsilon - \sigma_1 - \epsilon^T]$	(T19) $\dot{\epsilon}_1 = \epsilon \left(\left \frac{\sigma - \sigma_2}{\sigma_3} \right \right) \operatorname{sgn}(\sigma - \sigma_2)$ (T20) $\dot{\epsilon}_2 = \frac{3}{2} h_0 \dot{\epsilon}_1 - \epsilon \sigma_2$ (T21) $\dot{\epsilon}_3 = h_0 - \epsilon \sigma_2$	1. $\epsilon, h_0, \sigma_0, h_2,$ and σ_2 are experimentally determined functions.	E
Hart	(T22) $\sigma = E[\epsilon - \sigma_1 - \epsilon^T]$	(T23) $\dot{\epsilon}_1 = \frac{1}{2} \left[\frac{\sigma - \sigma_2}{\sigma_3} \right]^{M/2} \left[\frac{\sigma - \sigma_2}{\sigma_3} \right]^H \operatorname{sgn}(\sigma - \sigma_2)$ (T24) $\dot{\epsilon}_2 = \frac{3}{2} \dot{\epsilon}_1 - \frac{\left[\frac{\sigma_3}{\sigma_2} \right]^M - \frac{\sigma_3}{R}}{\left[\ln \left(\frac{3\sigma_3}{2(\sigma_2)} \right) \right]^{1/\lambda}}$ (T25) $\dot{\epsilon}_3 = \frac{1}{2} \left[\frac{\sigma - \sigma_2}{\sigma_3} \right]^{k/2} \frac{\sigma_3}{\epsilon \sigma_2} \left[\frac{\sigma_3}{\sigma_2} \right]^k \left[\ln \left(\frac{\sigma_3}{2(\sigma_2)} \right) \right]^{1/\lambda}$	1. The drag stress is taken to be a constant, σ_0 , hence there is no σ_3 as in other models. There is, however, a third internal state variable, termed σ_3 . 2. T is the absolute temp. R is the gas constant.	$E, \dot{\epsilon}, M, H,$ $G, m, \epsilon, Q, k,$ λ, C
Robinson	(T26) $\sigma = E[\epsilon - \sigma_1 - \epsilon^T]$	(T27) $\dot{\epsilon}_1 = \frac{1}{2} \left[\frac{\sigma - \sigma_2}{\sigma_3} \right]^{n-1} [\sigma - \sigma_2]$ (T28) $\dot{\epsilon}_2 = \frac{2\nu H}{\left[\frac{1}{\sigma_3} \right]^2} \dot{\epsilon}_1 - R \left[\frac{1}{\sigma_3} \right]^{n-1} \sigma_2$	1. G_0 is the initial value of $\frac{\sigma_2}{\sigma_3}$.	$E, \nu, K, n, s,$ H, R, G_0
Valanis	(T29) $\sigma = E[\epsilon - \sigma_1 - \epsilon^T]$	(T30) $\dot{\epsilon}_1 = k_1 \epsilon_1(\sigma, \dot{\epsilon}) + k_2 \epsilon_2(\sigma, \epsilon)$	1. Represents simplified form of Valanis' model.	E, k_1, k_2, f_1, f_2
Allen and Haisler	(T31) $\sigma = E[\epsilon - \sigma_1 - \epsilon^T]$	(T32) $\dot{\epsilon}_1 = i[\sigma - \sigma_2] + \dot{\epsilon}[\sigma - \sigma_2]$ (T33) $\dot{\epsilon}_2 = \dot{\epsilon} \sigma_2[\sigma - \sigma_2]$ (T34) $\dot{\epsilon}_3 = \dot{\epsilon} \left(\frac{\sigma_2}{\sigma_1} \right)$	1. Considerable curve-fitting and interpolation of stress-strain and creep data required to obtain material parameters $i, \dot{\epsilon},$ and $\dot{\nu}$.	$E, i, \dot{\epsilon}, \nu, f$

$$1 \operatorname{sgn}(x) = \begin{cases} 1 & x > 0 \\ 0 & x = 0 \\ -1 & x < 0 \end{cases}$$

2. $\dot{\epsilon}_1$ can be substituted directly into growth law for σ_2 and σ_3 to obtain a form consistent with internal state variable growth laws (16).

Note: parentheses () imply "function of", whereas brackets [] imply multiplication.

TABLE XI Ability of Viscoplastic Constitutive Equations to Model Certain Phenomena (Beek, Allen and Milly /50/)

Theory	Unified Creep-Plasticity	History Dependence	Bauschinger Effect	Temperature Dependence ¹	Anelasticity	Multiaxial Representation
Cernocky and Krempl	X			X		X
Krieg, Swarengen, and Rohde	X	X	X	X	X	X
Rodner et al.	X	X				X
Walker	X	X	X		X	X
Miller	X	X	X	X	X	
Gescotto and Leckie	X	X	X	X	X	
Hart	X	X	X	X	X	X
Robinson	X	X	X		X	X
Valanis ²	X			X		X
Allen and Haisler		X	X	X	X	X

¹To these authors' knowledge only Allen & Haisler's model has been utilized to predict transient temperature phenomena.

²Consider only the simplified model discussed herein.

TABLE XII Required Material Parameter Characterization in Various Viscoplastic Constitutive Equations (Beek, Allen and Milly /50/)

Cernocky and Kremp1	Constant Strain Rate Tensile Tests with Intermittent Hold Times Relaxations Tests
Krieg, Swarengen, and Rohde	Stress Drop Tests Constant Strain Rate Tensile Tests
Bodner <u>et al.</u>	Constant Strain Rate Tensile Tests Creep Tests
Walker	Constant Strain Rate Cyclic Tests Constant Strain Rate Tensile Tests
Miller	Creep Tests Constant Strain Rate Cyclic Tests Constant Strain Rate Tensile Test
Cescotto and Leckie	Constant Strain Rate Cyclic Tests Constant Strain Rate Tensile Tests Stress Drop Tests
Hart	Relaxation Tests
Robinson	Stress Drop Tests
Valanis	Constant Strain Rate Tensile Test*
Allen & Haisler	Constant Strain Rate Tensile Tests At Several Constant Temperatures Creep Tests At Several Constant Temperatures Single Cycle Strain Controlled Test At Each Constant Temperature

* Represents Simplest Rate Independent Form Of The Model

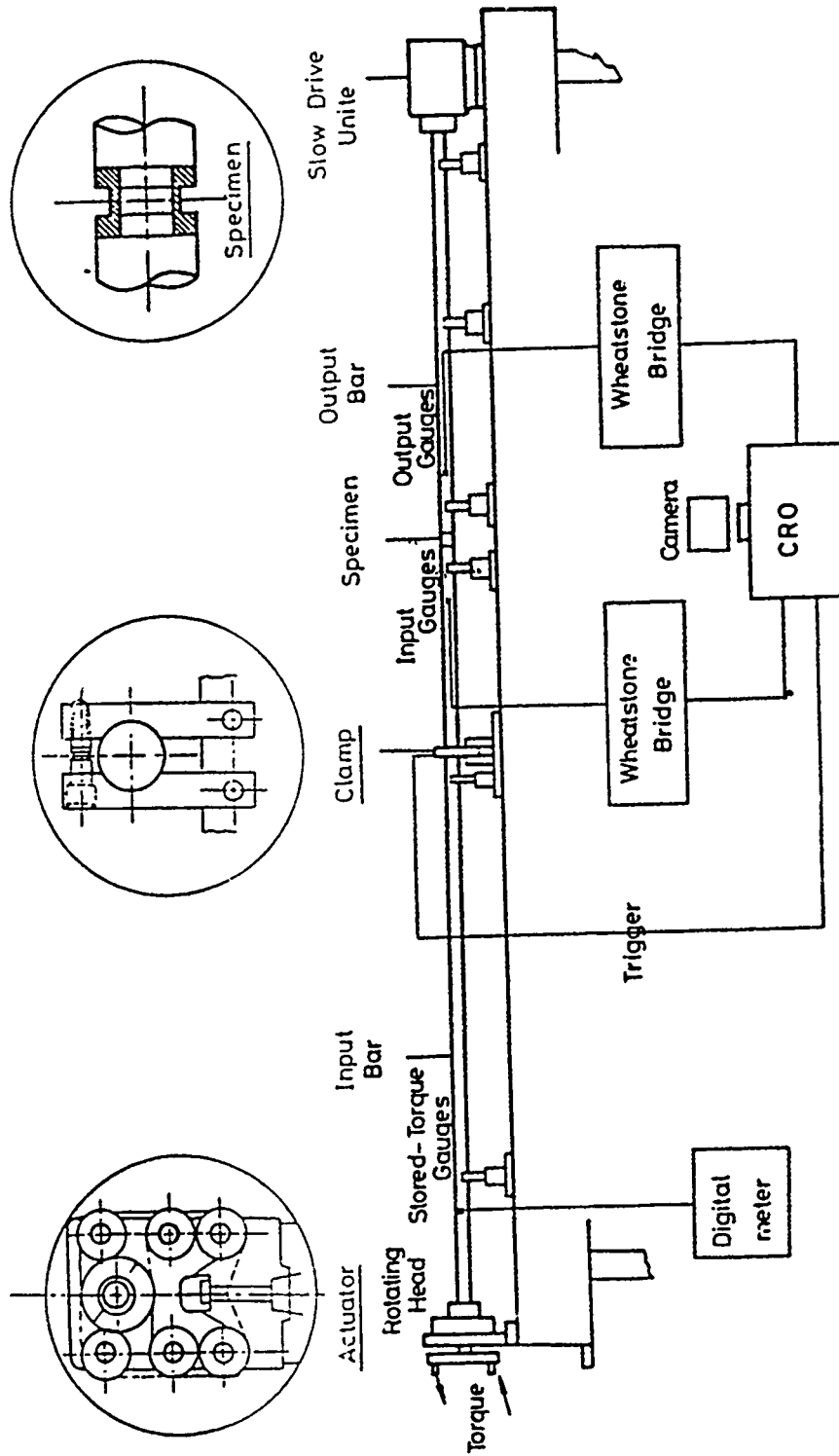


Fig. 1 Schematic drawing of torsional SHB with insets showing various details

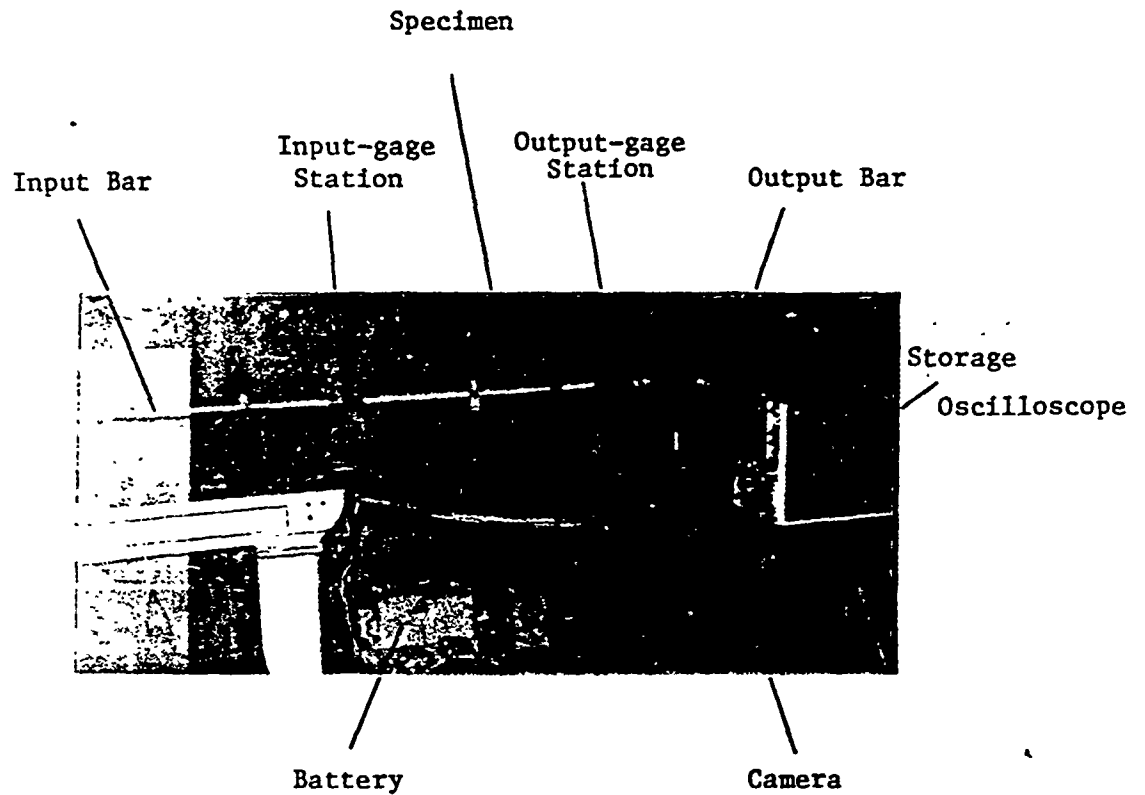


Fig. 2 Closeup of CRO and related instrumentation

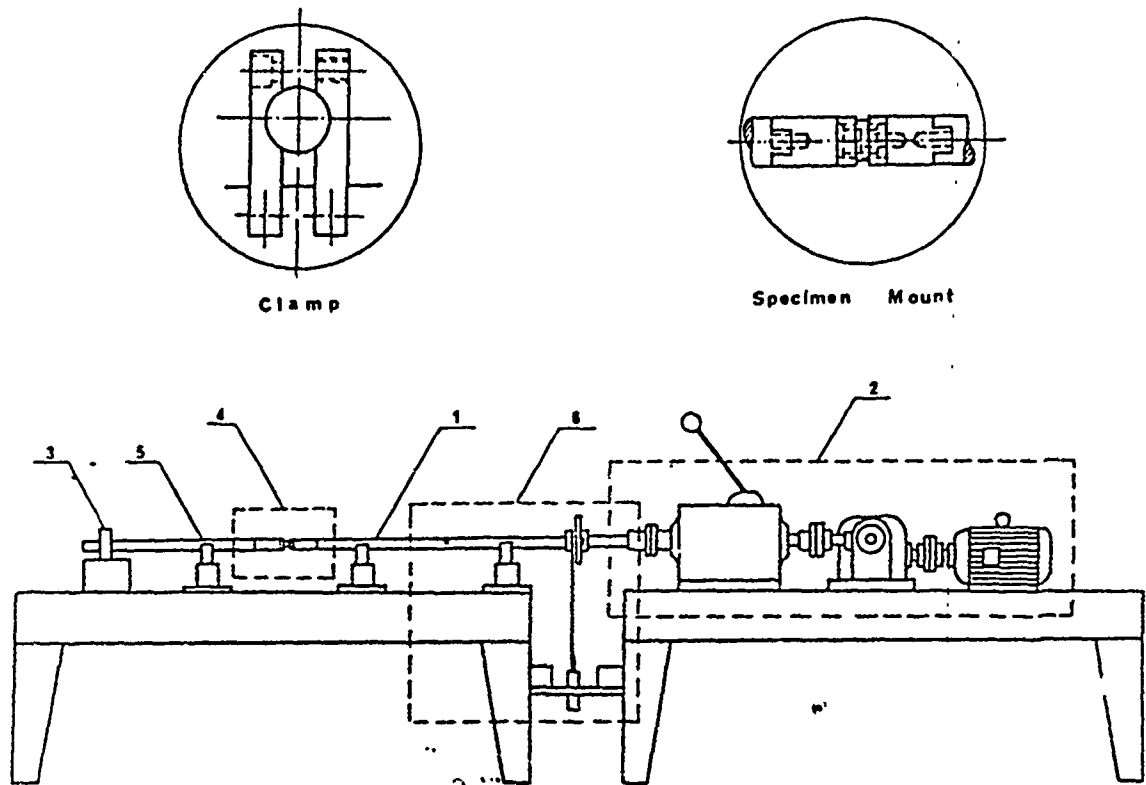


Fig. 3 Schematic drawing of quasi-static torsional apparatus

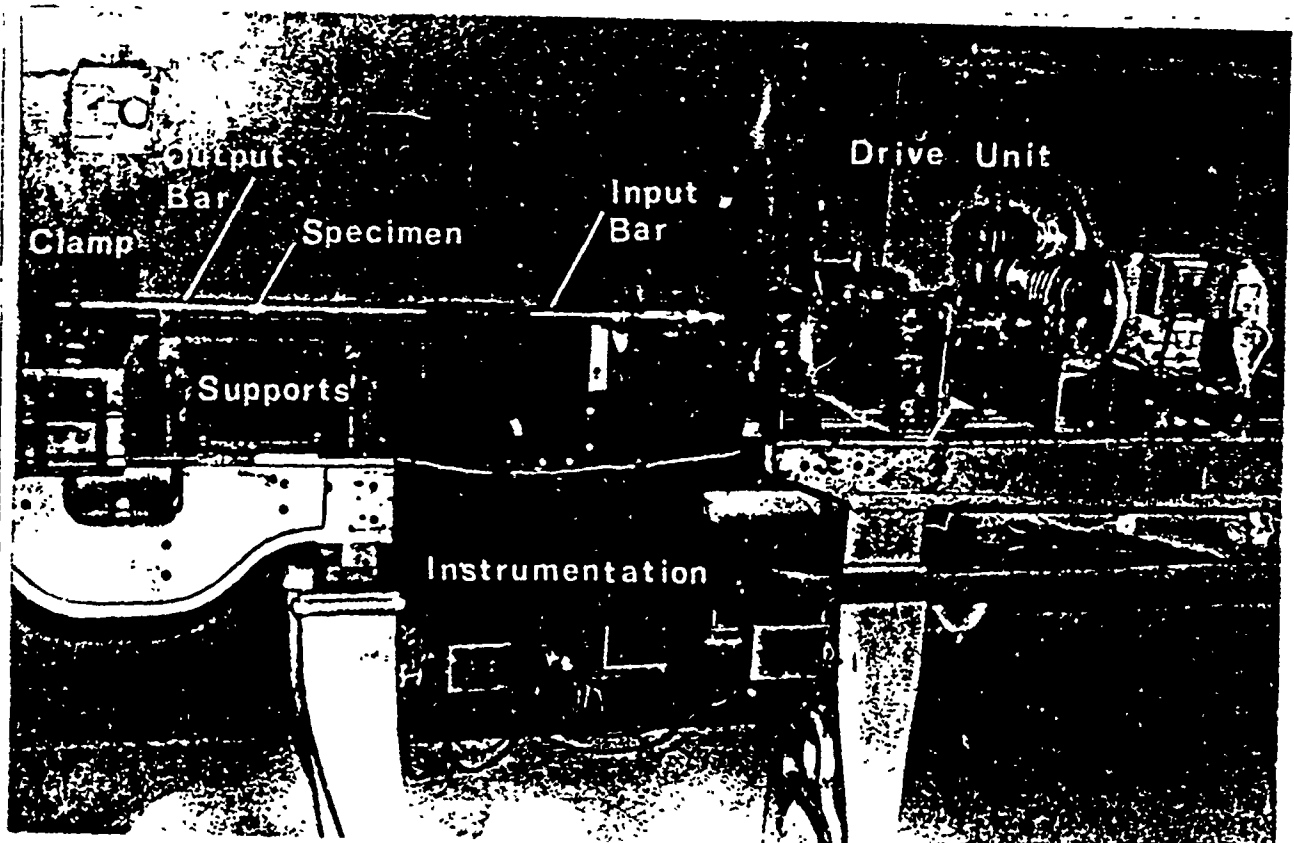


Fig. 4 General view of quasi-static torsional apparatus

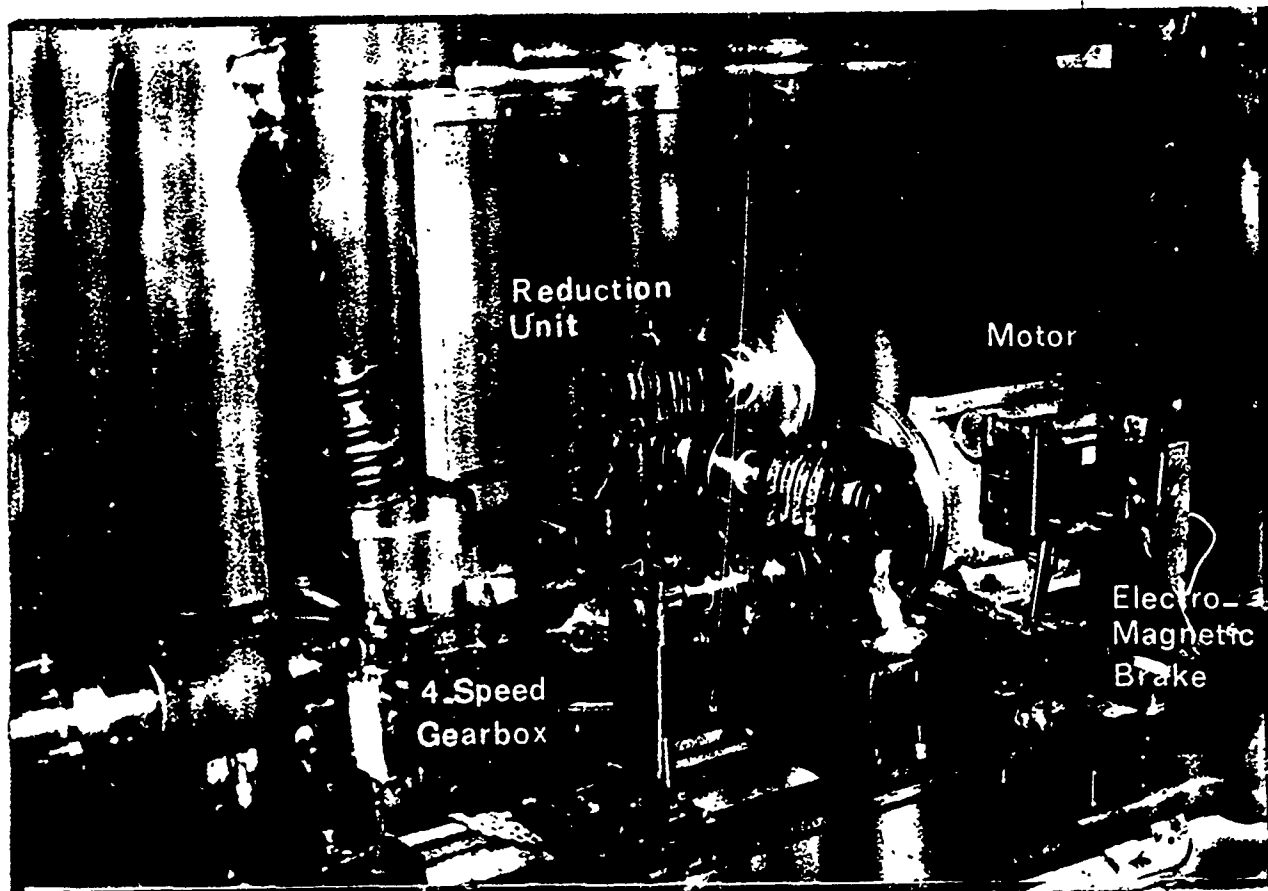


Fig. 5 General view of quasi-static rotational drive unit

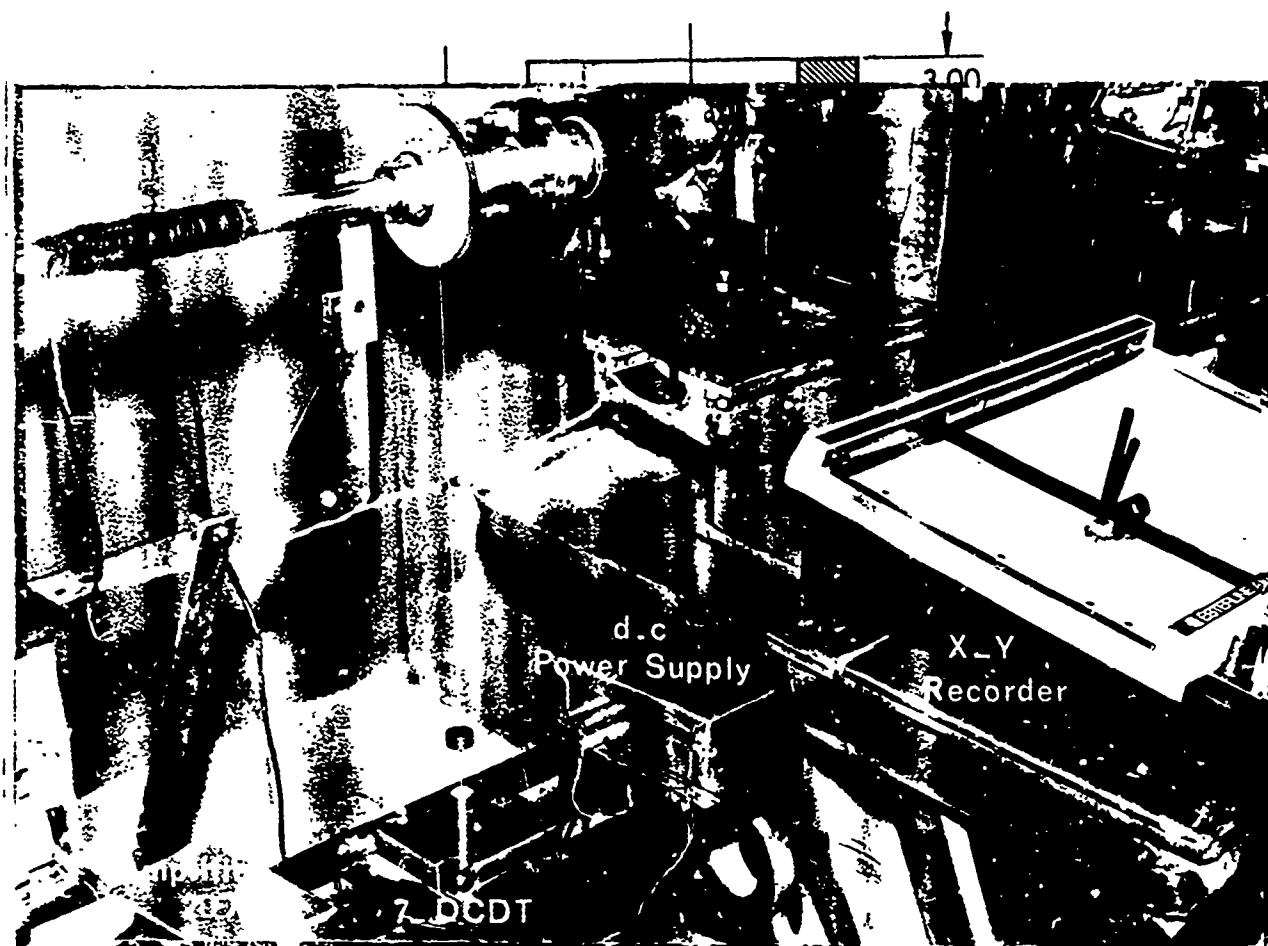
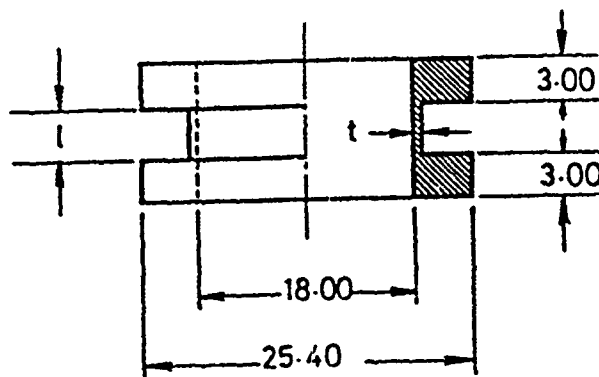


Fig. 6 Overall view of the instrumentation used in quasi-static testing

	l	t	
		Dynamic	Static
Copper	1.1 or 3.0	0.50	0.50
Mild Steel	1.1 or 3.0	0.26-0.29	0.42



Dimensions in mm

Fig. 7 Configuration and nominal dimensions of test specimens

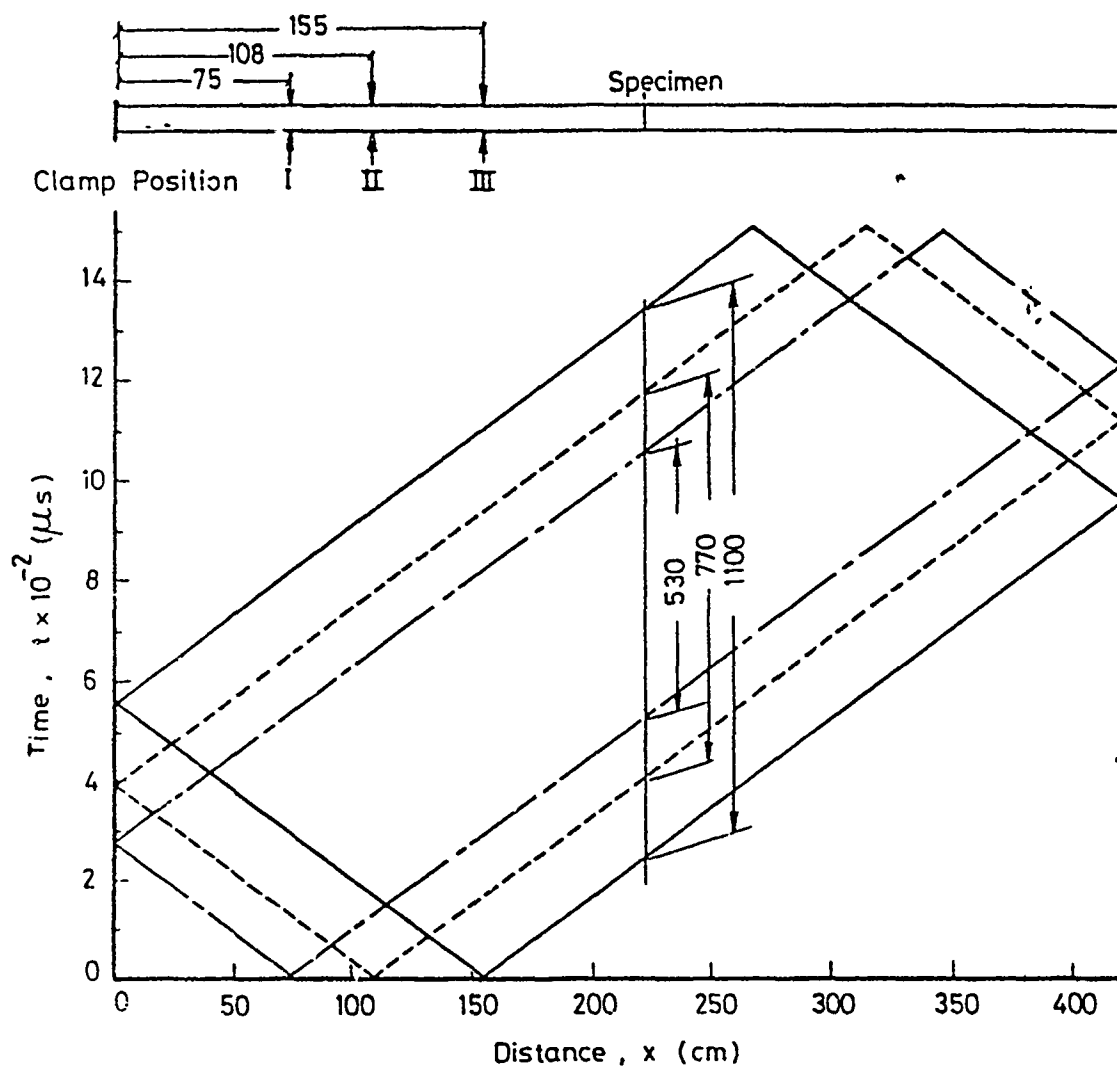
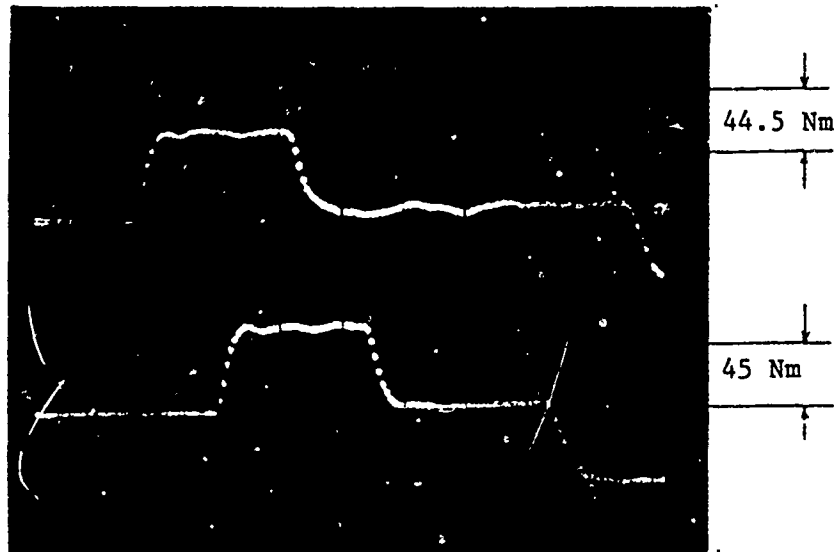
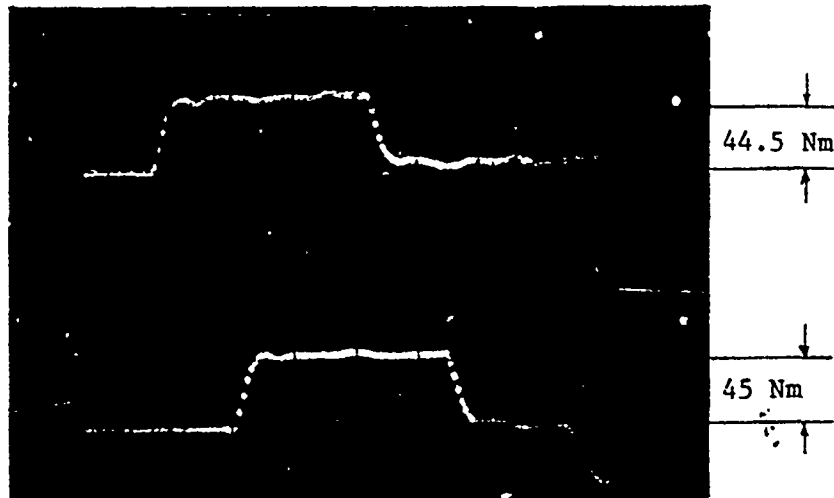


Fig. 8 Characteristic x-t diagrams showing locations of clamp in positions I, II and III and corresponding useful pulse durations

(a)



(b)



(c)

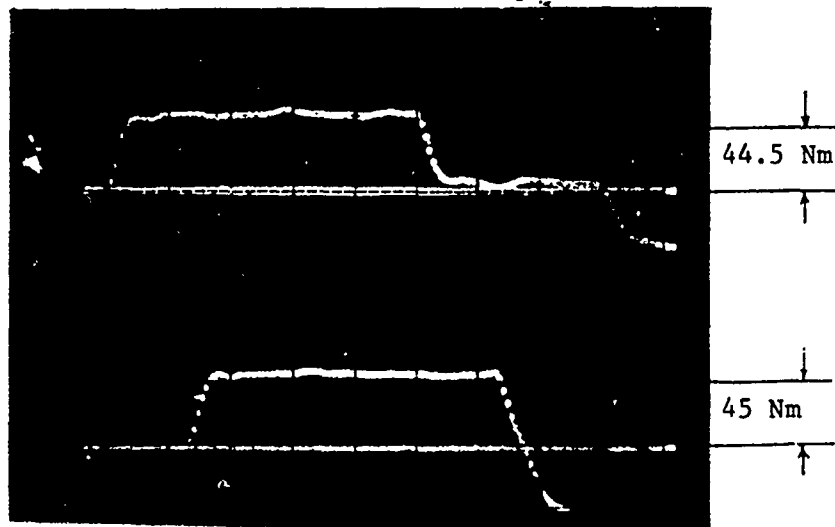


Fig. 9 Experimental Verifications of calculated useful pulse durations for the clamp at positions I, II and III, using a dummy specimen

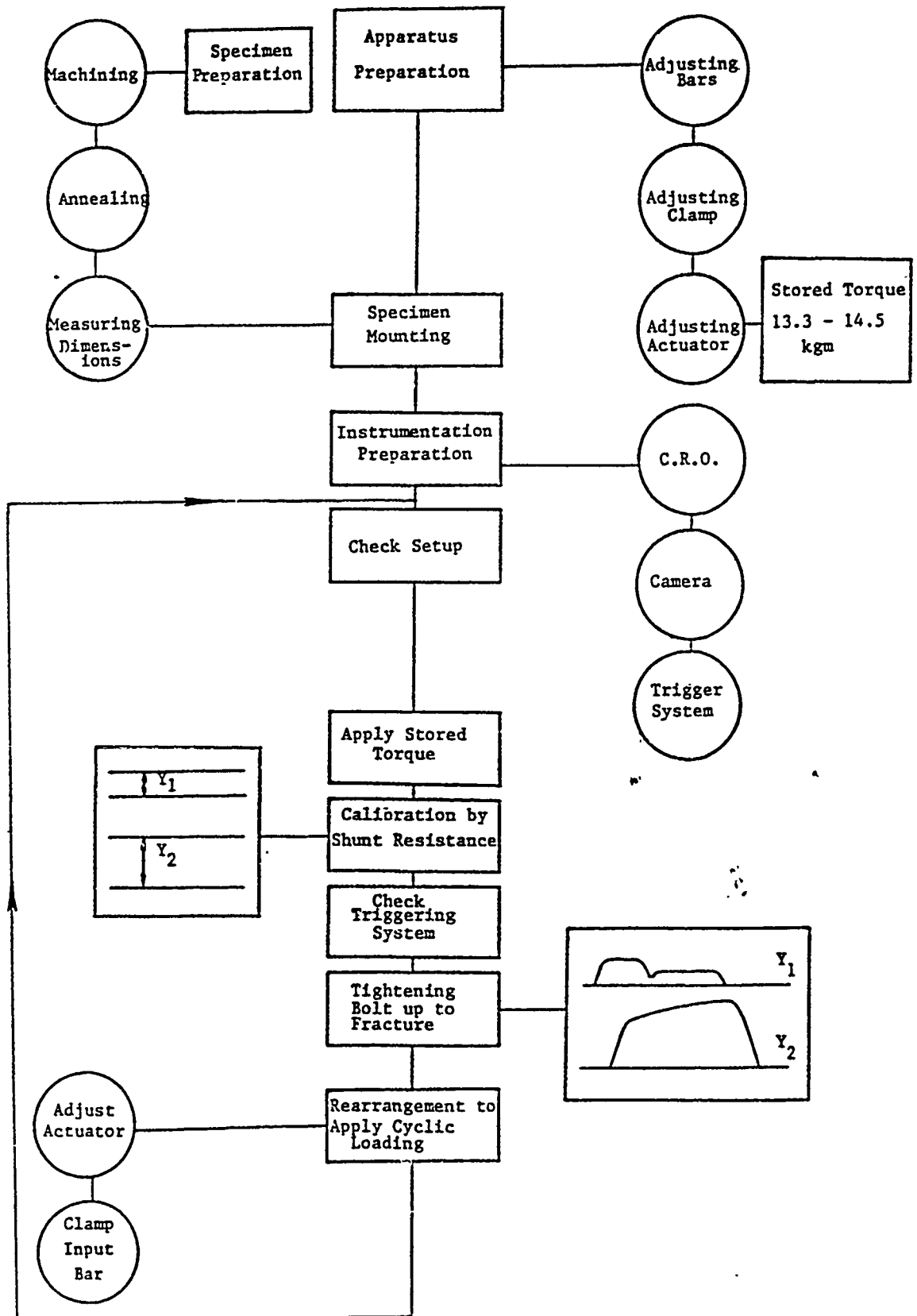


Fig. 10 Flow chart summarizing the procedure used in sequential reverse impact loading tests on the SHB

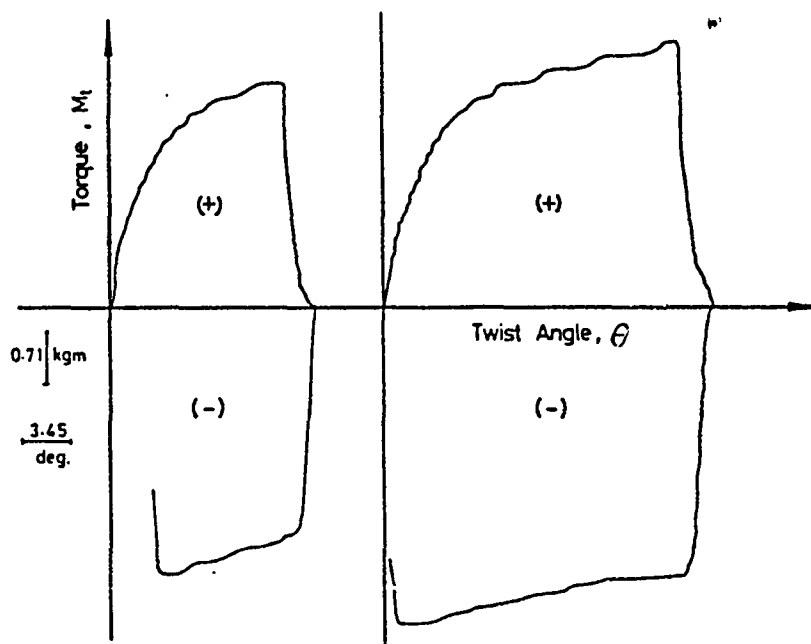


Fig. 11 Typical records of quasi-static reverse loading on copper specimens

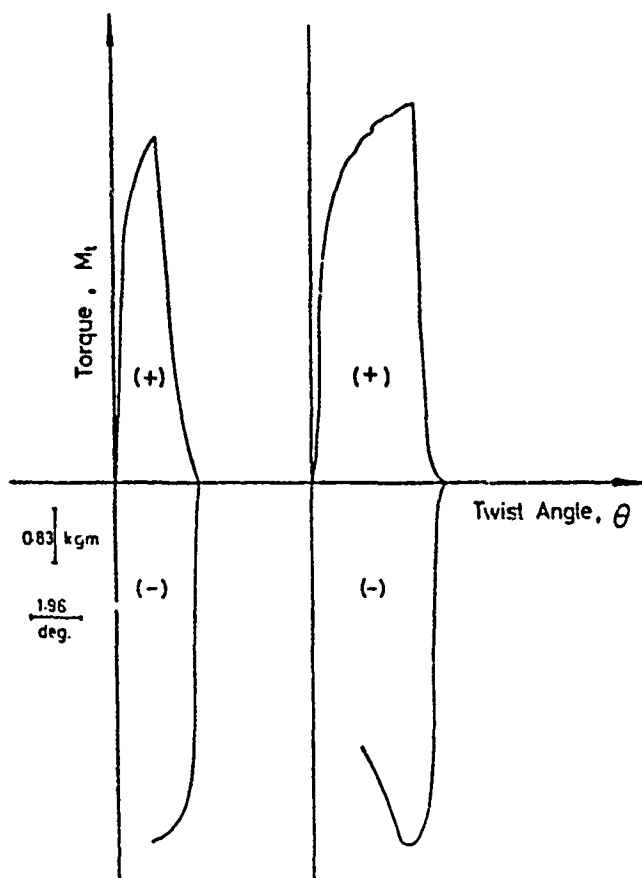

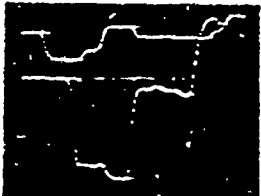
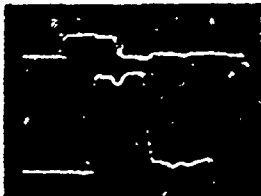


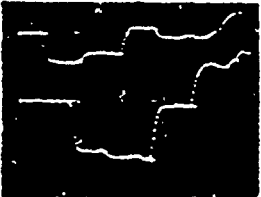
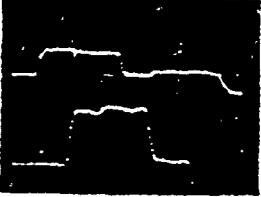
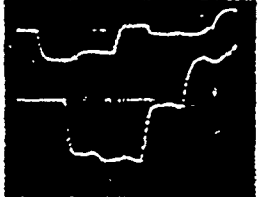

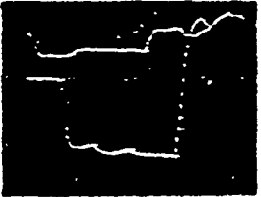
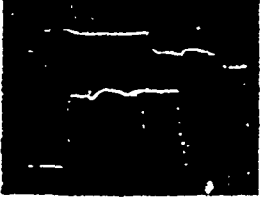

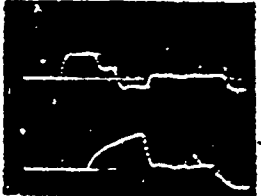
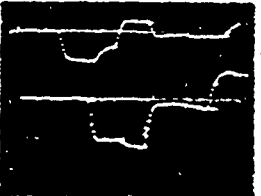
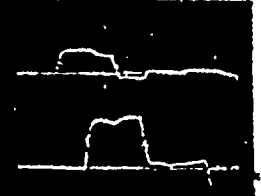
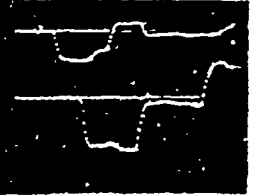

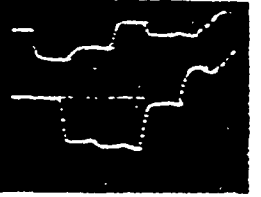


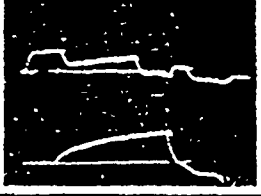

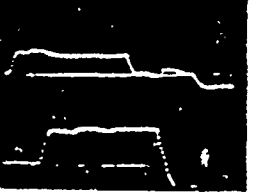
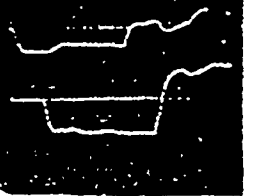


Fig. 12 Typical records of quasi-static reverse loading on steel specimens

OFHC COPPER

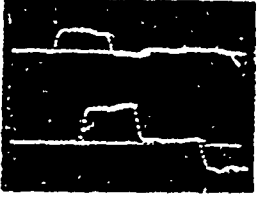
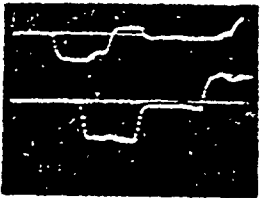
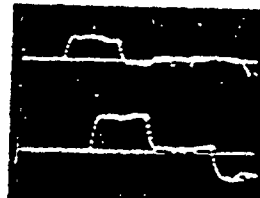
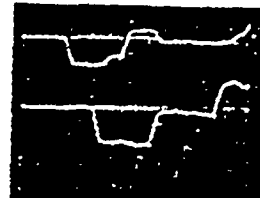
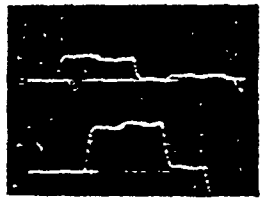
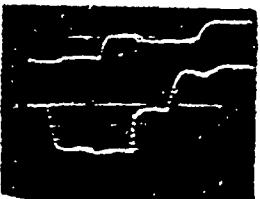

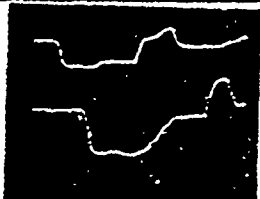



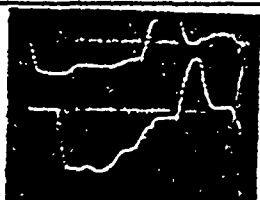
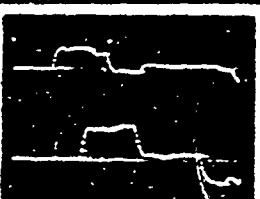
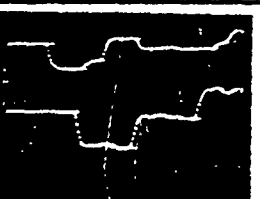
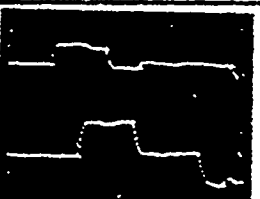



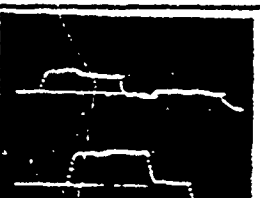



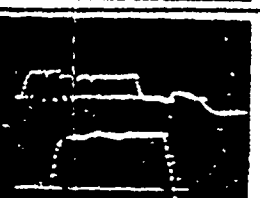

Nominal Gage Length (mm)	Clamp Position	Useful Loading Time (μ s)	Sequential Loading			
			1 Forward	2 Reverse	3 Forward	4 Reverse
1.1	I	A 530				
	II	B 770				
	III	C 1100				
3.0	I	D 530				
	II	E 770				
	III	F 1100				

I One division
on horizontal scale

I One division
on vertical scale

Fig. 13 Typical oscilloscope records of impact reverse loading on copper specimens

MILD STEEL

Nominal Gage Length (mm)	Clamp Position	Useful Loading Time (μ s)	Sequential Loading			
			1 Forward	2 Reverse	3 Forward	4 Reverse
1.1	I	A 530				
	II	B 770				
	III	C 1100				
3.0	I	D 530				
	II	E 770				
	III	F 1100				

I One division
on horizontal scale

I One division
on vertical scale

Fig. 14 Typical oscilloscope records of impact reverse loading on steel specimens

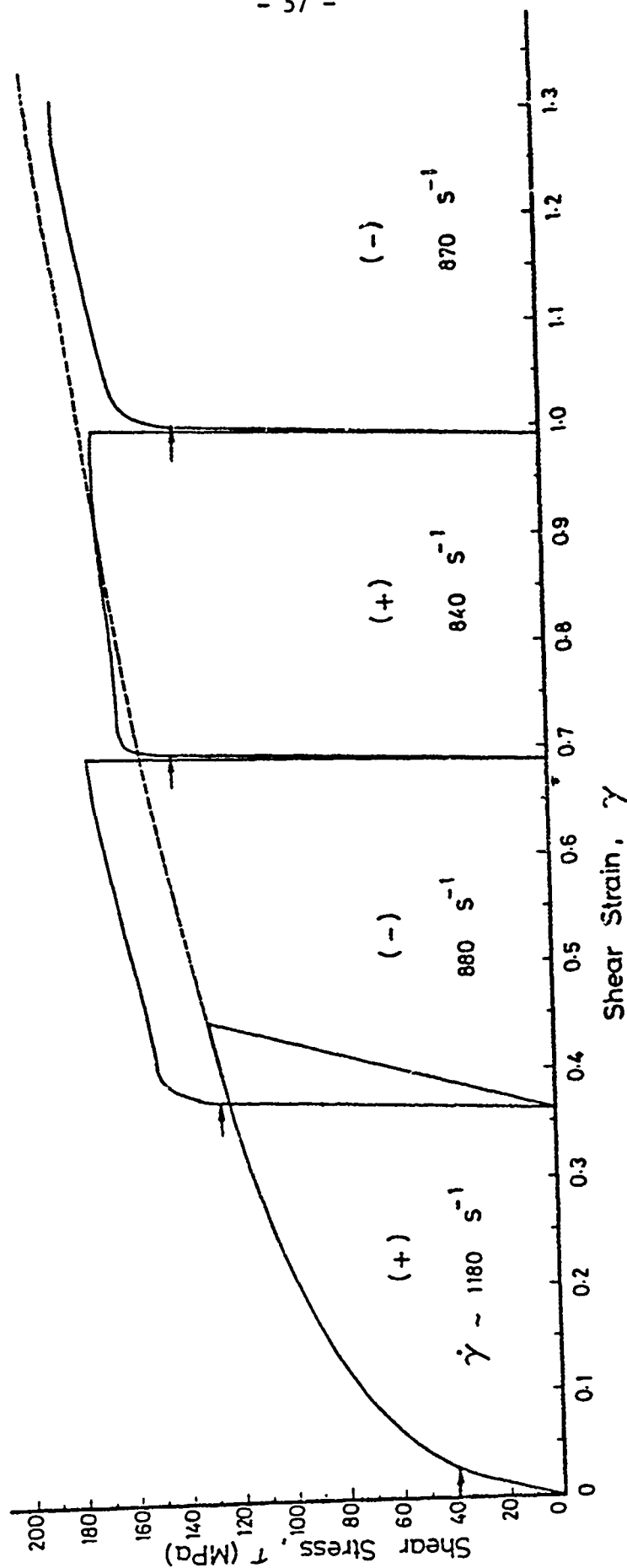


Fig. 15(a) Stress-strain curves for copper under sequential reverse loading at $\dot{\gamma} \sim 1100 \text{ s}^{-1}$, for a constant strain amplitude $\gamma_0 \sim 0.45$

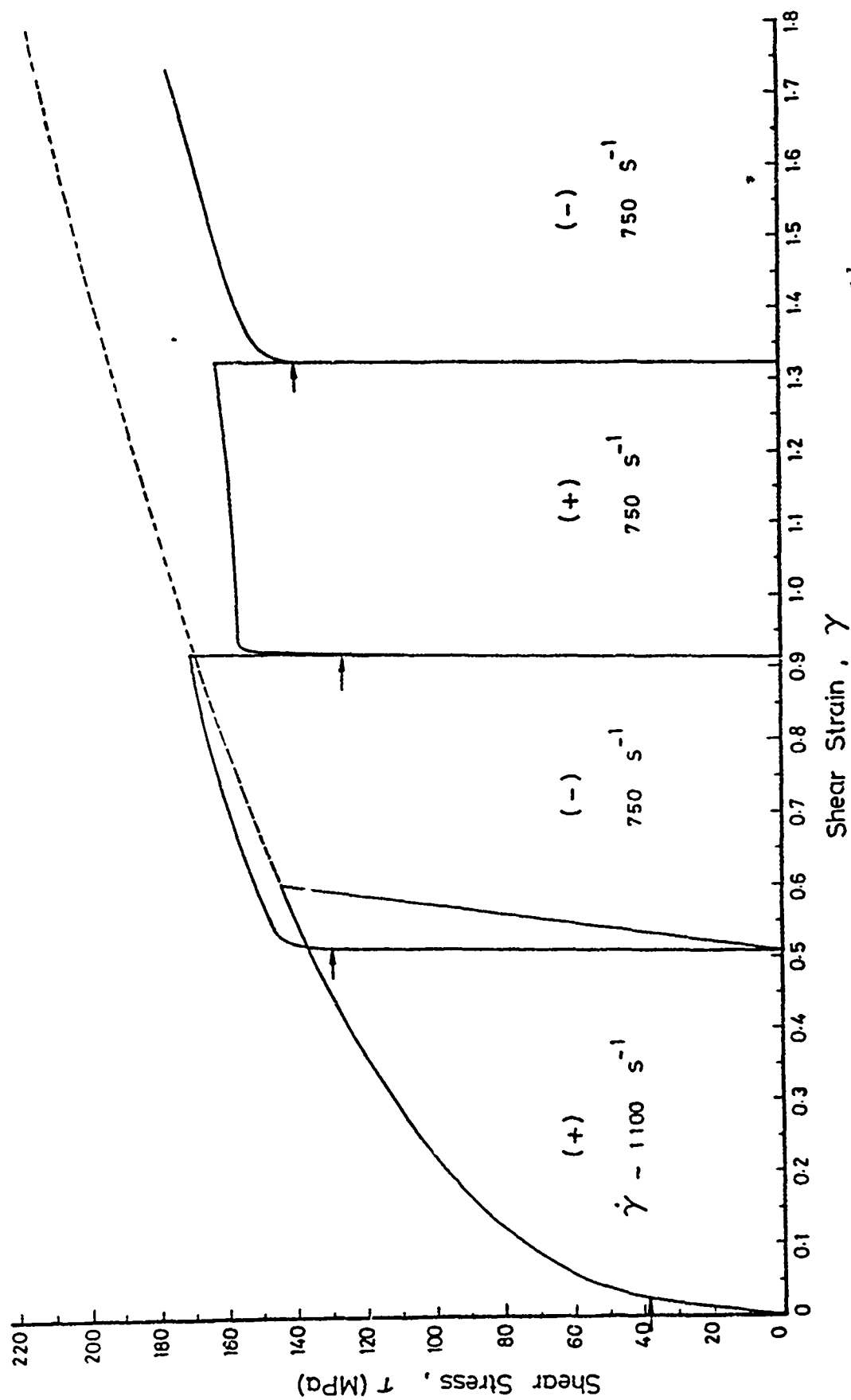


Fig. 15(b) Stress-strain curves for copper under sequential reverse loading at $\dot{\gamma} \sim 1100 \text{ s}^{-1}$, for a constant strain amplitude $\gamma_0 \sim 0.60$

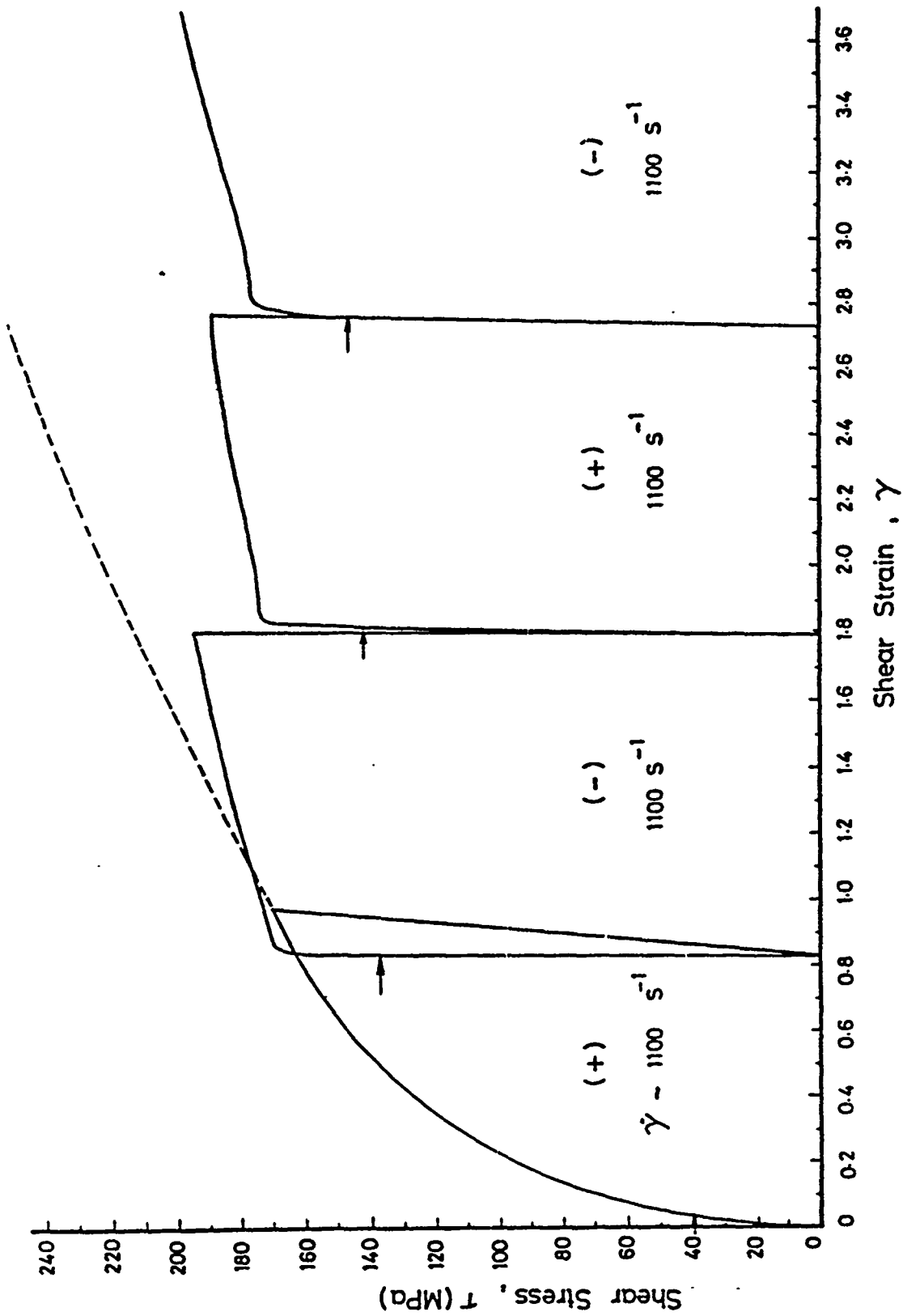


Fig. 15(c) Stress-strain curves for copper under sequential reverse loading at $\dot{\gamma} \sim 1100 \text{ s}^{-1}$, for a constant strain amplitude $\gamma_0 \sim 0.97$

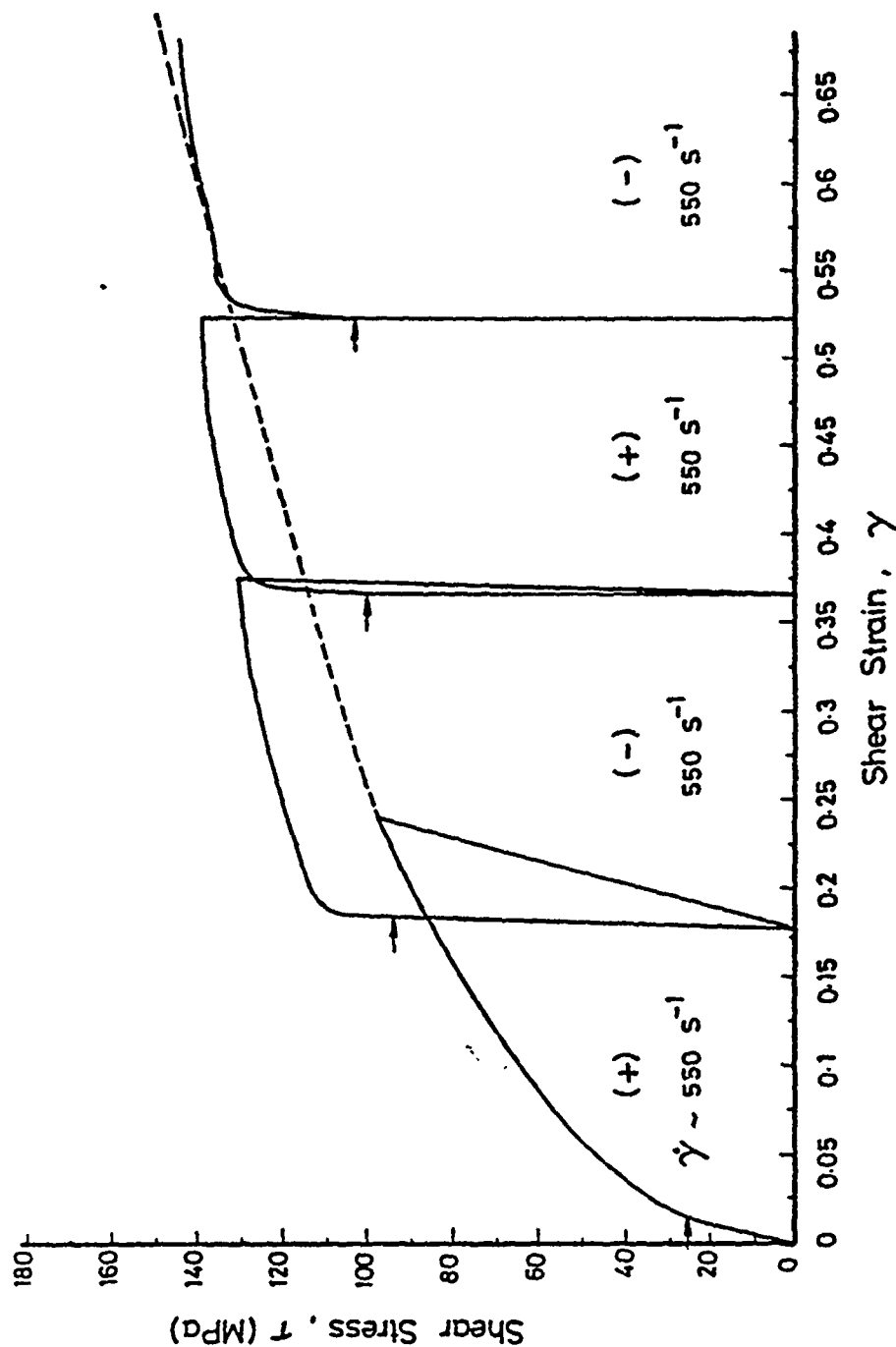


Fig. 16(a) Stress-strain curves for copper under sequential reverse loading at $\dot{\gamma} \sim 550$, for a constant strain amplitude $\gamma_0 \sim 0.24$

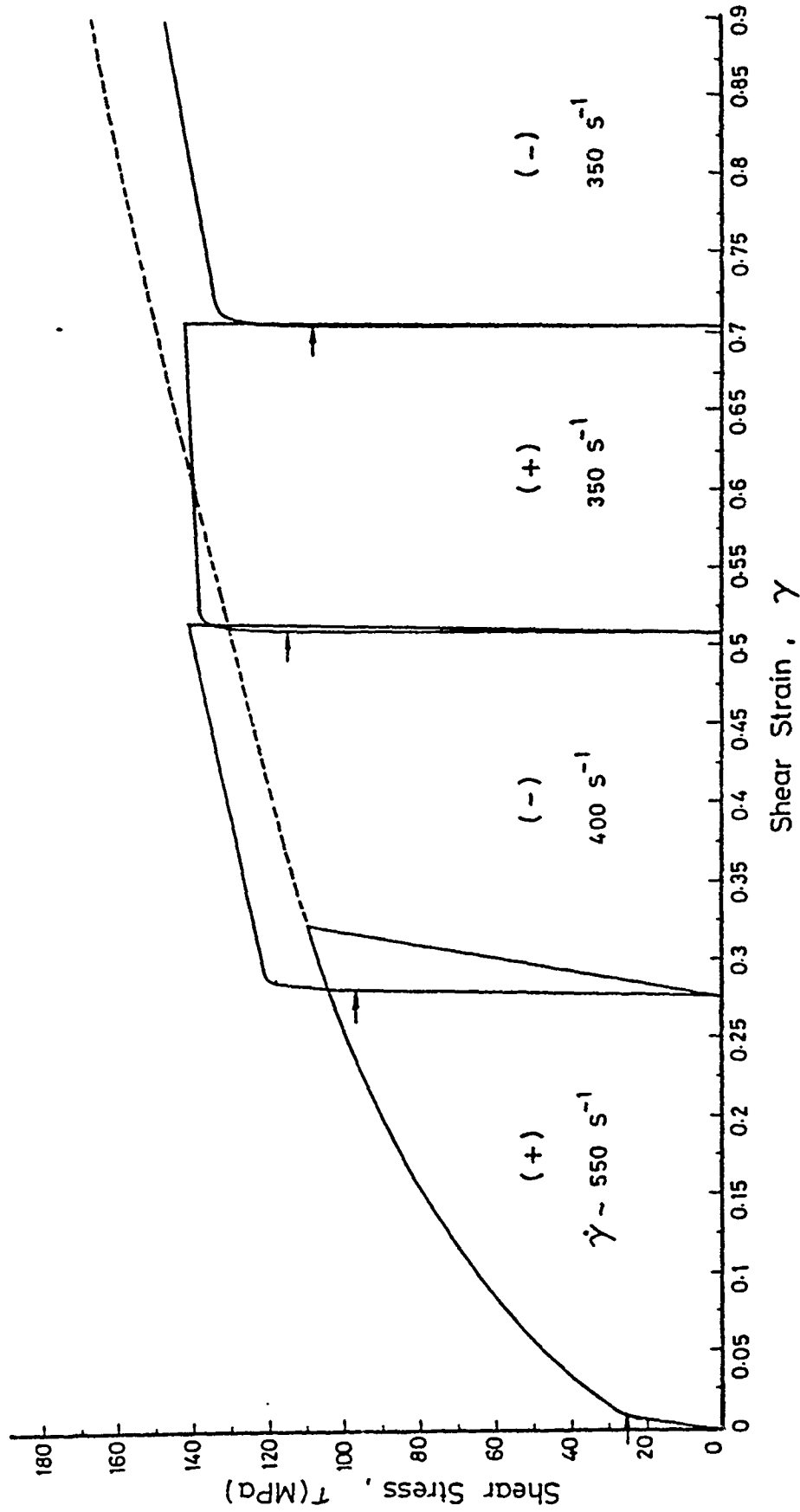


Fig. 16(b) Stress-strain curves for copper under sequential reverse loading at $\dot{\gamma} \sim 550 \text{ s}^{-1}$, for a constant strain amplitude $\gamma_0 \sim 0.32$

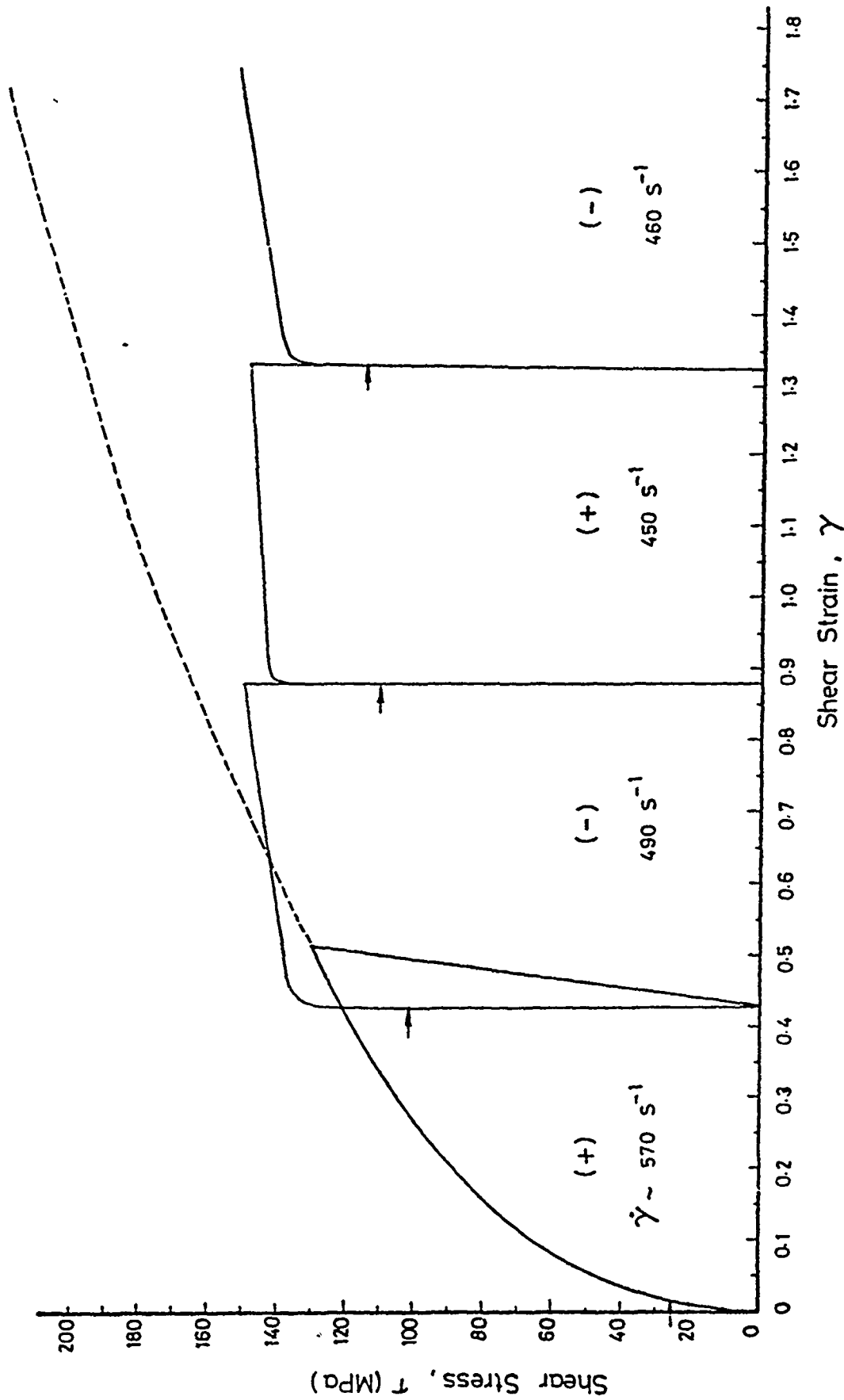


Fig. 16(:) Stress-strain curves for copper under sequential reverse loading at $\dot{\gamma} \sim 550 \text{ s}^{-1}$, for a constant strain amplitude $\gamma_0 \sim 0.508$

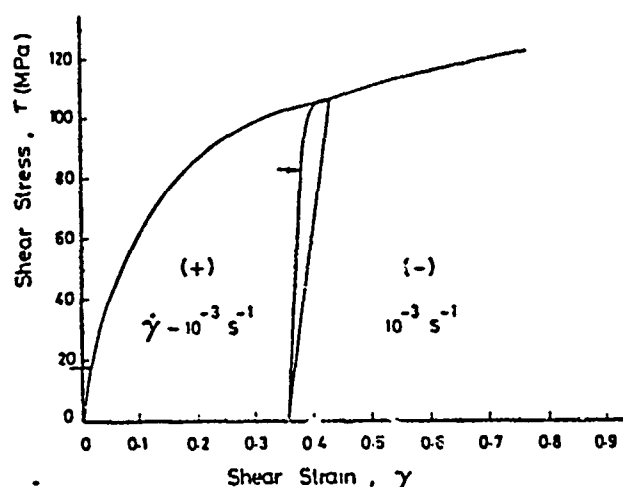


Fig. 17(a) Stress-strain curves for copper under forward and reverse loading at $\dot{\gamma} = 10^{-3} \text{ s}^{-1}$, for a constant strain amplitude $\gamma_0 \sim 0.43$

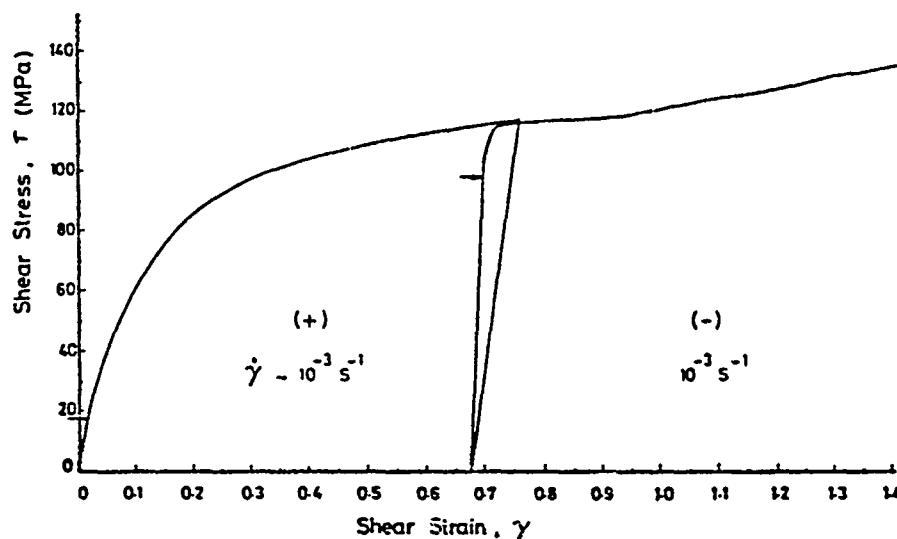


Fig. 17(b) Stress-strain curves for copper under forward and reverse loading at $\dot{\gamma} = 10^{-3} \text{ s}^{-1}$, for a constant strain amplitude $\gamma_0 \sim 0.76$

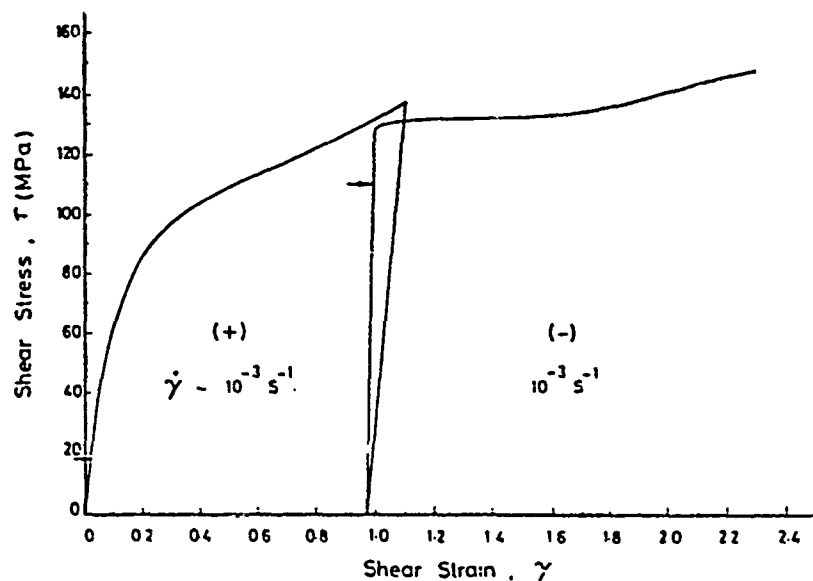


Fig. 17(c) Stress-strain curves for copper under forward and reverse loading at $\dot{\gamma} = 10^{-3} \text{ s}^{-1}$, for a

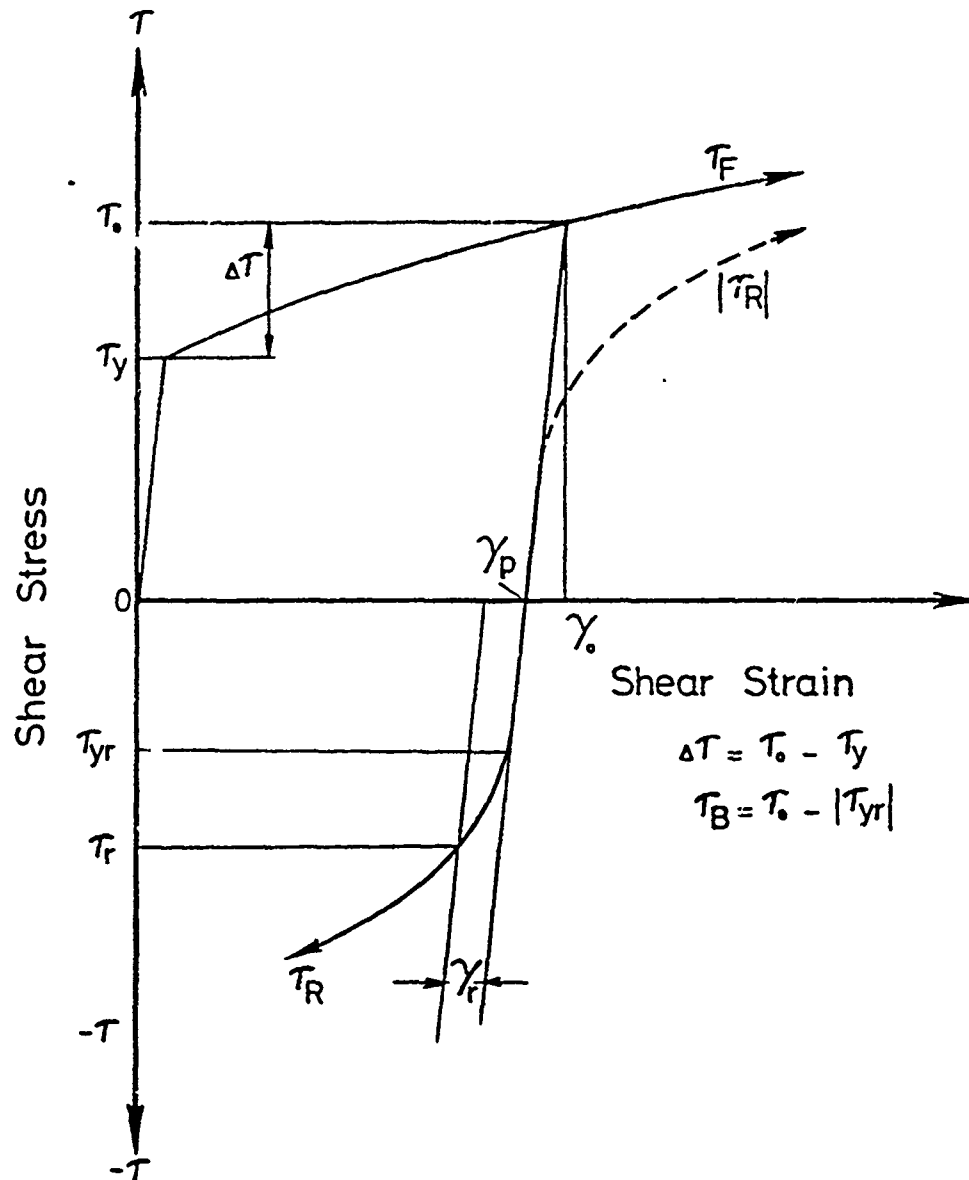


Fig. 18 Definition of terms used in describing the Bauschinger effect phenomenon

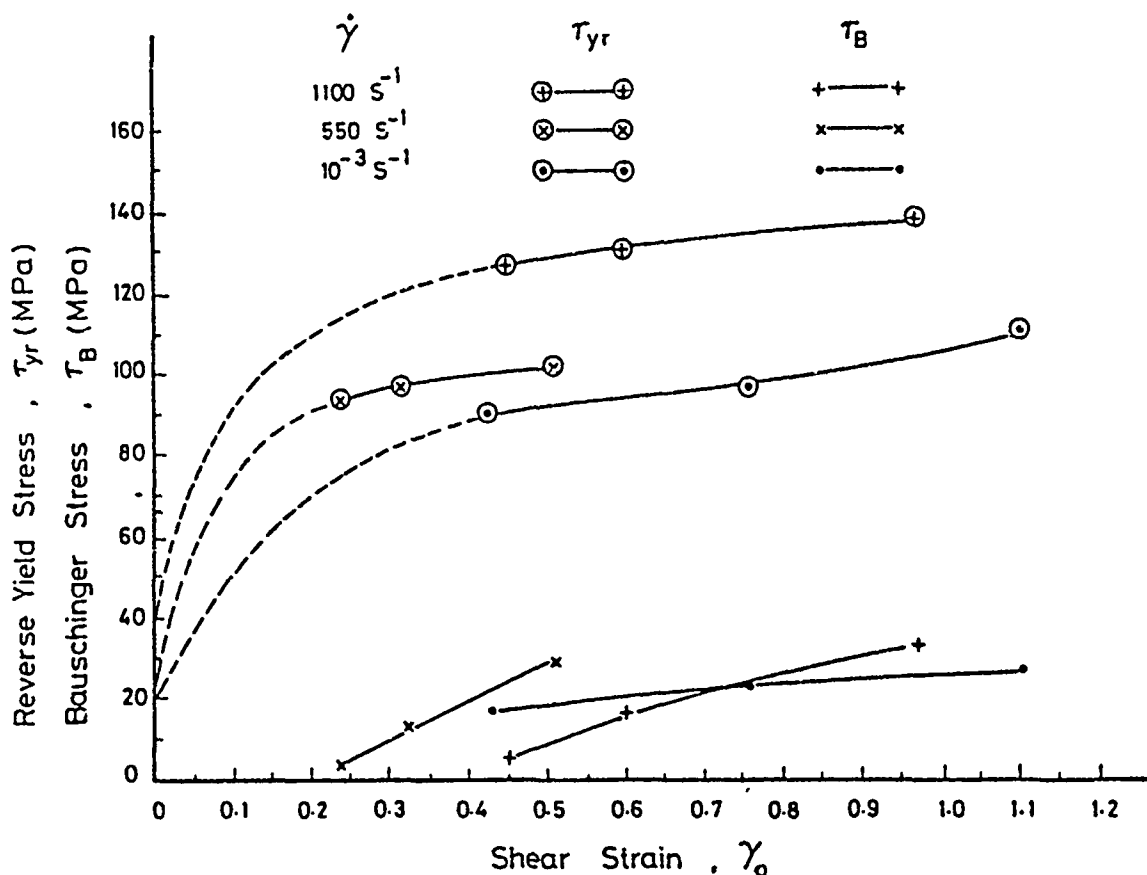


Fig. 19 Variation of reverse yield stress, τ_{yr} , and Bauschinger stress, τ_B , for copper, with strain amplitude, γ_o , for various strain rates

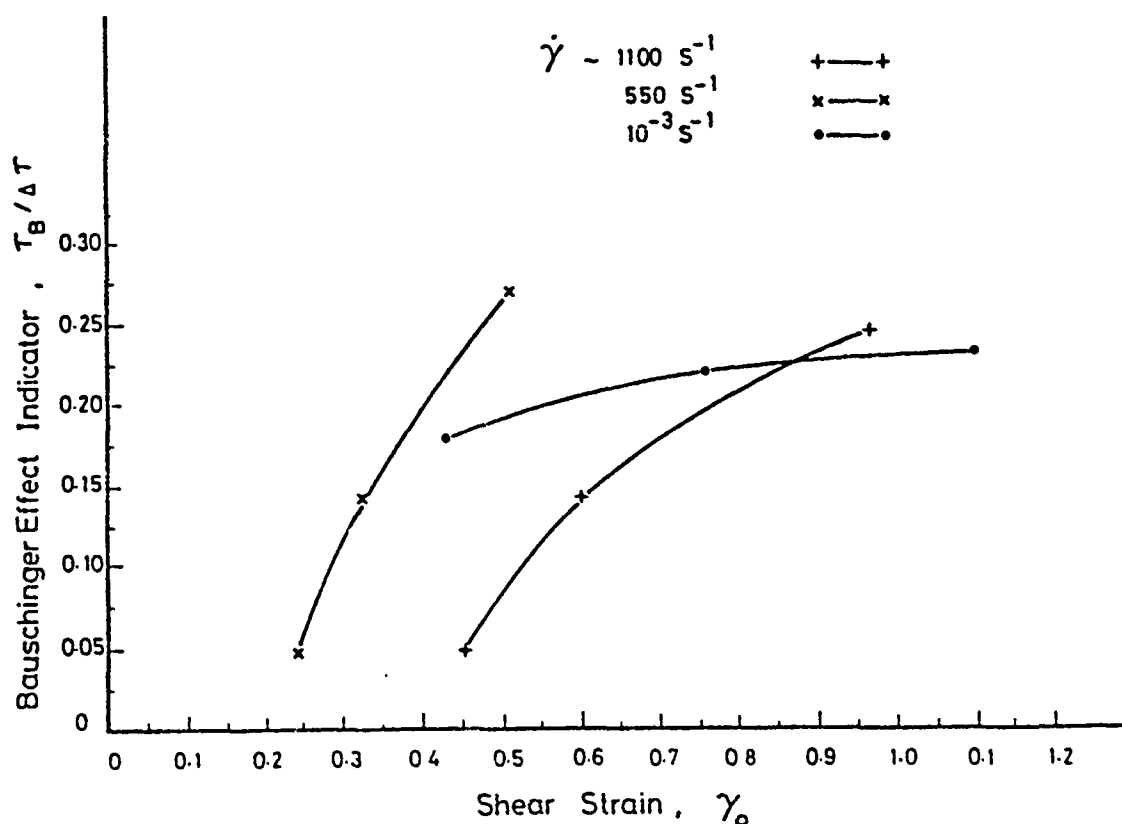


Fig. 20 Variation of Bauschinger effect indicator, $\tau_B / \Delta \tau$, for copper, with strain amplitude, γ_o , for various strain rates

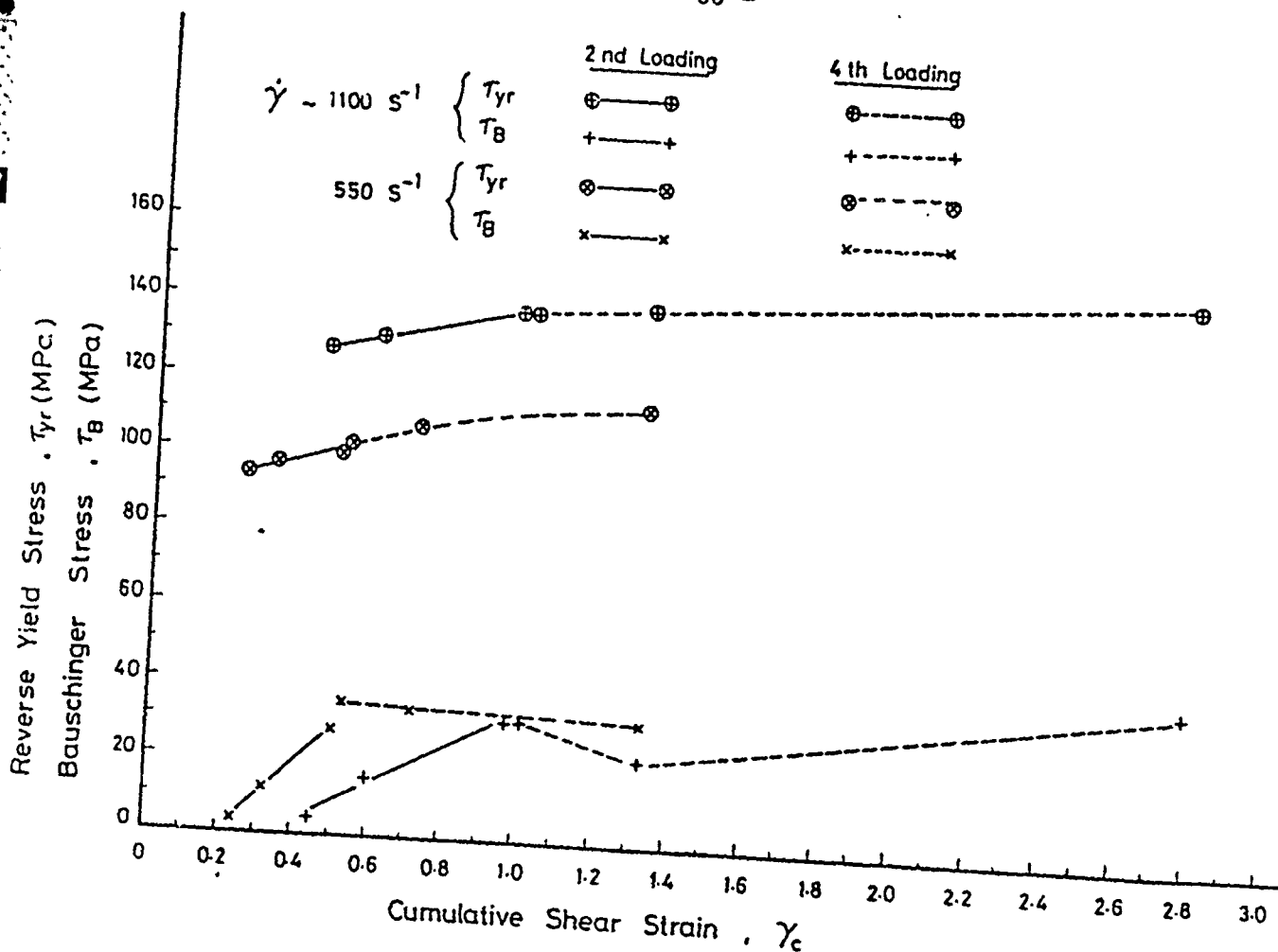


Fig. 21 Variation of reverse yield stress, τ_{yr} , and Bauschinger stress, τ_B , for copper, with cumulative strain, γ_c , for various strain rates

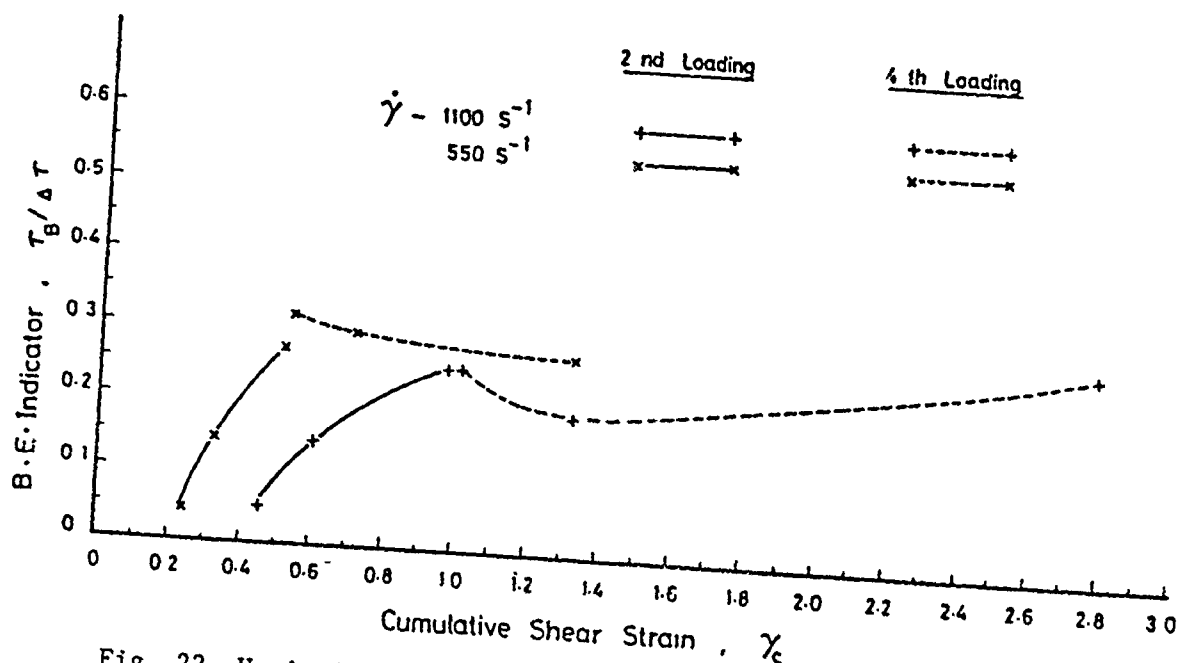


Fig. 22 Variation of Bauschinger effect indicator, $\tau_B / \Delta \tau$, for copper, with cumulative strain, γ_c , for various strain rates

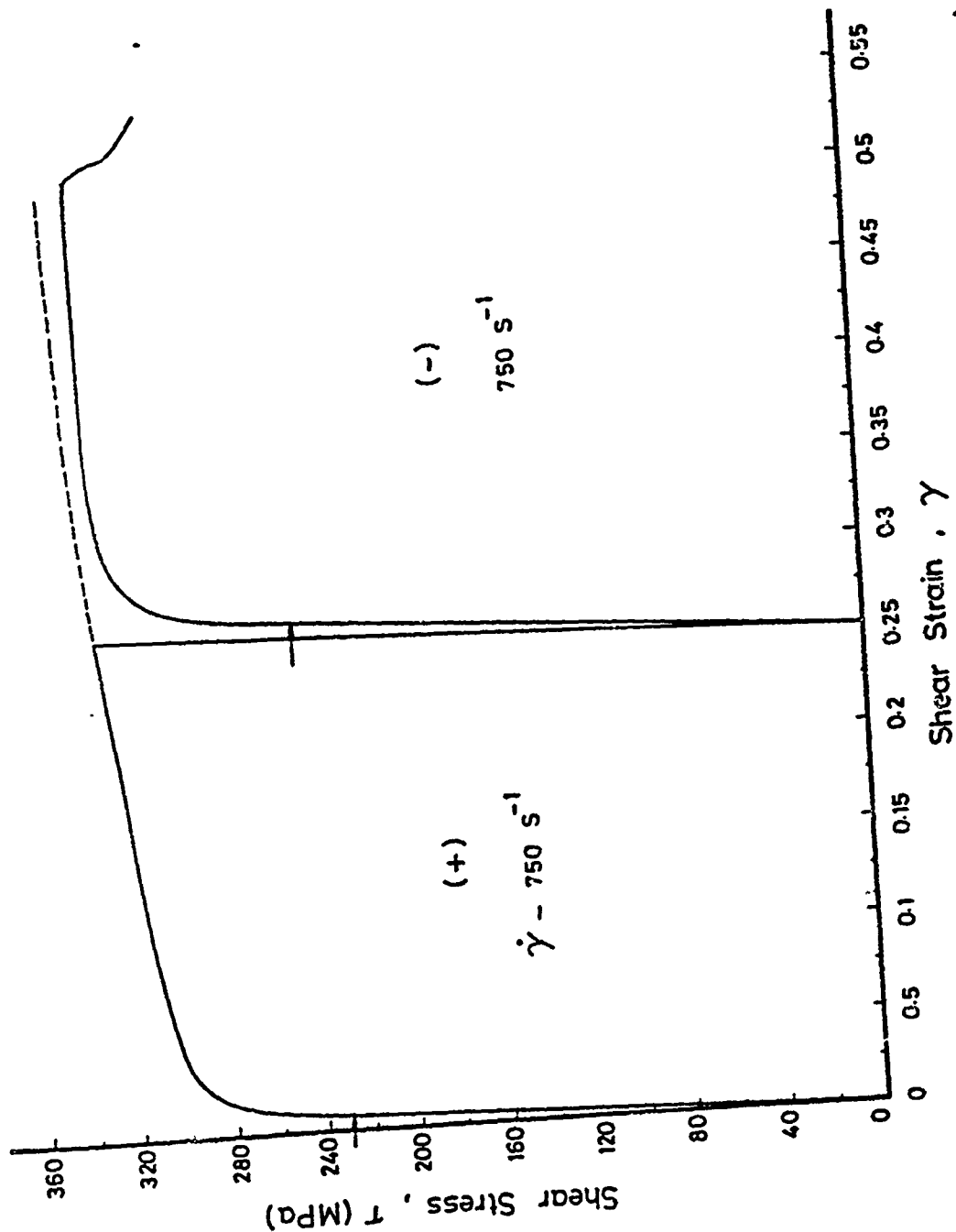


Fig. 23(a) Stress-strain curves for steel under sequential reverse loading at $\dot{\gamma} \sim 760 \text{ s}^{-1}$, for a constant strain amplitude $\gamma_0 \sim 0.262$

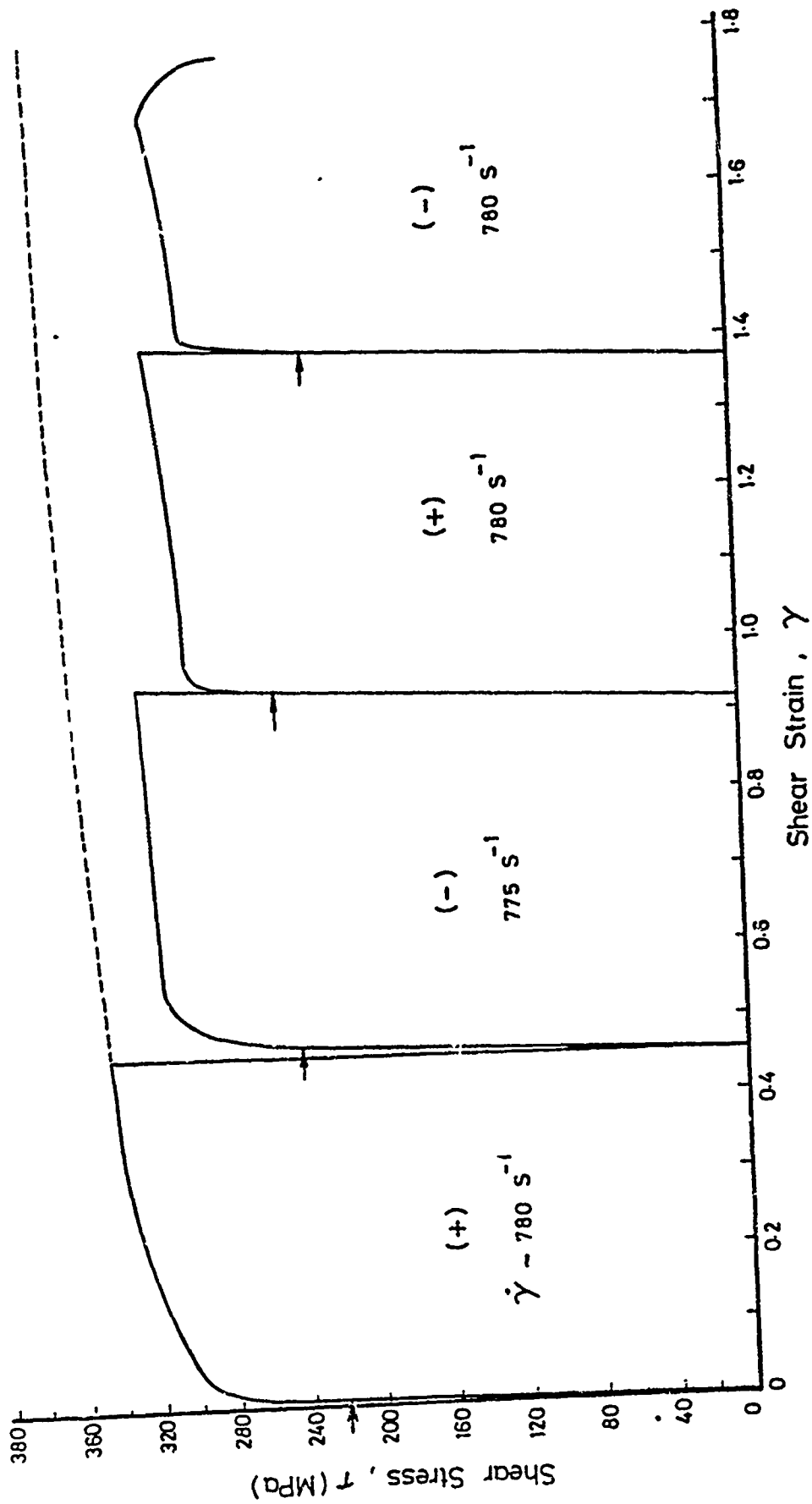


Fig. 23(b) Stress-strain curves for steel under sequential reverse loading at $\dot{\gamma} \sim 760 \text{ s}^{-1}$, for a constant strain amplitude $\gamma_0 \sim 0.46$

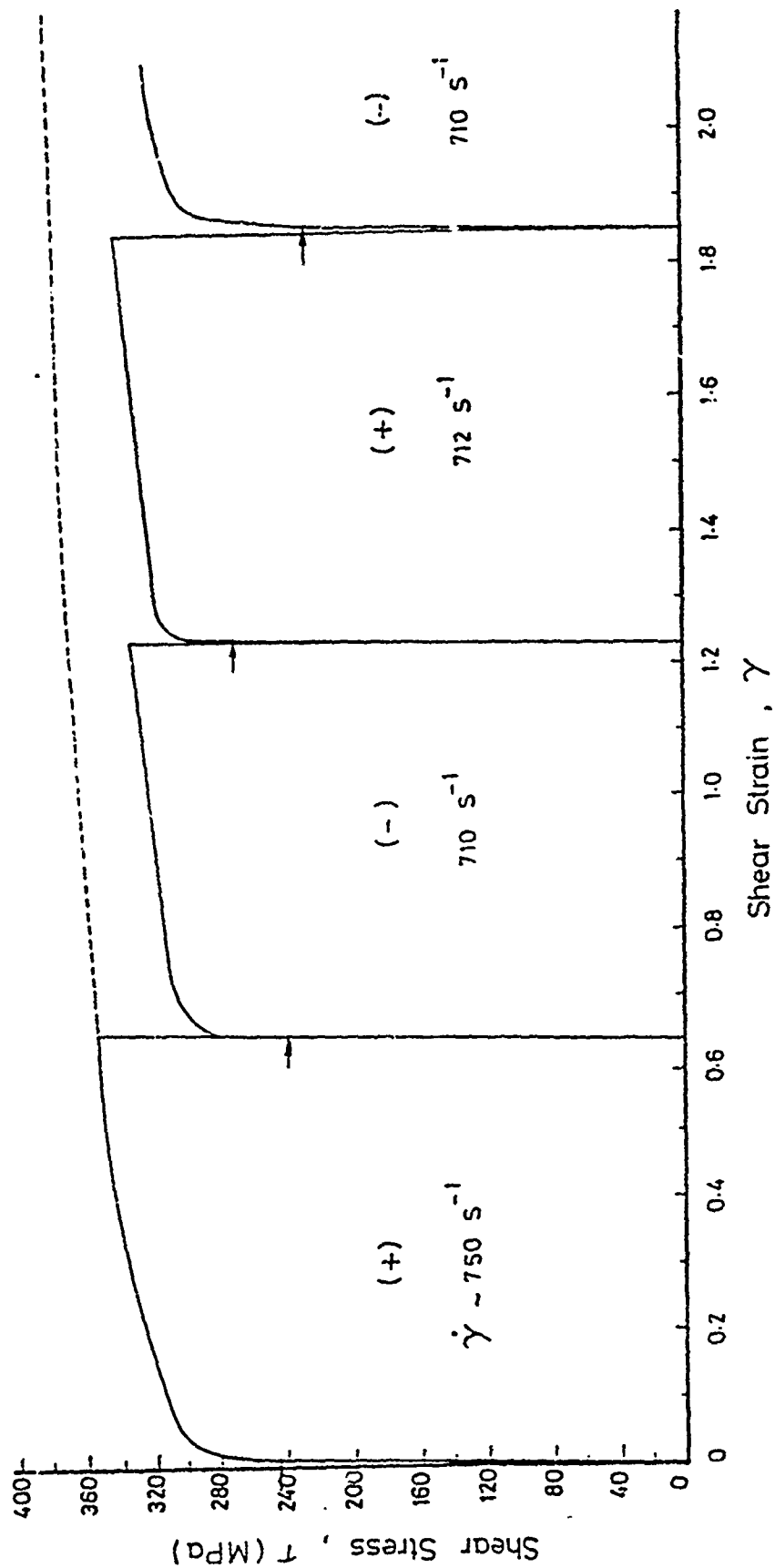


Fig. 23(c) Stress-strain curves for steel under sequential reverse loading at $\dot{\gamma} \sim 760 \text{ s}^{-1}$, for a constant strain amplitude $\gamma_0 \sim 0.65$

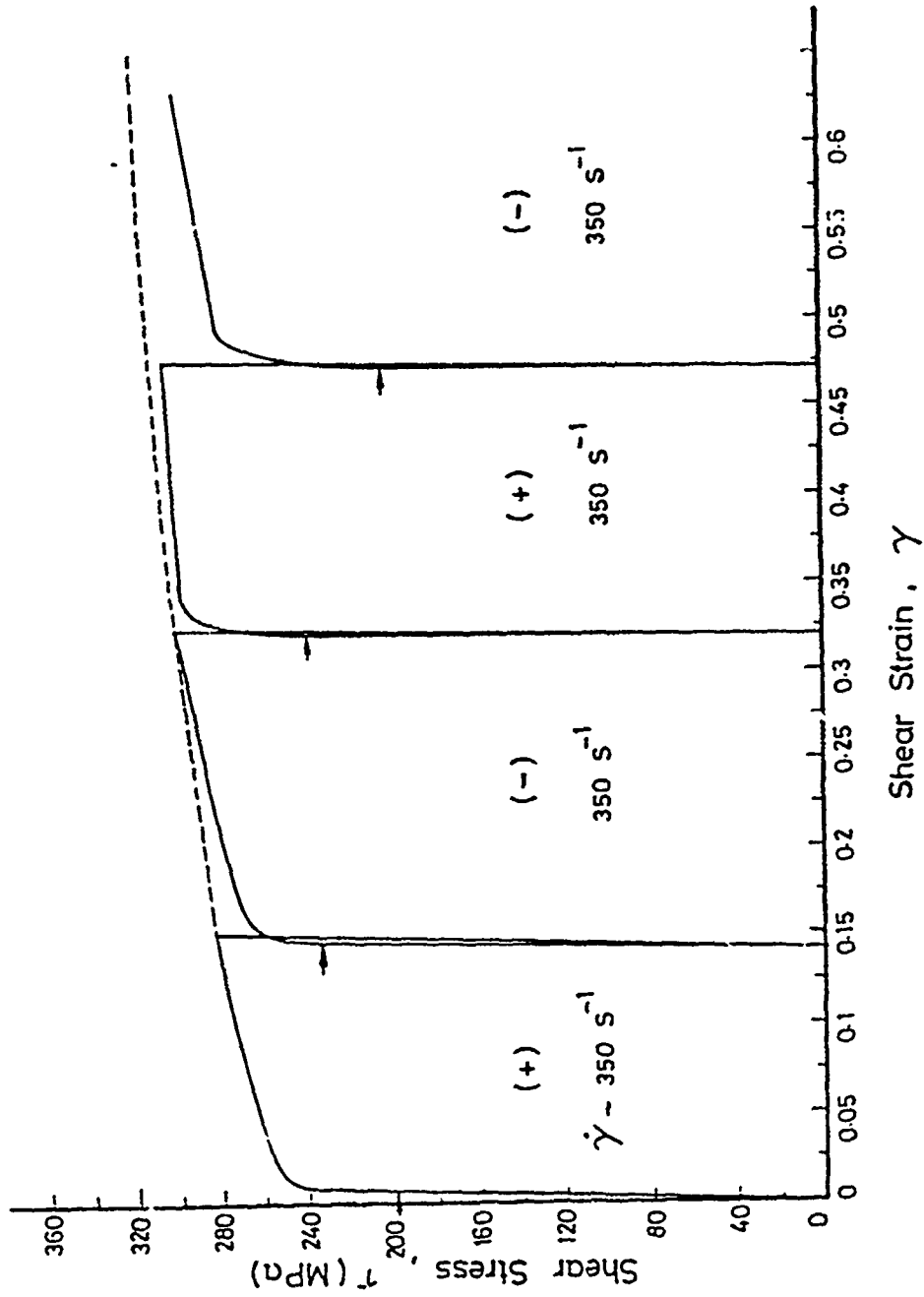


Fig. 24(a) Stress-strain curves for steel under sequential reverse loading at $\dot{\gamma} \sim 350 \text{ s}^{-1}$, constant strain amplitude $\gamma_0 \sim 0.15$

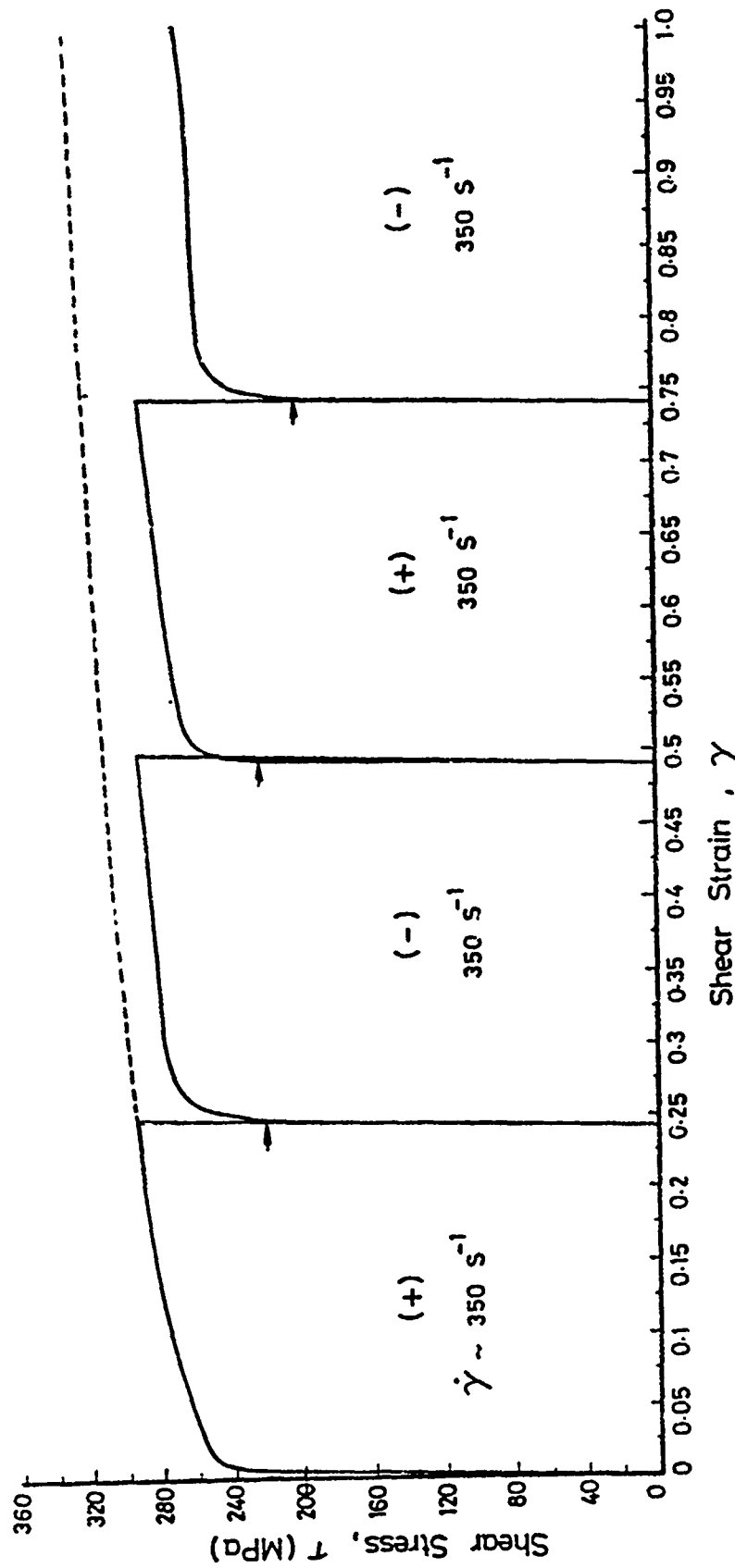


Fig. 24(b) Stress-strain curves for steel under sequential reverse loading at $\dot{\gamma} \sim 350 \text{ s}^{-1}$, for a constant strain amplitude $\gamma_0 \sim 0.25$

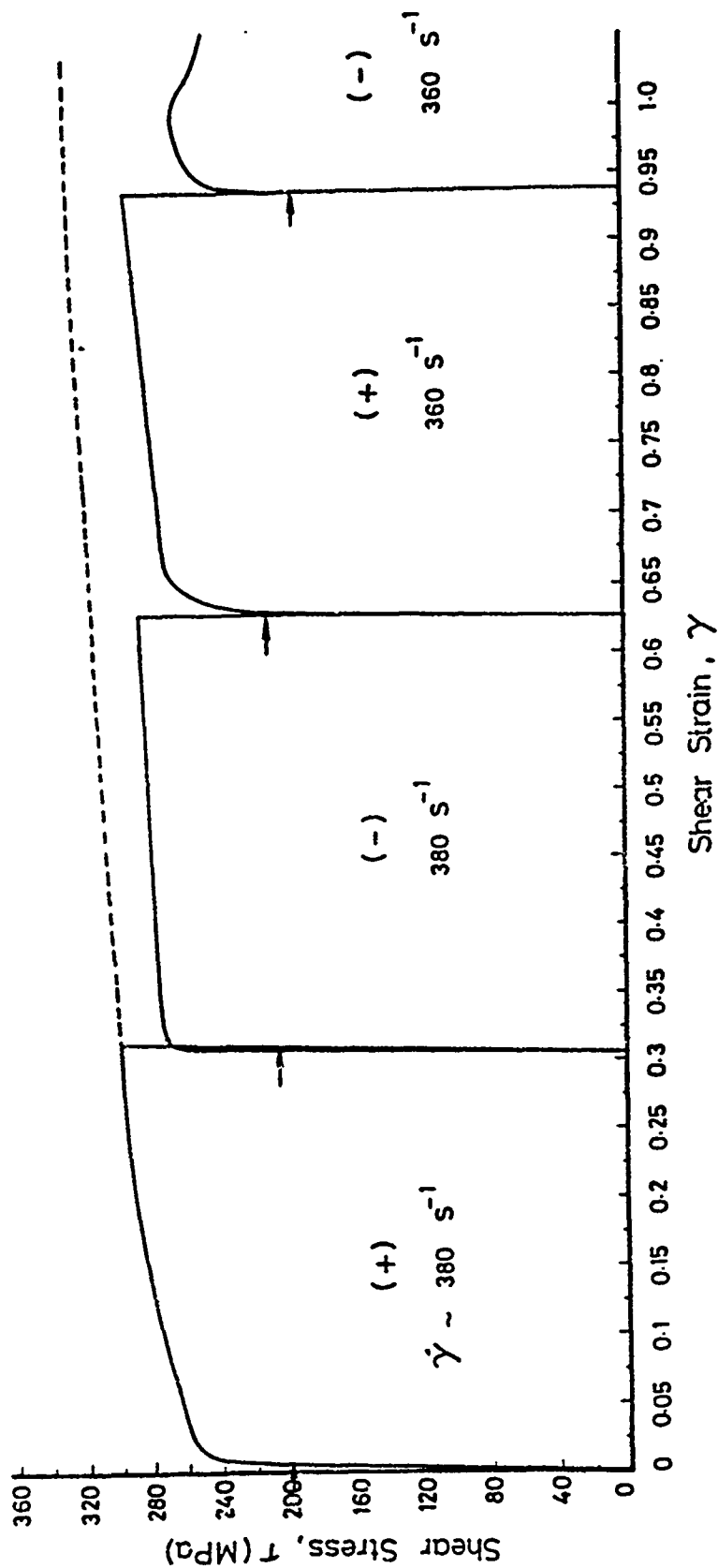


Fig. 24(c) Stress-strain curves for steel under sequential reverse loading at $\dot{\gamma} \sim 350 \text{ s}^{-1}$, for a constant strain amplitude $\gamma_0 \sim 0.312$

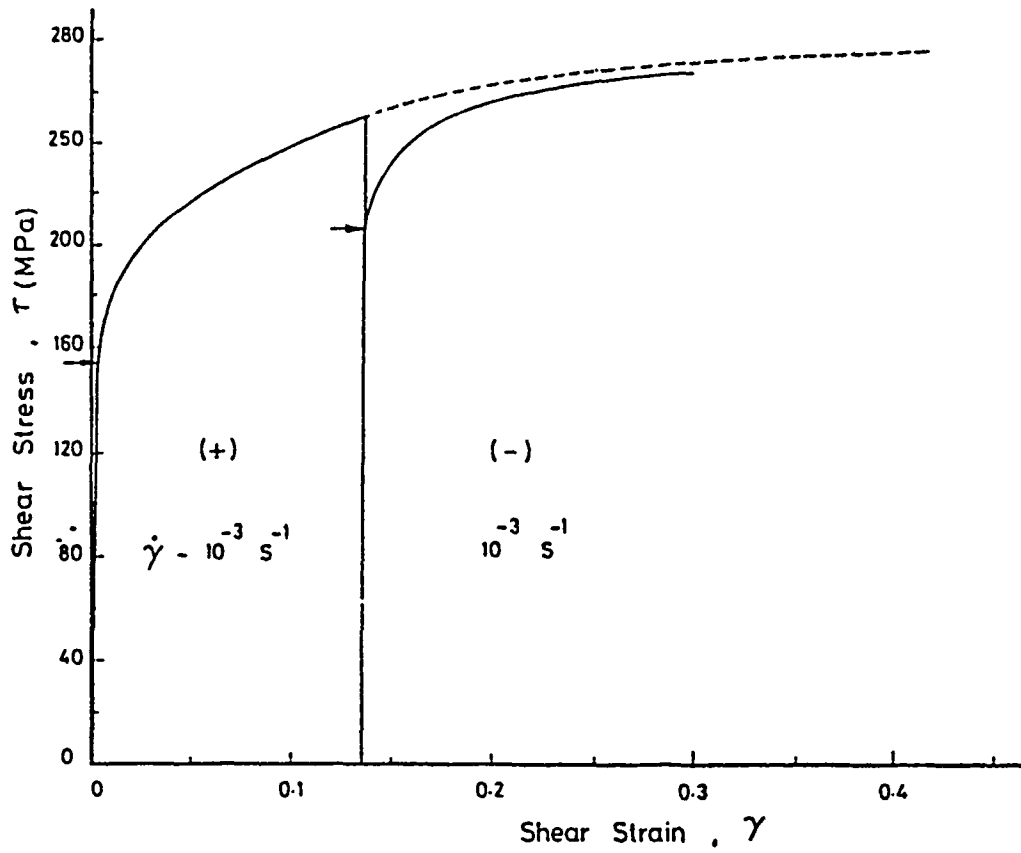


Fig. 25(a) Stress-strain curves for steel under forward and reverse loading at $\dot{\gamma} = 10^{-3} \text{ s}^{-1}$, for a constant strain amplitude $\gamma_0 = 0.135$

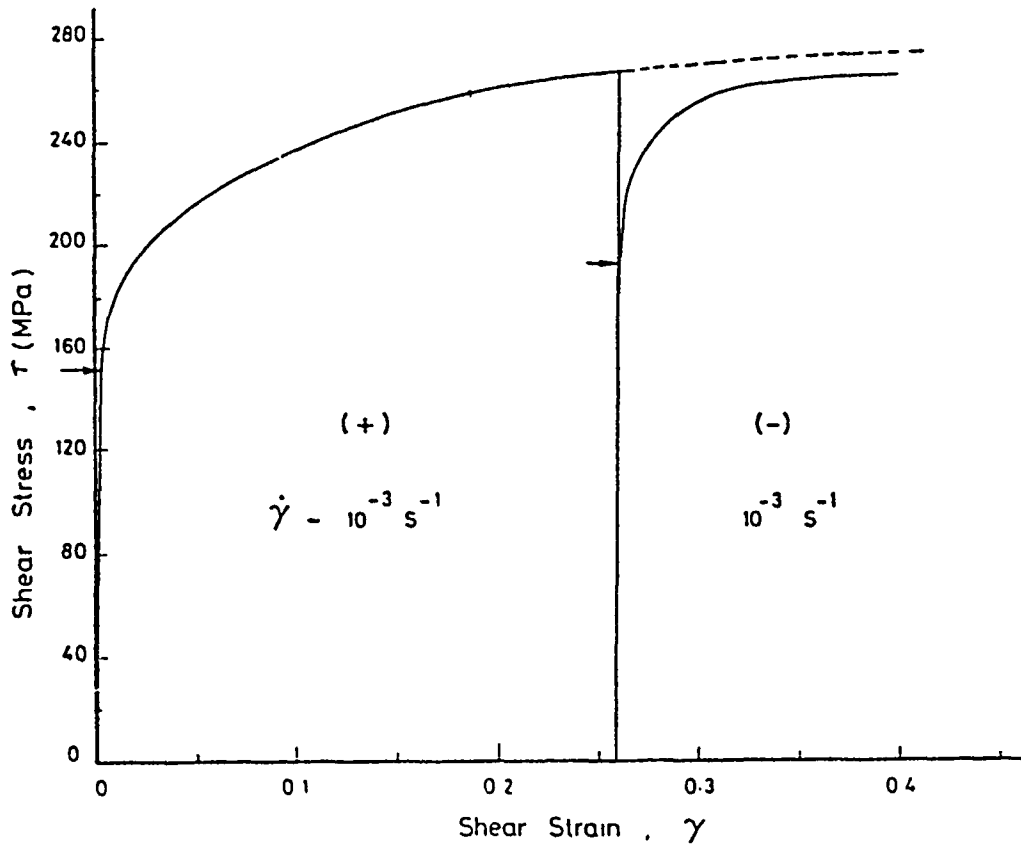


Fig. 25(b) Stress-strain curves for steel under forward and reverse loading at $\dot{\gamma} = 10^{-3} \text{ s}^{-1}$, for a constant strain amplitude $\gamma_0 = 0.26$

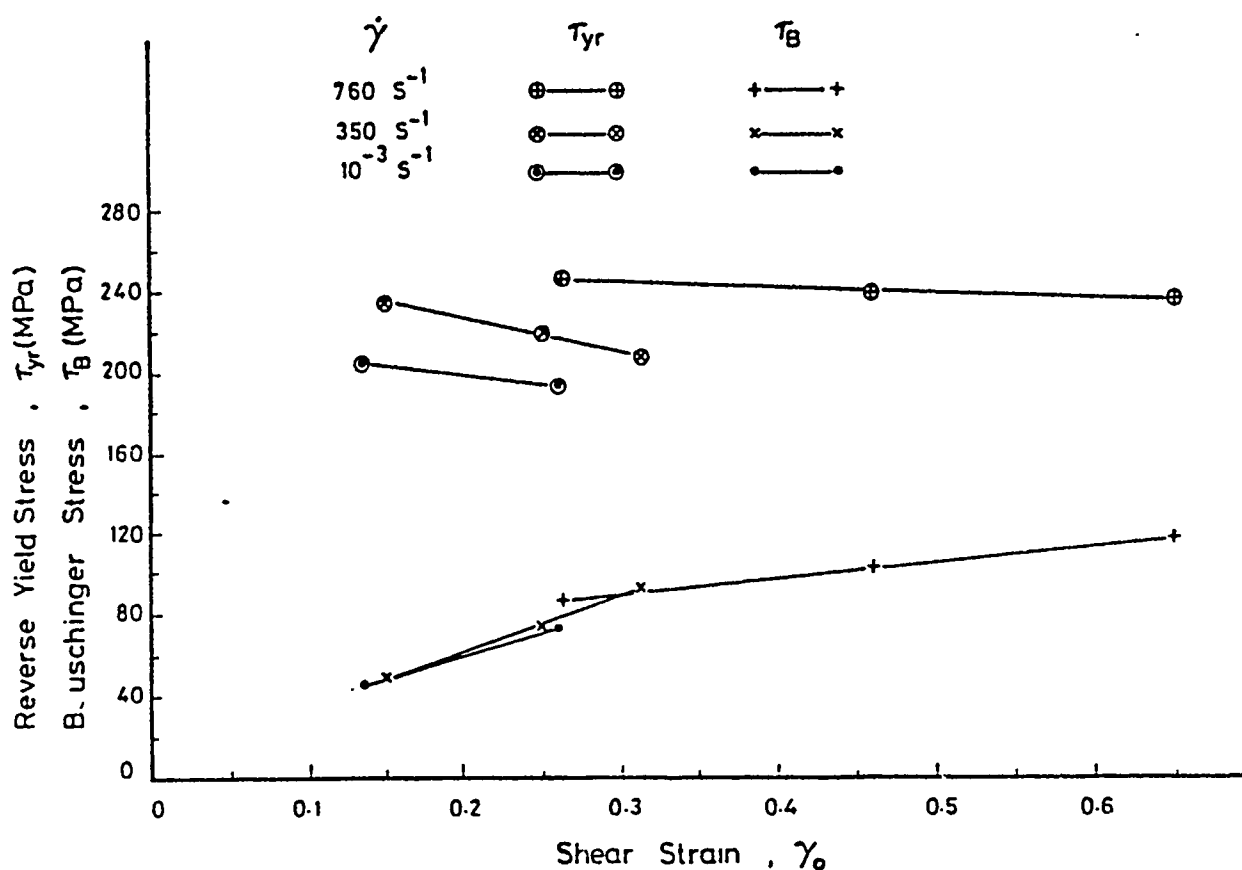


Fig. 26 Variation of reverse yield stress, τ_{yr} , and Bauschinger stress, τ_B , for steel, with strain amplitude, γ_0 , for various strain rates

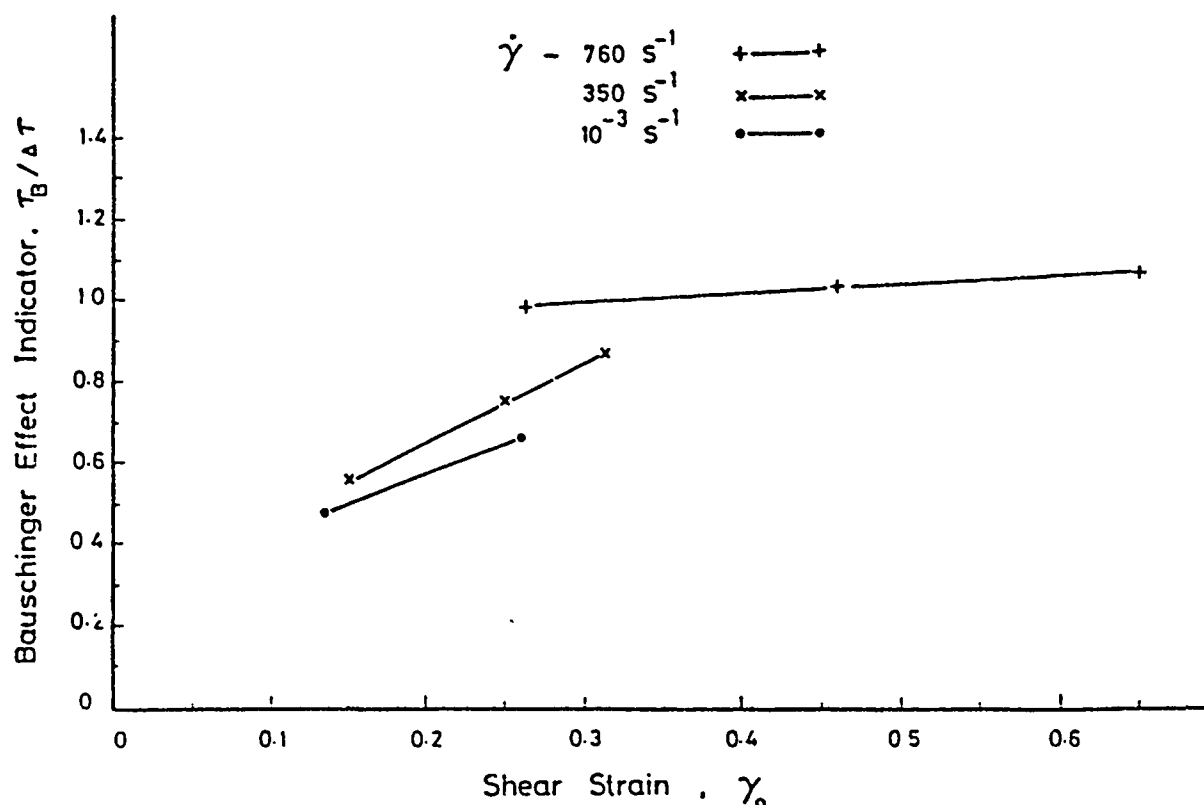


Fig. 27 Variation of Bauschinger effect indicator, $\tau_B / \Delta \tau$, for steel, with strain amplitude, γ_0 , for various strain rates

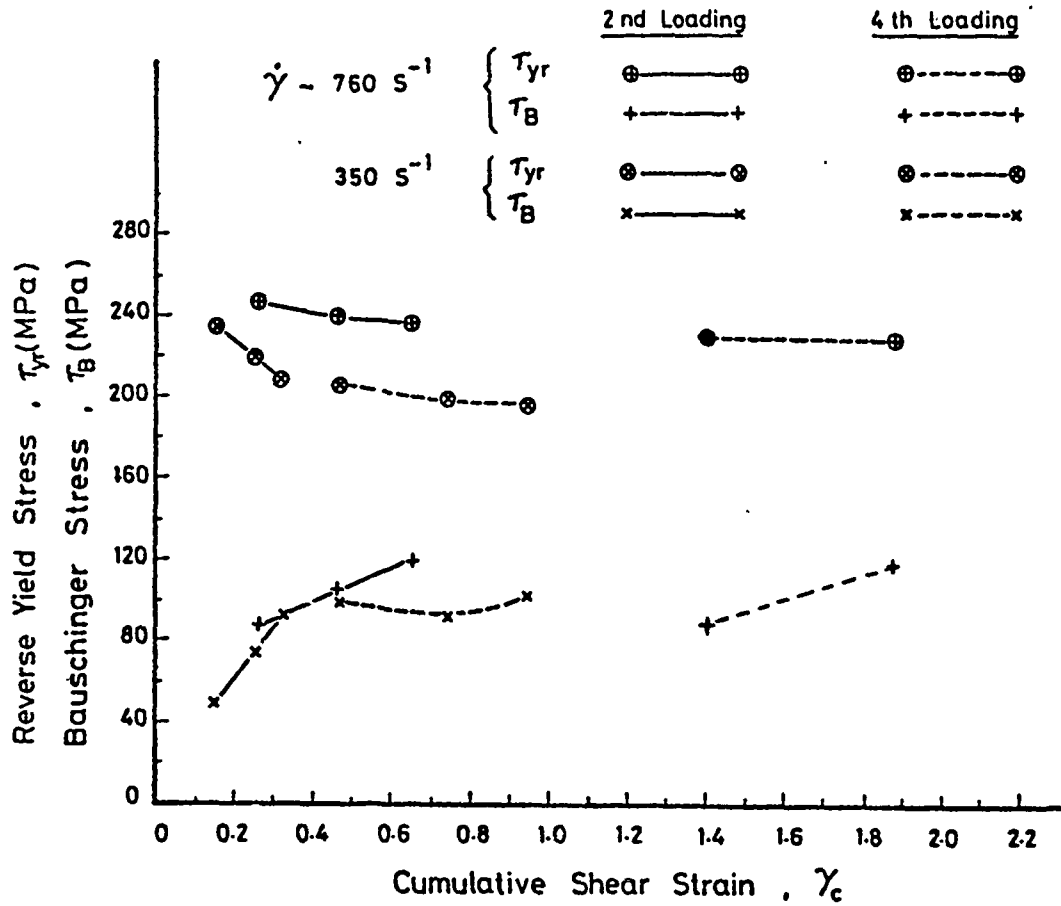


Fig. 28 Variation of reverse yield stress, τ_{yr} , and Bauschinger stress, τ_B , for steel, with cumulative strain, γ_c , for various strain rates

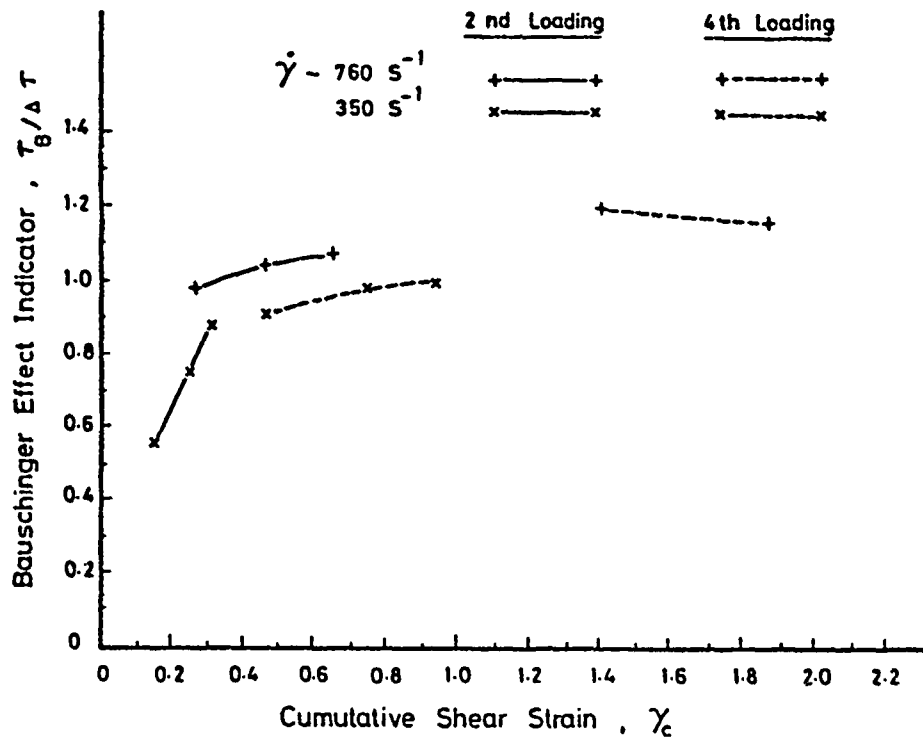


Fig. 29 Variation of Bauschinger effect indicator, $\tau_B / \Delta \tau$, for steel, with cumulative strain, γ_c , for various strain rates

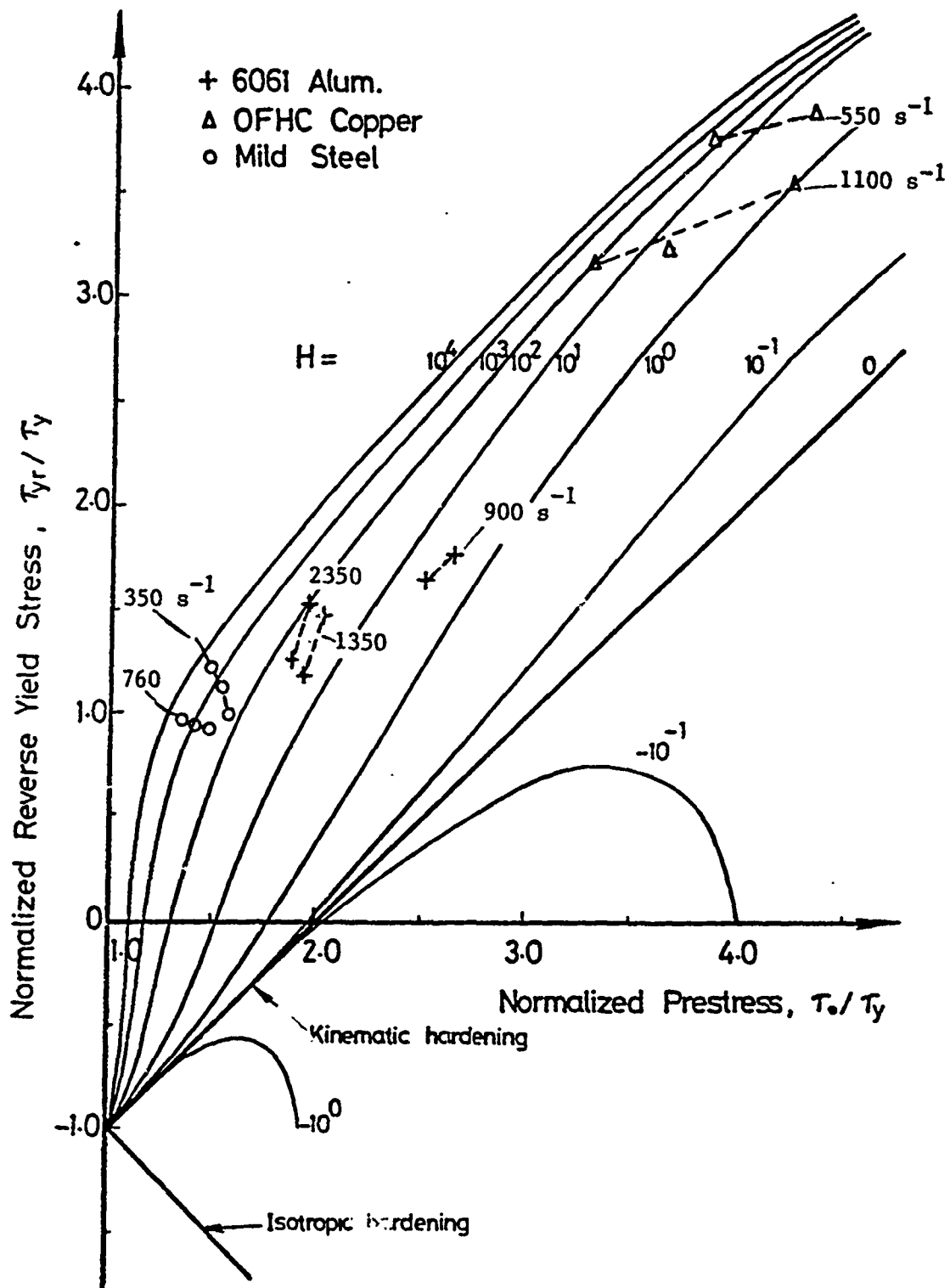


Fig. 30 Comparison between the measured Bauschinger effect and predictions from kinematic hardening theory

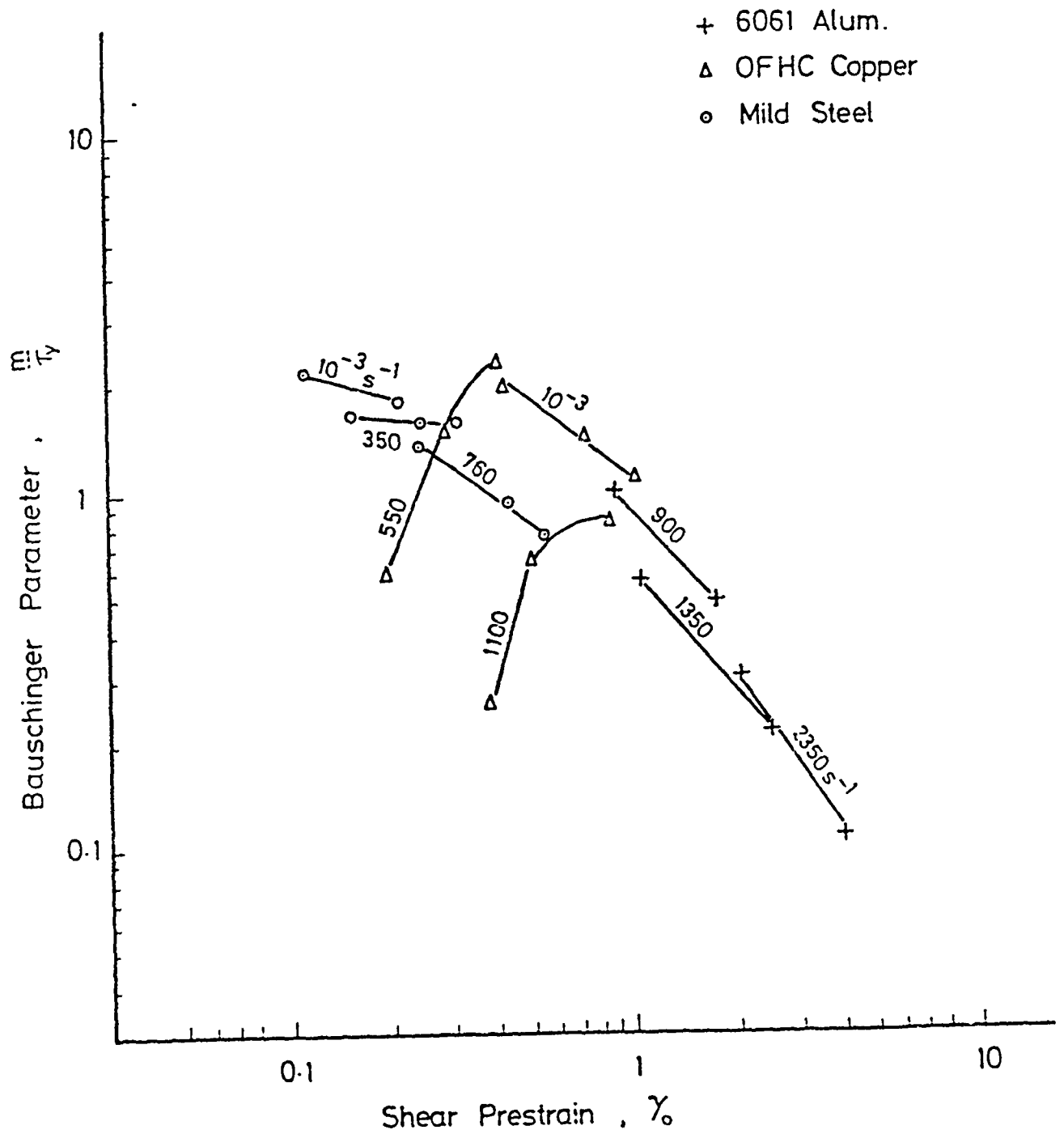


Fig. 31 Effect of prestrain amplitude on the Bauschinger parameter m/τ_y

PART II

Ratchetting of Pressurized Tubes
Subjected to Radial Cyclic Thermal Gradient

SECTION 1

INTRODUCTION

The structural ratchetting phenomenon (cumulative cyclic plastic strain growth), being of prime importance in modern systems where a steady and a cyclic load components are acting simultaneously, has been investigated within the frame of the present work. This phenomenon and its associated ratchet strains are greatly affected by the formulation of the structure, the flow and hardening characteristics of its material. If the cyclic load component is due to a cyclic thermal gradient, ratchet strains are also affected by the form of that gradient as well as its amplitude.

In the particular case of a steel tube subjected to steady internal pressure and cyclic radial thermal gradient, which simulates the conditions of fuel cans of liquid Metal Fast Breeder Reactors, ratchetting - among other deformational patterns - may occur under certain loading combinations/1/.

All previous analytical work on this problem was confined to Bree's uniaxial formulation of a tube made of an elastic - perfectly plastic or elastic - linearly plastic material with kinematic hardening assumptions. In the present phase, an effort was made to provide a more faithful biaxial formulation of the tube problem and to develop a new numerical procedure capable of handling any tube dimensions, different temperature distributions, and various hardening models. This new formulation has been presented in a previous report/2/, and will only be summarized hereafter. More emphasis will be made however, on the numerical procedure developed for its implementation and on the results obtained as contrasted with those of the uniaxial model and those obtained from experiments.

SECTION 2

BIAXIAL FORMULATION OF THE TUBE PROBLEM

The elasto-plastic investigations to determine stresses, strains and modes of deformations for tubes subjected to both steady internal pressure and cyclic radial temperature gradient as previously done by Miller/3/, Bree /4/, Mulcahy /5/ and others were confined to thin-walled tubes for which an equivalent uniaxial model was suggested. The hoop stress was maintained, the thermal stress was magnified by a factor equal to $\frac{1}{(1-\nu)}$ and the axial stress was neglected. The arguments made by Bree showed that such an equivalent uniaxial model - for the originally two dimensional problem - would lead to more conservative results, since the effect of the axial stress - which was neglected - is opposing that of the hoop stress and therefore the results obtained were expected to be greater than what would be obtained by an exact solution.

The actual elasto-plastic solution, being in two dimensions, is analytically impossible. Therefore, from experience earned from numerical investigations of the uniaxial formulation of the tube problem /1/ it is realized that a similar procedure could be followed to determine the elasto-plastic response of thick tubes under generalized plane strain conditions. In this case, the radial stress σ_r is no longer neglected, the axial stress σ_z is not set to zero, the thermal stress σ_t is not magnified and the axial strain ϵ_z is assumed to be constant.

A complete numerical procedure is developed and presented in this work for the generalized plane strain tube problem. Different hardening rules for the tube material can be employed in this numerical procedure. Both the kinematic and isotropic hardening models showed satisfactory performance as related to the tube problem.

2.1 Generalized plane strain formulation

Consider a thick-walled cylinder with inner radius a , outer radius b subjected to steady internal pressure p and a cyclic temperature gradient $T(r)$. The tube has closed ends and is further subjected to an additional uniform axial stress σ_0 . Generalized plane strain assumptions imply that the axial strain ϵ_z is independent of radius r , i.e. $\epsilon_z = \text{constant}$. Total strain is composed from elastic, plastic and thermal components. Creep

As shown in detail elsewhere /2/, equilibrium, compatibility and stress-strain relations can be used to derive the following expressions for the stress components:

$$\begin{aligned}\sigma_r &= -p \cdot \frac{a^2}{r^2} \cdot \frac{b^2 - r^2}{b^2 - a^2} + \frac{E}{(1+\nu)(1-2\nu)} \left[I_1 + I_2 + I_3 - \frac{b^2}{r^2} \cdot \frac{r^2 - a^2}{b^2 - a^2} I_0 \right], \\ \sigma_\theta &= p \cdot \frac{a^2}{r^2} \cdot \frac{b^2 + r^2}{b^2 - a^2} + \frac{E}{(1+\nu)(1-2\nu)} \left[I_1 - I_2 - I_3 - \frac{b^2}{r^2} \cdot \frac{r^2 + a^2}{b^2 - a^2} I_0 \right] \\ &\quad - \frac{E}{1-\nu^2} \left[\epsilon_\theta^p - \nu(\epsilon_r^p + \epsilon_\theta^p) + \alpha(1+\nu)T \right], \quad (1)\end{aligned}$$

$$\begin{aligned}\sigma_z &= 2\nu p \frac{a^2}{b^2 - a^2} + \frac{2\nu E}{(1+\nu)(1-2\nu)} \left[I_1 - \frac{b^2}{b^2 - a^2} I_0 \right] - \frac{E}{1-\nu^2} \left[\epsilon_\theta^p - \nu(\epsilon_r^p + \epsilon_\theta^p) \right] \\ &\quad + E\epsilon_z - \frac{E\alpha T}{1-\nu}\end{aligned}$$

and strain components:

$$\begin{aligned}\epsilon_r &= \frac{(1+\nu)(1-2\nu)}{E(b^2 - a^2)} p a^2 \left[1 - \frac{b^2}{r^2} \frac{1}{1-2\nu} \right] + I_1 + \frac{I_2 + I_3}{1-2\nu} - \frac{b^2 I_0}{b^2 - a^2} \\ &\quad \cdot \left[1 - \frac{a^2}{r^2} \frac{1}{1-2\nu} \right] - \nu\epsilon_z + \frac{1}{1-\nu} \left[(1-2\nu) \epsilon_r^p + \alpha(1+\nu)T \right], \\ \epsilon_\theta &= \frac{(1+\nu)(1-2\nu)}{E(b^2 - a^2)} p a^2 \left[1 + \frac{b^2}{r^2} \frac{1}{1-2\nu} \right] + I_1 - \frac{I_2 + I_3}{1-2\nu} - \frac{b^2 I_0}{b^2 - a^2} \\ &\quad \cdot \left[1 + \frac{a^2}{r^2} \frac{1}{1-2\nu} \right] - \nu\epsilon_z.\end{aligned} \quad (2)$$

where

$$\begin{aligned}
 I_1 &= \frac{1-2\nu}{2(1-\nu)} \int_a^r \frac{\epsilon_r^p - \epsilon_\theta^p}{r} dr, \\
 I_2 &= \frac{(1-2\nu)^2}{2(1-\nu)r^2} \int_a^r r (\epsilon_r^p + \epsilon_\theta^p) dr, \\
 I_3 &= \frac{-\alpha(1-2\nu)(1+\nu)}{(1-\nu)r^2} \int_a^r T r dr \text{ and} \\
 I_0 &= [I_1 + I_2 + I_3]_{r=b}
 \end{aligned} \tag{3}$$

Note that the value of ϵ_z is an unknown constant yet to be determined. This constant value of ϵ_z is determined from the condition of axial equilibrium, as:

$$\begin{aligned}
 \epsilon_z &= \frac{\sigma_0}{E} + (1-2\nu) \frac{p a^2}{(b^2 - a^2)E} + \frac{2\nu}{(1+\nu)(1-2\nu)(b^2 - a^2)} [b^2 I_0 - 2 \int_a^b r I_1 dr] \\
 &- \frac{2}{(1-\nu^2)(b^2 - a^2)} [(1-\nu) \int_a^b r \epsilon_\theta^p dr + \int_a^b r \epsilon_r^p dr - \alpha(1+\nu) \int_a^b r T dr]
 \end{aligned} \tag{4}$$

In the above formulation, the uniform axial stress σ_0 can be set to any value and hence this feature allows investigating plane strain conditions ($\epsilon_z = 0$) since the corresponding value of σ_0 can be determined from Eq. (4)

2.2 Plasticity relations

Since the tube is subjected to cyclic thermal gradient, the material model to be used in the analysis should exhibit the characteristics of metals when subjected to cyclic stresses. The most important of these characteristics for initially annealed metals and alloys are cyclic

hardening, cyclic creep and cyclic relaxation. As a first step toward the modelling of these features of material behaviour, the tube is analysed here using classical plasticity theories with both the kinematic and isotropic hardening rules.

2.2.1 Kinematic hardening

The plasticity relations for kinematic hardening can be formulated as follows. The yield condition for axisymmetric states of stress is given by:

$$F = (S_r - \alpha_r)^2 + (S_\theta - \alpha_\theta)^2 + (S_z - \alpha_z)^2 - \frac{2}{3} \sigma_{y,0}^2 = 0 \quad (5a)$$

where S_r , S_θ and S_z are the stress deviators, given by

$$S_r = \sigma_r - (\sigma_r + \sigma_\theta + \sigma_z) / 3, \quad (5b)$$

$$S_\theta = \sigma_\theta - (\sigma_r + \sigma_\theta + \sigma_z) / 3,$$

$$S_z = \sigma_z - (\sigma_r + \sigma_\theta + \sigma_z) / 3,$$

and α_r , α_θ , α_z are the coordinates of the center of the yield surface in stress space. The initial yield stress is denoted by $\sigma_{y,0}$. The flow rule - which relates plastic strain increments to stresses - is based upon Drucker postulate which states that the plastic strain rate vector is normal to the yield surface, so that :

$$d\epsilon_r^p = d\lambda \cdot \frac{\partial F}{\partial \sigma_r} = \frac{2}{3} d\lambda \cdot (S_r - \alpha_r), \quad (6)$$

$$d\epsilon_\theta^p = d\lambda \cdot \frac{\partial F}{\partial \sigma_\theta} = \frac{2}{3} d\lambda \cdot (S_\theta - \alpha_\theta),$$

$$d\epsilon_z^p = d\lambda \cdot \frac{\partial F}{\partial \sigma_z} = \frac{2}{3} d\lambda \cdot (S_z - \alpha_z),$$

where $d\lambda$ is a positive scalar multiplier yet to be determined. Introducing an effective plastic strain increment $d\bar{\epsilon}^p$ which is defined as :

$$d\bar{\epsilon}^p = \left[\frac{2}{3} (d\epsilon_r^p \cdot d\epsilon_r^p + d\epsilon_\theta^p \cdot d\epsilon_\theta^p + d\epsilon_z^p \cdot d\epsilon_z^p) \right]^{1/2} \quad (7)$$

which reduces $d\bar{\epsilon}^P$ to the observed plastic strain in the uniaxial test and substitution of Eq. (6) in Eq. (7) yields the value of $d\lambda$ as $(\frac{3}{2})^2 \frac{d\bar{\epsilon}^P}{\sigma}$. Hence, the flow relations can be rewritten as:

$$\begin{aligned} d\epsilon_r^P &= \frac{3}{2} \cdot \frac{d\bar{\epsilon}^P}{\sigma} [S_r - \alpha_r] , \\ d\epsilon_\theta^P &= \frac{3}{2} \cdot \frac{d\bar{\epsilon}^P}{\sigma} [S_\theta - \alpha_\theta] , \\ d\epsilon_z^P &= \frac{3}{2} \cdot \frac{d\bar{\epsilon}^P}{\sigma} [S_z - \alpha_z] \end{aligned} \quad (8)$$

The hardening rule which describes the incremental translation of the center of the yield surface is based upon Prager kinematic hardening model which assumes that such translations are in the direction of the plastic strain increments. Thus:

$$d\alpha_r = du \cdot d\epsilon_r^P ; \quad d\alpha_\theta = du \cdot d\epsilon_\theta^P ; \quad d\alpha_z = du \cdot d\epsilon_z^P , \quad (9)$$

where du is a positive scalar multiplier. Introducing an effective incremental translation $d\bar{\alpha}$ of the center of the yield surface as

$$d\bar{\alpha} = \left[\frac{3}{2} \cdot (d\alpha_r \cdot d\alpha_r + d\alpha_\theta \cdot d\alpha_\theta + d\alpha_z \cdot d\alpha_z) \right]^{\frac{1}{2}} \quad (10)$$

reduces $d\bar{\alpha}$ to the observed incremental translation of the center of the yield surface in the uniaxial test. Substitution of Eq. (9) into Eq. (10) yields $du = \frac{d\bar{\alpha}}{d\bar{\epsilon}^P}$ which in turn gives $d\alpha_r$, $d\alpha_\theta$ and $d\alpha_z$, as

$$\begin{aligned} d\alpha_r &= \frac{2}{3} \cdot \frac{d\bar{\alpha}}{d\bar{\epsilon}^P} \cdot d\epsilon_r^P = \frac{2}{3} C \cdot d\epsilon_r^P , \\ d\alpha_\theta &= \frac{2}{3} \cdot \frac{d\bar{\alpha}}{d\bar{\epsilon}^P} \cdot d\epsilon_\theta^P = \frac{2}{3} C \cdot d\epsilon_\theta^P , \\ d\alpha_z &= \frac{2}{3} \cdot \frac{d\bar{\alpha}}{d\bar{\epsilon}^P} \cdot d\epsilon_z^P = \frac{2}{3} C \cdot d\epsilon_z^P , \end{aligned} \quad (11)$$

where $C = \frac{d\bar{\alpha}}{d\bar{\epsilon}^p}$ is the coefficient of strain hardening as determined from the basic uniaxial test.

The yield condition, Eq. (5), the flow rule, Eq. (8), and the hardening rule, Eq. (11), completely define the plasticity theory for kinematic hardening. In the present work, the coefficient of strain hardening C is taken as a constant which implies that linear hardening is assumed.

2.2.2 Isotropic hardening

If the isotropic hardening is considered, the yield condition, Eq. (5), becomes

$$F = S_r^2 + S_\theta^2 + S_z^2 - \frac{2}{3} \sigma_y^2 = 0 \quad (12)$$

where, in this case, σ_y is the current value of the yield stress which is equal to the last value of the equivalent stress $\bar{\sigma}$ at which plasticity has occurred. The initial value for σ_y is the initial yield stress $\sigma_{y,0}$.

The flow rule of Eq. (8) becomes

$$d\epsilon_r^p = \frac{3}{2} \frac{d\bar{\epsilon}^p}{\bar{\sigma}} S_r \quad ; \quad d\epsilon_\theta^p = \frac{3}{2} \frac{d\bar{\epsilon}^p}{\bar{\sigma}} S_\theta \quad ; \quad d\epsilon_z^p = \frac{3}{2} \frac{d\bar{\epsilon}^p}{\bar{\sigma}} S_z \quad (13)$$

The hardening rule in the case of isotropic hardening is simple, since no translation of the center of the yield surface occurs, i.e. $\alpha_r = \alpha_\theta = \alpha_z = 0$, and the current value of the yield stress is set equal to the value of the equivalent stress $\bar{\alpha}$ at which plasticity has occurred for the last time.

The yield condition, the flow rule and the hardening rule are employed in the numerical procedure for either of the kinematic and isotropic material models and the solution for stresses and strains is then found at any point in the tube during any given cycle.

SECTION 3

NUMERICAL PROCEDURE

Cyclic thermo-elasto-plastic problems may be solved by means of the method of successive elastic solutions in which the total thermal gradient is applied incrementally. For each increment, an iterative procedure is employed in order to determine the plastic strain rate vector $(d\epsilon_r^p, d\epsilon_\theta^p, d\epsilon_z^p)$ for the biaxial tube model which satisfies the equilibrium, compatibility and stress-strain relations. Then, this plastic strain rate vector is used to determine the corresponding stresses.

The procedure used for the uniaxial tube model is basically the same as that used for the biaxial tube model. Therefore, the numerical procedure for the uniaxial case (being a special case of the biaxial model) is not given here and, instead, that for the biaxial problem is presented in full.

As mentioned earlier, the linear temperature distribution is only a special case of the bilinear distribution. Assigning zero to the value of 'h' in Fig. 1 will convert the bilinear temperature distribution into a linear distribution. Hence the proper value of 'h' within the following numerical procedures will provide the different versions for the different temperature distributions.

The procedure may be divided into two main segments; (a) determination of the temperature level at which first yield occurs, and (b) continuation of thermal load incrementation to determine the elasto-plastic solution of the problem.

3.1 Determination of the Temperature Level at Which First Yield Occurs

For the general case in which a bilinear temperature distribution is considered across the tube wall, the temperature may be given by

$$T(x) = 0 \quad 0 \leq x \leq h \quad (14)$$

$$T(x) = -T(x-h) / (1-h) \quad h \leq x \leq 1$$

where $x = (r_0 - r)/t$.

The temperature changes proportionally at all radii such that, for an intermediate temperature as shown by a dotted line in Fig. 1, ΔT is replaced by $\Delta T'$. For the full temperature distribution the temperature difference is ΔT .

In order to determine the temperature level at which first yield occurs, the total temperature gradient ΔT should be divided into an appropriate number of small increments. Care should be given in choosing the number of load increments to assure convergence of the iterations and to save computer time. According to Barsoum /6/, and also from numerical experiences, it was found that relatively large load increments would cause divergence. The reason behind this divergence is that the corrected plastic strains are calculated through stresses which are in turn erroneous during the iteration process.

The thermal load is now applied incrementally and the thermo-elasto-plastic problem is solved with the initial values of plastic strains $\epsilon_r^P = \epsilon_\theta^P = \epsilon_z^P = 0$ (or $d\epsilon^P = 0$ for the uniaxial model). After each temperature increment, a check is made on the yield function $F(r)$ at different points covering the thickness from the inner to the outer radius. If $F(r) < 0$, no yield has started yet. If $F(r) \geq 0$, yield has occurred; consequently, the iterative procedure for evaluating the plastic strains is to be started, and the thermal load incrementation is continued until full temperature difference, ΔT , is covered.

3.2 Continuation of Thermal Load Incrementation to Determine the Elastic Plastic Solution

For the evaluation of correct stresses and strains, the procedure used consisted of the following steps.

- (i) For all radii at which plastic deformation is likely to occur, initial values for the increments of plastic strains are assumed such that $\Delta\epsilon_r^P + \Delta\epsilon_\theta^P + \Delta\epsilon_z^P = 0$. An appropriate starting assumption is to take these increments very small, as for instance

$$\Delta\epsilon_r^P = 1.5 \times 10^{-6}, \quad \Delta\epsilon_\theta^P = -1 \times 10^{-6}, \quad \Delta\epsilon_z^P = -0.5 \times 10^{-6} \quad (15)$$

It should be noted that $\Delta\epsilon_r^P$, $\Delta\epsilon_\theta^P$ and $\Delta\epsilon_z^P$ are taken as zeros at all other radii at which no yield occurs.

- (2) At every radius, the effective increment of plastic strain, $\Delta\epsilon^P$, is calculated as

$$\Delta\epsilon^P = \left[\frac{2}{3} (\Delta\epsilon_r^{P^2} + \Delta\epsilon_\theta^{P^2} + \Delta\epsilon_z^{P^2}) \right]^{\frac{1}{2}} \quad (7) \text{ bis}$$

- (3) At every radius, the change in the coordinates of the center of the yield surface is calculated as

$$\Delta\alpha_r = \frac{2}{3} C \cdot \Delta\epsilon_r^P; \quad \Delta\alpha_\theta = \frac{2}{3} C \cdot \Delta\epsilon_\theta^P; \quad \Delta\alpha_z = \frac{2}{3} C \cdot \Delta\epsilon_z^P, \quad (11) \text{ bis}$$

where C is the work-hardening parameter taken as $\frac{\beta E}{1-\beta}$

- (4) At all radii, the new values of plastic strains are calculated as

$$\begin{aligned} \epsilon_{r,n}^P &= \epsilon_{r,n-1}^P + \Delta\epsilon_r^P, \\ \epsilon_{\theta,n}^P &= \epsilon_{\theta,n-1}^P + \Delta\epsilon_\theta^P, \\ \epsilon_{z,n}^P &= \epsilon_{z,n-1}^P + \Delta\epsilon_z^P, \end{aligned} \quad (16)$$

where $n-1$ and n denote a previous and current increment of thermal loading.

- (5) At all radii, the new values of the coordinates of the center of the yield surface are calculated as

$$\begin{aligned} \alpha_{r,n} &= \alpha_{r,n-1} + \Delta\alpha_r, \\ \alpha_{\theta,n} &= \alpha_{\theta,n-1} + \Delta\alpha_\theta, \\ \alpha_{z,n} &= \alpha_{z,n-1} + \Delta\alpha_z \end{aligned} \quad (17)$$

- (6) Using $\epsilon_{r,n}^P$, $\epsilon_{\theta,n}^P$ and $\epsilon_{z,n}^P$ obtained in step 4, the elasto-plastic-thermal problem is solved using Eqs. (1), (2) and (4) to calculate the current stresses and strains: $\sigma_{r,n}$, $\sigma_{\theta,n}$, $\sigma_{z,n}$, $\epsilon_{r,n}$, $\epsilon_{\theta,n}$ and $\epsilon_{z,n}$. At this level of calculations, it should be noted that the integrals I_2 and I_3 will have values other than zero.

- (7) At all radii, the deviatoric stress tensors are calculated as :

$$\begin{aligned} S_{r,n} &= \frac{2}{3} \left[\sigma_{r,n} - \frac{\sigma_{\theta,n} + \sigma_{z,n}}{2} \right], \\ S_{\theta,n} &= \frac{2}{3} \left[\sigma_{\theta,n} - \frac{\sigma_{r,n} + \sigma_{z,n}}{2} \right], \\ S_{z,n} &= \frac{2}{3} \left[\sigma_{z,n} - \frac{\sigma_{\theta,n} + \sigma_{r,n}}{2} \right] \end{aligned} \quad (5b) \text{ bis}$$

- (8) Using the values of $\alpha_{r,n}$, $\alpha_{\theta,n}$ and $\alpha_{z,n}$ obtained in step '5' together with $S_{r,n}$, $S_{\theta,n}$ and $S_{z,n}$ obtained in step '7', the corrected values of plastic strain increments $\Delta \epsilon^{p*}$, $\Delta \epsilon_{\theta}^{p*}$ and $\Delta \epsilon_z^{p*}$ are as follows /6/ :

$$\Delta \epsilon_r^{p*} = \frac{\Delta \bar{\epsilon}^p}{\epsilon_e} \cdot \epsilon_{r1}; \quad \Delta \epsilon_{\theta}^{p*} = \frac{\Delta \bar{\epsilon}^p}{\epsilon_e} \cdot \epsilon_{\theta1}; \quad \Delta \epsilon_z^{p*} = \frac{\Delta \bar{\epsilon}^p}{\epsilon_e} \cdot \epsilon_{z1} \quad (18)$$

where ϵ_e is an equivalent modified total strain calculated as

$$\epsilon_e = \left[\frac{2}{3} (\epsilon_{r1}^2 + \epsilon_{\theta1}^2 + \epsilon_{z1}^2) \right]^{\frac{1}{2}} \quad (19)$$

and $\Delta \bar{\epsilon}^p$ in this case is calculated from

$$\Delta \bar{\epsilon}^p = \epsilon_e - \frac{2}{3} \cdot \frac{1+\nu}{E} \sigma_{y,0} \quad (20)$$

where $\sigma_{y,0}$ is the initial yield stress, while ϵ_{r1} , $\epsilon_{\theta1}$ and ϵ_{z1} are the deviatoric modified strains to be calculated from

$$\begin{aligned} \epsilon_{r1} &= \frac{1+\nu}{E} [S_{r,n} - \alpha_{r,n}] + \Delta \epsilon_r^p, \\ \epsilon_{\theta1} &= \frac{1+\nu}{E} [S_{\theta,n} - \alpha_{\theta,n}] + \Delta \epsilon_{\theta}^p, \\ \epsilon_{z1} &= \frac{1+\nu}{E} [S_{z,n} - \alpha_{z,n}] + \Delta \epsilon_z^p \end{aligned} \quad (21)$$

- (9) The corrected value of effective plastic strain increment is calculated at all radii using the new values of plastic strain increments obtained in step '8'

$$\Delta \epsilon^{P*} = \left[\frac{2}{3} \{ (\Delta \epsilon_r^{P*})^2 + (\Delta \epsilon_\theta^{P*})^2 + (\Delta \epsilon_z^{P*})^2 \} \right]^{\frac{1}{2}} \quad (22)$$

- (10) The convergence criterion is checked at all radii :

$$|\Delta \epsilon^{P*} - \Delta \epsilon^P| \leq \eta \quad (23)$$

where η is a constant to be chosen on basis of accuracy required and availability of computational time, since a smaller η will increase the number of iterations performed to reach the solution and hence computational time is increased. $\Delta \epsilon^P$ in the above convergence criterion is the value obtained in step '2'. If the convergence criterion is satisfied at all radii at which yield is occurring proceed to step '11', and if the convergence criterion is not satisfied go to step '2' and repeat the calculation (step '2' to step '10') using the newly calculated values of plastic strain increments, viz, $\Delta \epsilon_r^{P*}$, $\Delta \epsilon_\theta^{P*}$ and $\Delta \epsilon_z^{P*}$ obtained in step '8' until convergence is attained.

- (11) At all radii which were not yielding during the thermal load increment considered, the yield function $F(r)$ is calculated from Eq. (5a) to determine whether yield has occurred during the current thermal load increment. If yield occurs, these radii should be allowed to deform plastically during the application of subsequent thermal load increments.
- (12) The previous steps are repeated until the full temperature distribution is applied to the tube.

In the above numerical procedure, the relations for a kinematic hardening material were employed. If any other hardening model is used, exactly the same procedure may be applied with proper employment of the hardening rule, flow rule and yield function.

As regards the isotropic hardening model for the material, the above procedure is followed with minor modifications. Steps '3' and '5' are deleted. In step '8' the corrected values of plastic strain increments are calculated as follows /7/:

$$\epsilon_r^{p*} = \frac{\Delta \bar{\epsilon}^p}{\epsilon_e} \cdot \epsilon_{r1} \quad ; \quad \epsilon_\theta^{p*} = \frac{\Delta \bar{\epsilon}^p}{\epsilon_e} \cdot \epsilon_{\theta 1} \quad ; \quad \epsilon_z^{p*} = \frac{\Delta \bar{\epsilon}^p}{\epsilon_e} \cdot \epsilon_{z1}, \quad (18) \text{ bis}$$

where ϵ_e is the equivalent modified total strain calculated as :

$$\epsilon_e = \left[\frac{2}{3} (\epsilon_{r1}^2 + \epsilon_{\theta 1}^2 + \epsilon_{z1}^2) \right]^{\frac{1}{2}} \quad (19) \text{ bis}$$

and $\Delta \bar{\epsilon}^p$ is calculated as :

$$\Delta \bar{\epsilon}^p = \frac{1}{1 + \frac{2}{3} \left(\frac{1+\nu}{E} \right) (\beta E)} \cdot \left[\Delta \epsilon^p + \frac{2}{3} \left(\frac{1+\nu}{E} \right) (\bar{\sigma} - \sigma_y) \right] \quad (24)$$

$\Delta \epsilon^p$: is as calculated in step '2'

$\bar{\sigma}$: is the equivalent stress at the current point,

σ_y : is the current yield stress at the current point.

and ϵ_{e1} , $\epsilon_{\theta 1}$ and ϵ_{z1} are the deviatoric modified strains calculated as

$$\begin{aligned} \epsilon_{r1} &= \frac{1+\nu}{E} (S_{r,n}) + \Delta \epsilon_r^p, \\ \epsilon_{\theta 1} &= \frac{1+\nu}{E} (S_{\theta,n}) + \Delta \epsilon_\theta^p, \\ \epsilon_{z1} &= \frac{1+\nu}{E} (S_{z,n}) + \Delta \epsilon_z^p, \end{aligned} \quad (25)$$

In step '11', the yield function will be as given by Eq. (12) and in addition to checking points that were not yielding during the load

increment considered, the yield stress of the material should be corrected for points at which yielding has occurred and convergence is reached. For those points, and before proceeding to the next thermal load increment, the new yield stress is calculated as

$$\sigma_y = \bar{\sigma} = \left[\frac{2}{3} (S_\theta^2 + S_r^2 + S_z^2) \right]^{\frac{1}{2}} \quad (26)$$

For other points where yield has not occurred during this load increment, the yield stress should remain unchanged. These steps are repeated until the full temperature distribution is applied to the tube.

The flow chart shown in Fig. 2, indicates the main portions and features for the biaxial program under kinematic hardening assumption. For isotropic hardening, the main features are basically the same except for the relations according to which the new increments of plastic strains are calculated.

SECTION 4

RESULTS AND DISCUSSIONS

4.1 Choice of Numerical Experiments

The two computer programs developed for handling the tube problem, based on the uniaxial and biaxial models respectively, were carefully tested and tried for load sets causing different regimes of deformation. The two programs showed successful converging results for the kinematic and isotropic versions of each program.

A set of actual material constants were fed into these programs. These were chosen for the 304 SS used by Corum and Sartory in their tube ratchetting tests /8/. Thus, comparison between numerical and experimental results was made possible. The properties of 304 SS at an elevated temperature of 900°F (482°C) are represented by the following quantities :

Young's modulus, $E = 23.3 \times 10^6$ psi (16.38×10^5 kp/cm²)

Poisson's ratio, $\nu = 0.3$

Yield stress, σ_y = 11.15×10^3 psi (783.8 kp/cm²)
Coefficient of strain hardening, β = 0.0253
Coefficient of linear thermal expansion, α = 11.09×10^{-6} °F⁻¹ (19.96×10^{-6} °C⁻¹)

Tube dimensions representing Corum's test specimen were also used in these programs. These were as follows :

Inner radius, R_i = 3.845 in. (97.663 mm)
Outer radius, R_o = 4.22 in. (107.188 mm)
Mean radius to thickness ratio, R_m/t = 10.75

In order to complete the information needed to run either one of the two programs, the values of the internal pressure p , the maximum temperature difference ΔT , the number of steps by which this difference is to be incremented, and the value of 'h' which defines the point at which the two straight lines of the bilinear temperature distribution intersect ($h = 0$ for linear distribution), were also needed.

The strategy followed to get the numerical results was as follows :

- (a) Initial investigation of the validity of the adopted numerical procedure. The cornerstone for this validation was the kinematic hardening version of the uniaxial program. A complete study was made on this version, since it is the only one to which a corresponding analytical solution is available /9/. Different sets of loading parameters, as shown in Table I, which covered the full interaction diagram for the specific tube considered, Fig. 3, were used.
- (b) Upon verification of the validity of the kinematic hardening version of the uniaxial program, the segment of the program concerning the hardening rule was modified to accommodate the isotropic hardening rule. Some loading samples, as shown in Table II, were then tried.
- (c) Then, being sure that the adopted numerical procedure was in good order, the uniaxial program was further modified to yield the biaxial versions for both kinematic and isotropic hardening models, with the numerical technique maintained unchanged.

- (d) The biaxial versions were then used to get results for the pressure and temperature difference used by Corum in his test ($p = 700$ psi, $\Delta T = 167^{\circ}\text{F}$).

Several test runs were done for each of the versions used until satisfactory performance was achieved and enough experience was earned. Only computer runs of interest were completed and printed. Results are presented in the following.

4.2 Results

For each of the loading sets mentioned above the corresponding version of the program was used to calculate stresses and strains at 51 equally-spaced points, covering the full thickness of the tube for the uniaxial versions, and 26 points for the biaxial version. The resulting stresses and strains were printed after each half thermal cycle and for 30 complete cycles.

4.2.1 Kinematic hardening results

(a) For a pressure p of 100 psi and a temperature difference ΔT of 50°F at the inner tube surface ($x=1$). Fig. 4 shows the resulting stress distributions for the first cycle (solid for the cooling half cycle and dotted for the heating half), and the growth of total strain ϵ with cycling. During the cooling half of the first cycle, plastic deformation occurs only at the inner side of the tube (from $x = 0.92$ to $x = 1$), and no plastic deformation is observed during the second half of the first cycle. Further cycling shows no growth of plastic strains and the stress distributions are exactly the same as in the first cycle. The cyclic steady state, as could be seen from Fig. 4(a), (b), is then an elastic shakedown. This agrees also with analytical predictions for the pressure and temperature difference employed (as could be seen from Fig. 3). The value of the plastic front ($x = 0.92$), as well as stresses and strains at all points are also found to be the same as calculated theoretically.

(b) For $p = 100$ psi and $\Delta T = 200^{\circ}\text{F}$. Fig. 5 gives the resulting stresses for the first cycle and the growth of the total plastic strain with further cycling. During the cooling half of the first cycle, compressive plastic deformations take place at the outer tube side from $x = 0$ to $x = 0.36$, meanwhile tensile

plastic deformations occur at the inner side from $x = 0.58$ to $x = 1$. During the heating half of this cycle only compressive plastic deformations take place at the inner tube side from $x = 0.72$ to $x = 1$. Further cycling gives exactly the same stress distributions as in the first cycle. Hence, the range from $x = 0.72$ to $x = 1$ is undergoing cyclic plasticity and no total strain growth is observed. The cyclic steady state is thus cyclic plasticity F_1 , and has been reached after the first cycle. The analytical results for the same operating conditions and corresponding regime of deformation were found to be exactly the same as the numerical predictions.

(c) For $p = 100$ psi and $\Delta T = 300^\circ\text{F}$. Results are shown in Fig. 6. During the first half cycle, plastic strains are developed at both sides of the tube; from $x = 0$ to $x = 0.4$ compressive yielding occurs, and from $x = 0.56$ to $x = 1$ tensile yielding takes place. During the second half cycle plasticity is still seen at both sides; tensile from $x = 0$ to $x = 0.38$ and compressive from $x = 0.65$ to $x = 1$. Further cycling gives exactly the same stress distributions seen in the first cycle. Hence the regions from $x = 0$ to $x = 0.38$ and from $x = 0.66$ to $x = 1$ are undergoing cyclic plasticity while no total strain growth is observed. The cyclic steady state in this case is cyclic plasticity F_2 and is reached after the first cycle. These predictions agree also with analytical predictions for the same operating conditions.

(d) For $p = 100$ psi and $\Delta T = 100^\circ\text{F}$. Fig. 7 gives the resulting stresses for the first cycle and the growth of the total plastic strain with further cycling. During the cooling half of the first cycle, tensile plastic deformation takes place at the inner side of the tube from $x = 0.7$ to $x = 1$, while during the heating half of this cycle compressive plastic deformation takes place also at the inner side from $x = 0.96$ to $x = 1$. Further cycling gives exactly the same stress distributions. Hence, the range from $x = 0.96$ to $x = 1$ at the inner side is undergoing cyclic plasticity while no total strain growth is observed. The cyclic steady state is thus cyclic plasticity F_3 and is reached after the first cycle. Similar analytical results were obtained for the same pressure and temperature difference.

(e) For $p = 900$ psi and $\Delta T = 50^\circ\text{F}$. Fig. 8 gives the resulting stress distributions during the first, tenth and twentieth cycles. The total strain growth is shown in Fig. 12. It is clear, in this case, that plastic deformations

occur on one side only of the tube during each half cycle, and during the subsequent half this side is fully elastic and the other half starts to yield. Such a mechanism is maintained during all cycles, thus causing a growing total plastic strain over the cycles (ratchetting) with a decreasing rate of growth until a cyclic steady state of elastic shakedown is reached. It can be seen from Fig. 8, that the plastic fronts y_1 and y_2 are getting closer with further cycling until they coincide at $x = 0.56$ when the steady state is approached. This is seen almost after 18 cycles. From Fig. 12, it can be seen that the rate of growth of the total strain is large at the beginning and is decreasing gradually until the steady state is observed with a value for the total strain of about 0.24%. This is considered the asymptotic ratchet strain for the loads imposed. The observed ratchetting regime is R_1 . Similar analytical results were obtained under the same conditions.

(f) For $p = 200$ psi and $\Delta T = 300^\circ\text{F}$. The resulting stress distributions are shown in Fig. 9 for the first and almost all subsequent cycles. The total strain growth with cycling is shown in Fig. 12. In this case plastic deformations are taking place on both sides of the tube during each half cycle in such a fashion as to increase the total strain over each half cycle by a certain decreasing increment until a steady state of reversed plasticity, F_2 , is reached. For the case considered, compressive plastic deformations occur at the outer side from $x = 0$ to $x = 0.38$ and tensile plastic deformations occur at the inner tube side from $x = 0.52$ to $x = 1$ during the cooling half of any cycle. For the heating half cycle, the situation is reversed and tensile plasticity takes place from $x = 0$ to $x = 0.48$ whilst compressive plasticity occurs from $x = 0$ to $x = 0.66$ to $x = 1$. The cyclic steady state is reached after almost 10 cycles with an asymptotic ratchet strain of -0.01% . The observed ratchetting regime for this case is R_2 . Similar analytical results were found under the same operating conditions.

(g) For $p = 900$ psi and $\Delta T 100^\circ\text{F}$. The resulting stress distributions are shown in Fig. 10 for the first, tenth and twentieth cycles. The total strain growth is shown in Fig. 12. Here, a phase of transient ratchetting similar to R_1 is seen up to the seventh cycle until a sufficient degree of hardening is attained which initiated reversed plasticity at the inner tube side in a

fashion similar to F_1 . With further cycling the plastic fronts for two subsequent half cycles are getting closer, and after the heating half of the 7th cycle a new compressive plastic zone is observed at the inner side of the tube. The size of this zone is increased with cycling till it covers the range from $x = 0.96$ to $x = 1$, at the steady state. This range is therefore undergoing cyclic plasticity F_1 . The total accumulated plastic strain reaches its asymptotic value of about 0.65% after 25 cycles where the ratchetting plastic fronts coincide at $x = 0.55$. A cyclic steady state of reversed plasticity at the inner tube side is thus maintained. These results are found to be in a very good agreement with analytical results under similar conditions.

(h) For $p = 900$ psi and $\Delta T = 300^\circ\text{F}$. The resulting stress distributions - using the K.H. uniaxial version - are shown in Fig. 11 for the first and tenth cycles (which was almost the same for all subsequent cycles). The total strain growth is shown in Fig. 12. For this case, ratchetting is observed at the first few cycles in a mode similar to R_3 until a sufficient degree of hardening is attained to initiate reversed plasticity at the outer tube side (this was observed after the 6th cycle), thus, giving rise to a ratchetting regime R_2 which will have a steady state of cyclic plasticity F_2 . The cyclic steady state is reached almost after 15 cycles, with the ratchetting plastic fronts coinciding at $x = 0.5$ and reversed plasticity covering the ranges from $x = 0$ to $x = 0.38$ at the outer side and from $x = 0.66$ to $x = 1$ at the inner side. The accumulated total plastic strain at the steady state is about 1.3% which is to be considered the asymptotic value for the ratchetting strain. The observed ratchetting regime is called R_4 . Analytical evaluation of stresses, strains, ratchetting strains and asymptotic strain gave similar figures to those obtained numerically.

4.2.2 Istropic hardening results

(a) When the isotropic hardening uniaxial version of the program was used for $p = 100$ psi and $\Delta T = 50^\circ\text{F}$, the results were exactly equal to those obtained from the kinematic hardening version. Shakedown was observed after the first cycle. The stress distributions and total strain growth are therefore as shown in Fig. 4. The reason for the similarity between kinematic and isotropic hardening results is due to the fact that the effect of the hardening

rule on a virgin material can be seen only when there is more than one half cycle during which plasticity occurs. Since in the shakedown regime, no plasticity takes place after the first half of the first cycle, it is then evident that the stresses and strains at the end of this half cycle are not yet influenced by the hardening rule.

(b) For $p = 100$ psi and $\Delta T = 100^{\circ}\text{F}$. The results obtained are also as shown in Fig. 5. The features of the stress distributions over any cycle and the trend for cumulative strain growth are found to be exactly the same as those obtained from the K.H. version for the same loads, though the mode of deformation observed was elastic shakedown after the second cycle compared with cyclic plasticity for kinematic hardening results. No plastic deformations were seen after the second cycle since the degree of hardening reached was sufficient to prevent the formation of any new plastic strains.

(c) For $p = 100$ psi and $\Delta T = 200^{\circ}\text{F}$. The isotropic hardening results are coincidentally similar to those obtained for kinematic hardening and a state of cyclic plasticity with a slight decreasing reversed plastic strain was observed with further cycling. No total strain growth was observed, as seen from Fig. 6 which applies here also. Nevertheless it is worth warning that the similarity observed up till this point between the isotropic and kinematic hardening results, is not a common rule for all results. It is confined only to the stress distributions and trend of strain growth, but not the regime of deformation, and only for the loading combinations considered. For the considered point ($p = 100$ psi and $\Delta T = 200^{\circ}\text{F}$), cyclic plasticity at both sides of the tube was observed only up to the fourth cycle after which a state of elastic shakedown was reached.

From the above three examples, it can be generalized that for a tube made of an isotropically hardening material and for any loading combinations, the cyclic steady state will always be an elastic shakedown.

4.2.3 Results for load conditions used in Corum's test

For $p = 700$ psi and $\Delta T = 167^{\circ}\text{F}$ which correspond to the conditions of Corum's test /8/, the kinematic hardening uniaxial version of the program gave the stress distributions shown in Fig. 13 ($h = 0.328$) for the first, tenth, twentieth and thirtieth cycles. The corresponding total strain growth

is shown in Fig. 15. The observed mode of deformation was ratchetting R_3 in which cyclic plasticity was observed at the inner tube side. It covers the range from $x = 0.9$ to $x = 1$ during the first cycle and increases gradually till the steady state is approached. The steady state is almost reached after 25 cycles. The ratchetting plastic fronts are at $x = 0.48$ and $x = 0.54$ after 30 cycles. Plasticity covers the range from $x = 0.78$ to $x = 1$, and the total cumulative strain is about 0.73%.

For the same pressure (700 psi) and temperature difference (167°F), the linear temperature distribution ($h = 0$) was tried and the K.H./uniaxial results are as shown in Figs. 14 and 15. The mode of deformation observed is also ratchetting but regime R_2 with cyclic plasticity seen from the first cycle at both sides of the tube covering the ranges from $x = 0$ to $x = 0.02$ and from $x = 0.98$ to $x = 1$. These ranges increase with further cycling till the steady state is reached after almost 20 cycles. It covers then the ranges from $x = 0$ to $x = 0.12$ at the outer skin and from $x = 0.88$ to $x = 1$ at the inner skin. The observed cyclic steady state is reversed plasticity, regime F_2 . The value of the cumulative strain growth at the end of the 30th cycle is 0.6% which is lower than that for $h = 0.328$.

When the isotropic hardening uniaxial version was used for Corum's test conditions, the stress distributions for the bilinear temperature distribution ($h = 0.328$) are as shown in Fig. 16, for the first, tenth, twentieth and thirtieth cycles. The strain growth with cycling is shown in Fig. 18. The observed mode of deformation is ratchetting with cyclic plasticity seen from the first cycle at the inner tube side, covering the range from $x = 0.96$ to $x = 1$. This range does not very much extend with cycling. After 30 cycles it covers from $x = 0.94$ to $x = 1$. The ratchetting plastic fronts are clearly approaching each other with cycling. At the first cycle they were at $x = 0.46$ and $x = 0.68$, meanwhile at the 30th cycle they were at $x = 0.5$ and $x = 0.56$. A pronouncedly increasing ratchetting strain was still observed after the 30th cycle and no sign of the steady state was yet seen. The total cumulative plastic strain was 1.33% which is almost twice as much as that obtained from kinematic hardening results.

For the linear temperature distribution ($h = 0$), the isotropic hardening/uniaxial results are as shown in Figs. 17 and 18. The deformation mode is pure

ratchetting with no reversed plasticity zones at either sides of the tube. This ratchetting mode is similar to R_1 . The ratchetting plastic fronts are at $x = 0.36$ and $x = 0.62$ at the first cycle and generally approach each other till they reach $x = 0.5$ and $x = 0.52$ after 30 cycles. The steady state is not clearly seen after 30 cycles, since the incremental strain growth was still pronounced. The general trend of the total strain growth curve, Fig. 18, shows that the steady state is expected after few more cycles following the 30th. The total strain growth is 0.8%, which is 1.25 times higher than the corresponding kinematic hardening value.

A new set of results for the same test conditions is produced using the biaxial tube program. This program was tested for validity of performance for various loading points on the Bree diagram and was found to be numerically reliable. When the kinematic hardening version of this program was used, the results for Corum's test conditions were as shown in Figs. 19 and 21 for the bilinear temperature distribution ($h = 0.328$) and in Figs. 20 and 21 for the linear temperature distribution. For the first case, the hoop stress (σ_θ) distributions during the first, tenth and twentieth cycles are shown in Fig. 19, while the growth of the hoop strain at the outer surface of the tube, $\epsilon_\theta(0)$, is as shown in Fig. 21. Ratchetting was also observed here, with smaller ratchetting strain increments and higher rate of decrease of plastic strain increments with cycling, as compared to the corresponding values (Fig. 15) obtained for the uniaxial model under similar conditions of hardening rule and temperature distribution. A cyclic steady state of reversed plasticity was observed after 18 cycles with an asymptotic value of the hoop strain at the outer tube surface of 0.34%. This is almost half of that obtained from the uniaxial model results.

The linear distribution of temperature under the same loading conditions ($p = 700$ psi and $\Delta T = 167^\circ\text{F}$) showed similar trends. Ratchetting was also observed but with lower values and higher rates of the plastic strain increments than those for $h = 0.328$. Therefore, the steady state was observed earlier, after 15 cycles, with an asymptotic value of the hoop strain at the outer radius of the tube of 0.25% which is almost $3/4$ the corresponding value for $h = 0.328$. The hoop stress distributions during the first, tenth and

twentieth cycles are as shown in Fig. 20, and the hoop strain growth is as shown in Fig. 21.

Similar to the situation observed from the uniaxial model predictions, the isotropic hardening predictions, using the biaxial model, showed excessive estimation of ratchetting strains, as compared with kinematic hardening predictions for both linear ($h = 0$) and bilinear ($h = 0.328$) temperature distributions. Since isotropic hardening assumptions are not in a good correlation with actual observed behaviour of 304SS, only the hoop strains at the outer tube surface - being of prime importance - are shown in Fig. 21. The distribution of hoop stresses during certain cycles is similar in form, but different in magnitude, to those shown in Figs. 19 and 20.

As could be seen from Fig. 21, the total cumulative hoop strain at the outer tube surface after 30 cycles, is 0.6% for $h = 0.328$, and 0.32% for $h = 0$. It is seen also that the steady state was not reached for $h = 0.328$ and was reached after almost 25 cycles for $h = 0$. A summary of all the test point results are given in Table III.

For comparison with experimental results, the most suitable sets of numerical results would be those obtained when kinematic hardening assumptions together with the bilinear temperature distribution were adopted. This is simply because the hardening characteristics of type 304 stainless steel are better approximated by kinematic hardening rule than by isotropic hardening, and the actual thermal gradient is better approximated by a bilinear distribution (with $h = 0.328$) rather than a linear one. Fig. 22 shows the experimental and numerical results for 13 complete cycles. The numerical predictions are those obtained from both the uniaxial and biaxial models of the tube, under kinematic hardening assumptions and a bilinear temperature distribution. It is clear that the uniaxial model predictions excessively overestimate the ratchet strains, whilst the biaxial model predictions slightly underestimate them. This argument applies also to the plastic strain increment over each cycle. After 13 cycles, the uniaxial model gives a cumulative strain of 1.95 times the actual observed strain and a plastic strain increment of 3 times the experimental value, meanwhile the biaxial model gives a cumulative strain of only 0.89 times the experimental and a plastic strain increment of only 1.22

times the experimentally observed plastic strain increment. It is therefore evident that the biaxial model gives much better predictions for the tube problem than the uniaxial. The small differences between the experimental results and the available biaxial model predictions may be due to the combined effect of the bilinear approximation of the actual thermal gradient, the elastic-linearly plastic assumption as the flow rule for the tube material, the kinematic hardening assumption as the hardening rule for the tube material, and the neglect of changes in material properties when its temperature is changed. It is expected that better predictions will be obtained, if the above considerations are more accurately implemented in our numerical procedure.

SECTION 5

CONCLUSIONS AND RECOMMENDATIONS

The problem of a tube subjected to steady internal pressure and cyclic radial thermal gradient has been investigated. A new numerical procedure was constructed to solve the same problem. The validity of this numerical procedure was extensively verified through comparisons with available analytical solutions, namely, that based on the kinematic hardening assumption for an elastic-linearly plastic tube material and the uniaxial model of the tube.

The numerical technique has been further elaborated to accommodate the isotropic hardening rule instead of the kinematic hardening and to utilize a more generalized biaxial tube model instead of the uniaxial one. The main results of this work are summarized again hereafter as main conclusions.

- (a) The adopted numerical procedure is a successful one. Its predictions, in the case of uniaxial model with kinematic hardening assumptions, were in a very good agreement with analytical results. Expected regimes of deformation were exactly as predicted from the full solution map of Fig. 3. Asymptotic ratchet strains were also the same as those obtained from the same figure. The stresses at any point of the tube thickness during any cycle and the values of the plastic fronts were almost the same as calculated analytically.

- (b) The numerical solution is not confined to the kinematic hardening assumption only, but also isotropic hardening was made to replace the kinematic one, for which no analytical solutions are available, and it was possible, therefore, to reach the thermo-elasto-plastic solution for the tube problem under any loading conditions. Shakedown, reversed plasticity and ratchetting were also observed here with a common cyclic steady state of shakedown for all regimes. This is due to the fact that under isotropic hardening assumption the size of the yield surface is increased with the increasing number of load cycles until a sufficient degree of hardening is attained, such that the loads are no longer able to cause plasticity and fully elastic behaviour prevails then (shakedown).
- (c) A new model has been developed, for which the actual stress and strain conditions were maintained. This model has been found more accurate and superior to the uniaxial model initially proposed and that has been widely adopted in most of the trials to solve the tube problem. The biaxial tube model is very close to actual conditions where all stresses and strains are present in the three dimensions, i.e. $\sigma_r, \sigma_\theta, \sigma_z, \epsilon_r, \epsilon_\theta$ and ϵ_z . Since the tube problem is one in which axial symmetry exists, all stresses and strains - except ϵ_z - were dependent on the radius only. The axial strain ϵ_z is constant, since the tube was assumed to be in a state of generalized plane strain. Due to its faithful representation of the tube, the results obtained using the biaxial model has been found, as expected, much closer to actual experimental values. Also, the biaxial model predictions of ratchet strains, when isotropic hardening was assumed, were well above those obtained from the same model but with kinematic hardening assumption, Fig. 21; a situation similar to that observed for the uniaxial model.
- (d) The effect of the hardening rule on the ratchet strain and number of cycles needed to reach the steady state has been found so pronounced. Isotropic hardening assumption has resulted in greater ratchet strains than those produced under the kinematic hardening assumption for both the uniaxial and biaxial tube models. Also the tendency to reach the cyclic state has been found to be at a relatively smaller number of

thermal cycles under kinematic hardening rule than those for the isotropic one. This was true for the uniaxial as well as the biaxial tube model.

- (e) The effect of 'h', the bilinear intersection, on the ratchet strains and the arrival at the steady state was also a very clear one. For both isotropic and kinematic hardening and for both the uniaxial and biaxial tube models the ratchet strains were relatively higher in the case of a bilinear temperature distribution ($h=0.328$) than that for the linear distribution ($h = 0$). The cyclic steady state was arrived at, considerably earlier in the case of a linear distribution than a bilinear one. Table III shows the above effect quantitatively.
- (f) The difference found between the experimental and biaxial model results (the latter being about 10% lower than the former), is not as dreadful as those observed when Bree's uniaxial tube model was used (about 95% above the actual results). Possible sources of error in the load and material modeling are :
 - i. the elastic-linearly plastic assumption with $\beta = 0.0253$ for the tube material,
 - ii. the kinematic hardening assumption for the 304SS,
 - iii. the bilinear temperature distribution with $h = 0.328$, which is only an approximation,
 - iv. the constancy of material properties assumption, which neglects the effect of temperature on properties.

Nevertheless it is worth mentioning that the adopted numerical technique can handle any type of flow rule, hardening rule, temperature distribution and any set of data describing the change of material properties with temperature, once these are available. Even the control history can be changed from cycle to cycle. Also, any tube dimensions can be used, including thick-walled tubes, since the biaxial model simulates basically thick-walled tubes. The full solution map for a certain tube (Bree diagram) can then be numerically constructed for any set of material data.

From the foregoing, it is clear that the flow rule and the hardening rule play a very important role in the deformational pattern of the structure. Although the kinematic hardening rule reproduces the observed Bauschinger effect upon stress reversals, the cyclic steady state under conditions of fully reversed strains, is reached during the first cycle. On the other hand, isotropic hardening theory reaches a purely elastic cyclic state after a finite number of cycles and does not show a Bauschinger effect. The two theories are seen to provide two extreme limits of behaviour, between which actual material response as well as all remaining hardening theories lie, Fig. 23. In this respect, various efforts have been done recently towards a more accurate description of material behaviour. Among the most important models presented in the literature are those of Mroz /10/, Eisenberg /11/ and Dafalias and Popov /12/.

Mroz /10/ proposed a material model which utilizes a field of work-hardening moduli as shown in Fig. 24. The monotonic stress-strain curve is approximated by a number of linear segments. During monotonic loading, the stress increases in steps and plastic strain is defined by the appropriate work-hardening modulus.

Eisenberg /11/ assumed the universal applicability of Ramberg-Osgood relations, $\epsilon = \sigma/E + (\sigma/k)^n$ for the monotonic and subsequent branches of the hysteresis loops and developed growth laws for the material parameters k and n on the basis of observed hardening of 304SS.

Dafalias and Popov /12/ introduced the concept of a limit or bounding surface which encloses the yield surface in stress space, Fig. 25. The limit surface can translate, shrink or expand but never intersect with the yield surface. The plastic tangent depends on the proximity between the two surfaces at the point of loading. The material exhibits a memory of past loading history by means of plastic internal variable and a projected foresight by means of the proximity between actual and image stress points.

It is recommended that these and other models should be used in further work related to the tube problem.

SECTION 6

REFERENCES

- 1- Eleiche, A.M. and Megahed, M.M., "Inelastic Deformation of Metals and Structures Under Dynamic and Quasi-Static Cyclic Loading", Annual Technical Report to ERO, Contract Number DAJA37-81-C-0236, May 1983.
- 2- Eleiche, A.M. and Megahed, M.M., "Inelastic Deformation of Metals and Structures Under Dynamic and Quasi-Static Cyclic Loading", Annual Technical Report to ERO, Contract Number DAJA37-81-C-0236, May 1982.
- 3- Miller, D.R., "Thermal Stress Ratchet Mechanism in Pressure Vessels", J. Basic Eng., Trans. ASME, Series D, 190-196 (1959)
- 4- Bree, J., "Incremental Growth due to Creep and Plastic Yielding of Thin Tubes Subjected to Internal Pressure and Cyclic Thermal Stresses", J. Strain An., 3, 122-127 (1968).
- 5- Mulcahy, T.M., "An Assessment of Kinematic Hardening Thermal Ratchetting", J. Eng. Mat. Tech., Trans. ASME, 96 214-221 (1974).
- 6- Barsoum, R.S., "A Convergent Method for Cyclic Plasticity Analysis with Application to Nuclear Components", Int. J. Numer. Meth. Eng., 6, 227-236 (1973).
- 7- Mendelson, A., Plasticity: Theory and Applications, 1st Ed., McMillan Co., New York, 123-127 (1968).
- 8- Corum, J.R. and Sartory, W.K., "Elastic-Plastic-Creep Analysis of Thermal Ratchetting in Straight Pipe and Comparison with Test Results", ASME Paper 73-WA/PVP-4, 1-11 (1973).
- 9- Megahed, M.M., "Influence of Hardening Rule on the Elasto-Plastic Behaviour of a Simple Structure Under Cyclic Loading", Int. J. Mech. Sci., 23, 169-182 (1981).
- 10- Mroz, Z., "An Attempt to Describe the Behaviour of Metals Under Cyclic Loads Using a More General Work-Hardening Model", Acta Mechanica, 7, 199-212 (1969).
- 11- Eisenberg, M.A., "A Generalization of Plastic Flow Theory with Application to Cyclic Hardening and Softening of Metals", J. Eng. Mat. Tech., 98, 221-228 (1976).
- 12- Dafalias, Y.F. and Popov, E.P., "Plastic Internal Variable Formalism of Cyclic Plasticity", J. Appl. Mech., 98, 645-651 (1976).

TABLE I - Internal pressure - temperature difference combinations and corresponding increment of temperature difference and expected mode of behavior used for inspecting the uniaxial program with kinematic hardening assumption

p (psi)	100	100	100	100	900	200	900	900
ΔT ($^{\circ}F$)	50	200	300	100	50	300	100	300
$\Delta T'$ ($^{\circ}F$)	20	20	30	5	20	30	20	30
mode	S	F ₁	F ₂	F ₃	R ₁	R ₂	R ₃	R ₄

TABLE II - Internal pressure - temperature difference combinations and corresponding increments of temperature difference used in the uniaxial program with isotropic hardening assumption

p	100	100	100	700
ΔT	50	100	200	167
$\Delta T'$	20	20	20	10

TABLE III - Summary of numerical results for the load conditions (p = 700 psi and $\Delta T = 167^{\circ}F$) used by Corum in his tube ratchetting tests

Model	Uniaxial Model				Biaxial Model			
Hardening rule	K.H.		I.H.		K.H.		I.H.	
h	0.328	0	0.328	0	0.328	0	0.328	0
Cumulative strain % after 30 cycles	0.73	0.6	1.33	0.9	0.34	0.25	0.6	0.32
Cyclic steady state	reached after 15 cycles	reached after 20 cycles	not reached	not reached	reached after 18 cycles	reached after 15 cycles	not reached	reached after 25 cycles

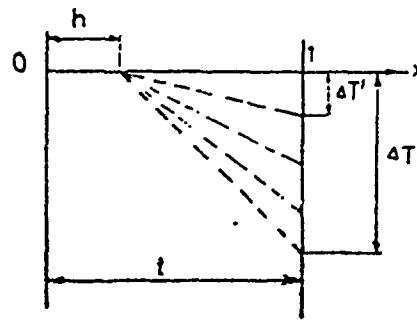


Fig. 1 Total thermal gradient incrementation

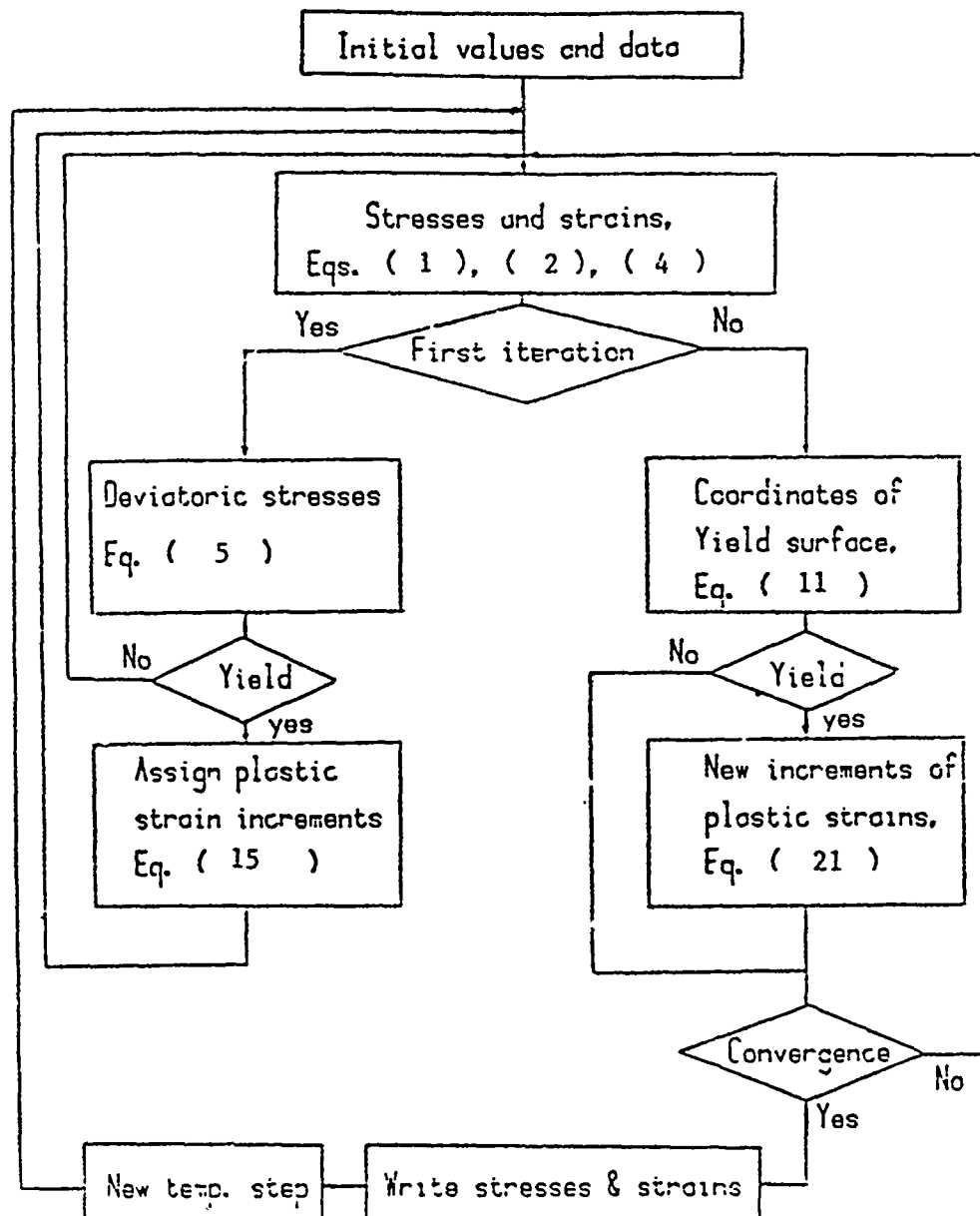


Fig. 2 Simplified flow chart for the biaxial program

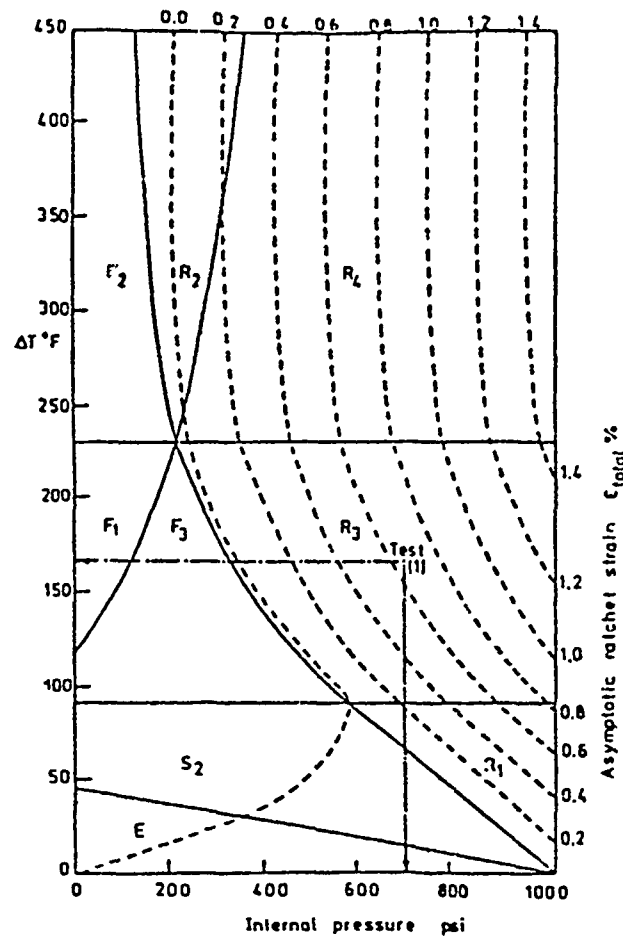


Fig. 3 Full interaction diagram for a tube made of 304 SS with kinematic hardening assumption and bilinear temperature distribution ($\beta = 0.0253$, $h = 0.328$)

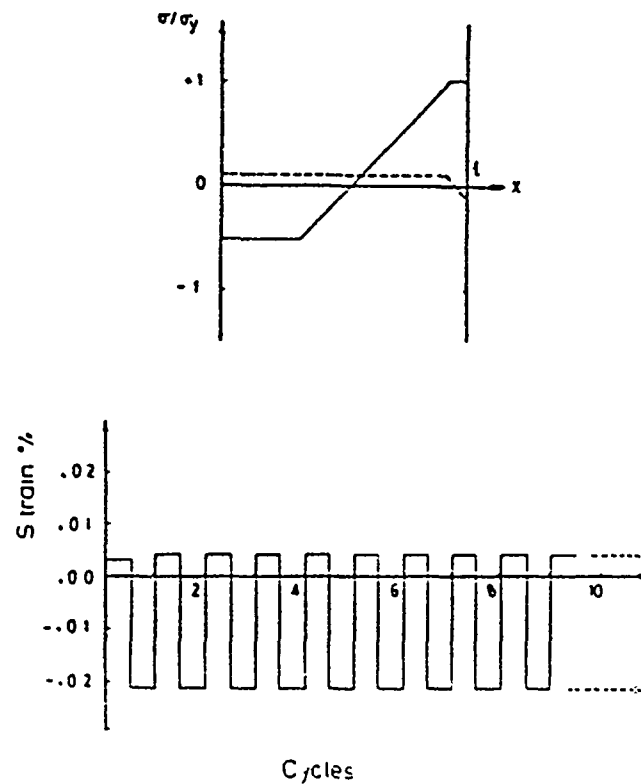


Fig. 4 Cyclic stress distributions and strain growth for $p = 100$ psi $\Delta T = 50^\circ\text{F}$ (Regime S)

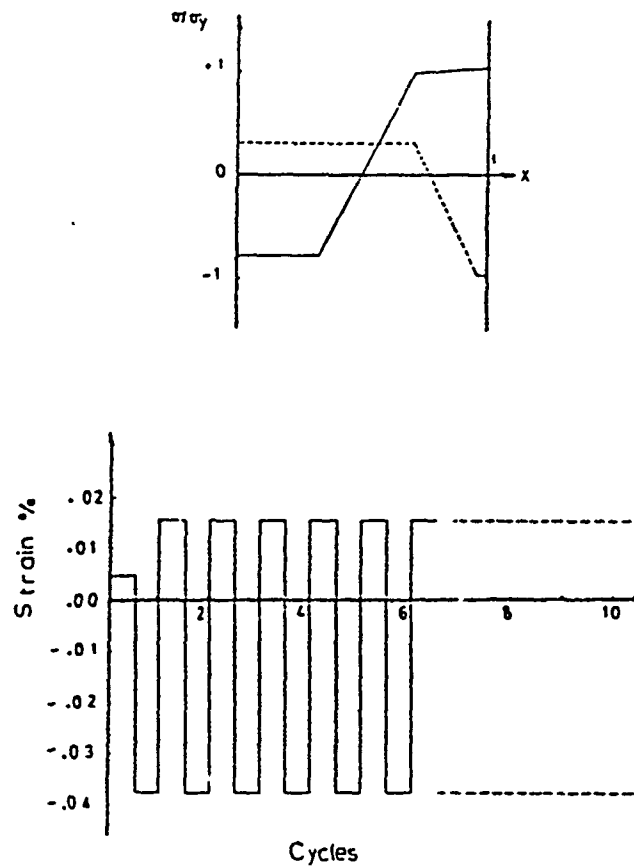


Fig. 5 Cyclic stress distributions and strain growth for $P = 100$ psi and $\Delta T = 200^\circ\text{F}$ (Regime F_1)

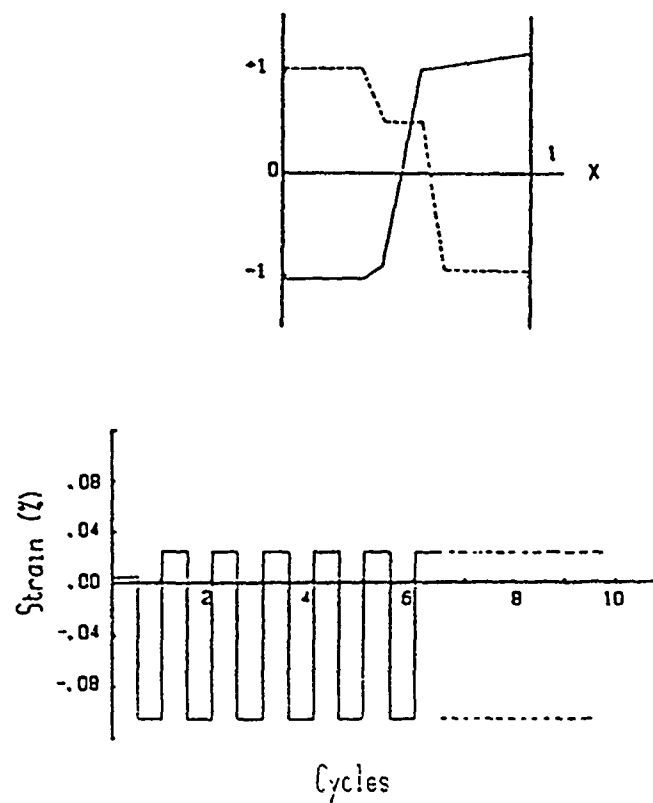


Fig. 6 Cyclic stress distributions and strain growth for $p = 100$ psi and $\Delta T = 300^\circ\text{F}$ (Regime F_2)

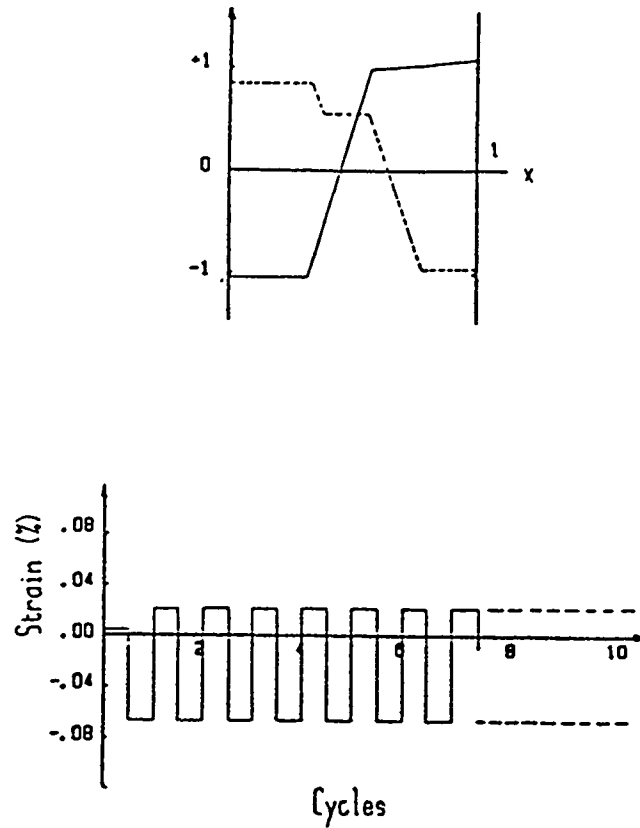


Fig. 7 Cyclic stress distribution and strain growth for $P = 100$ psi and $T = 100^\circ\text{F}$ (Regime F_3)

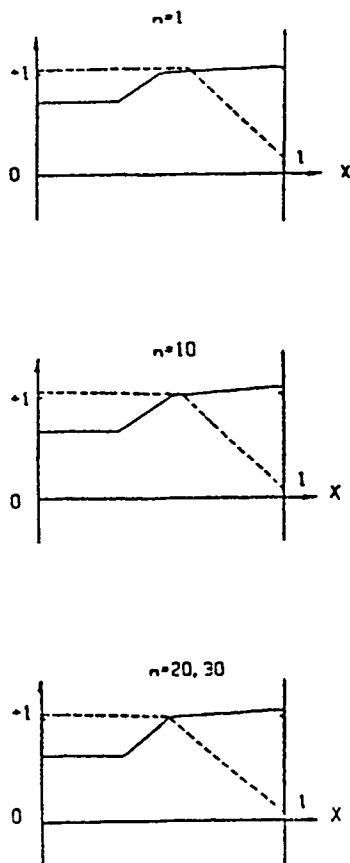


Fig. 8 Cyclic stress distributions for $p = 900$ psi and $\Delta T = 50^\circ\text{F}$ (Regime R_1)

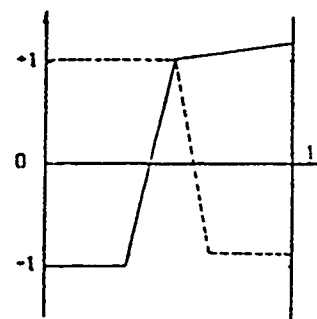


Fig. 9 Cyclic stress distributions for $p = 200$ psi and $\Delta T = 300^\circ\text{F}$ (Regime R_2)

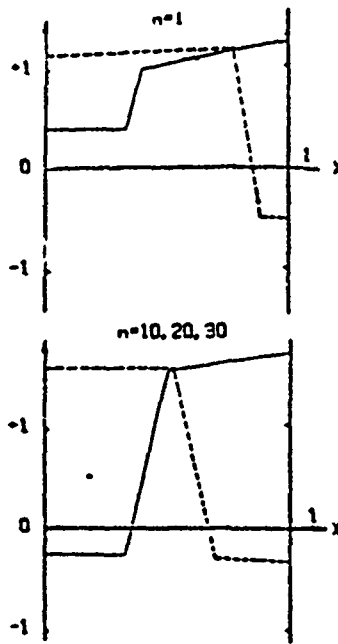


Fig. 10 Cyclic stress distributions for $p = 900$ psi and $\Delta T = 100$ F (Regime R_3)

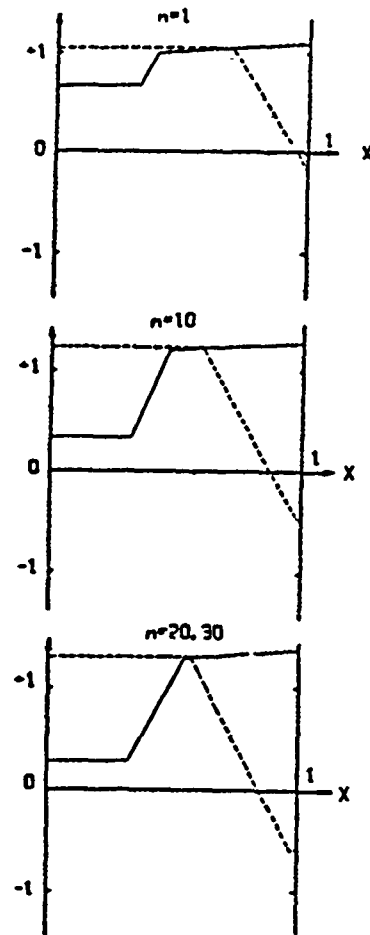


Fig. 11 Cyclic stress distributions for $p = 900$ psi and $\Delta T = 300$ F (Regime R_4)

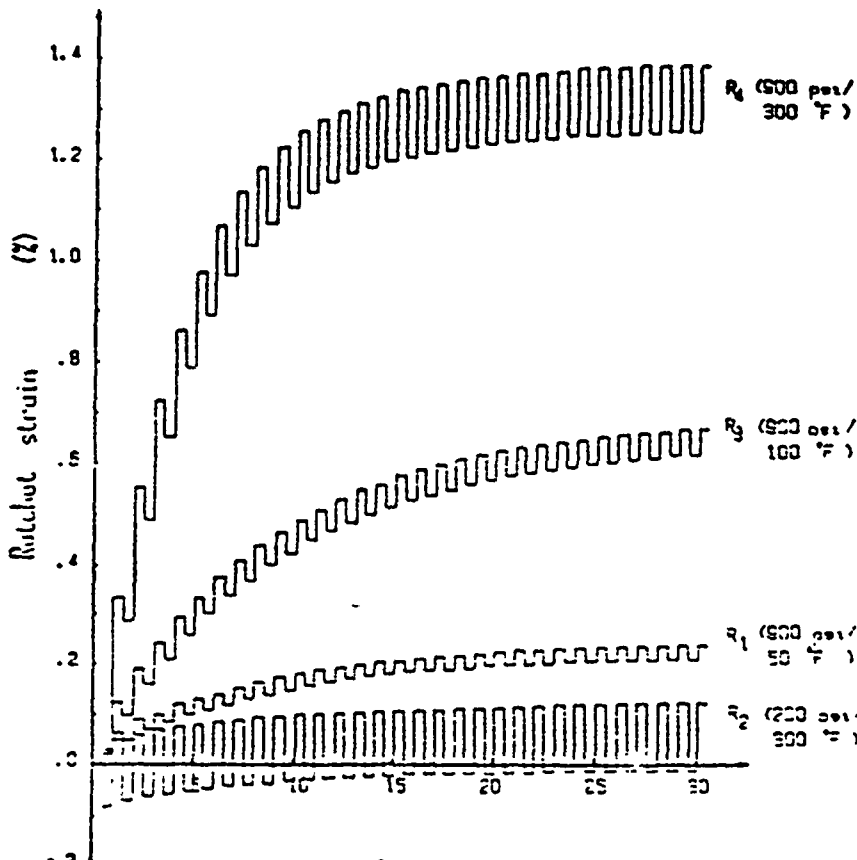


Fig. 12 Cumulative strain growth for the different ratchetting regimes

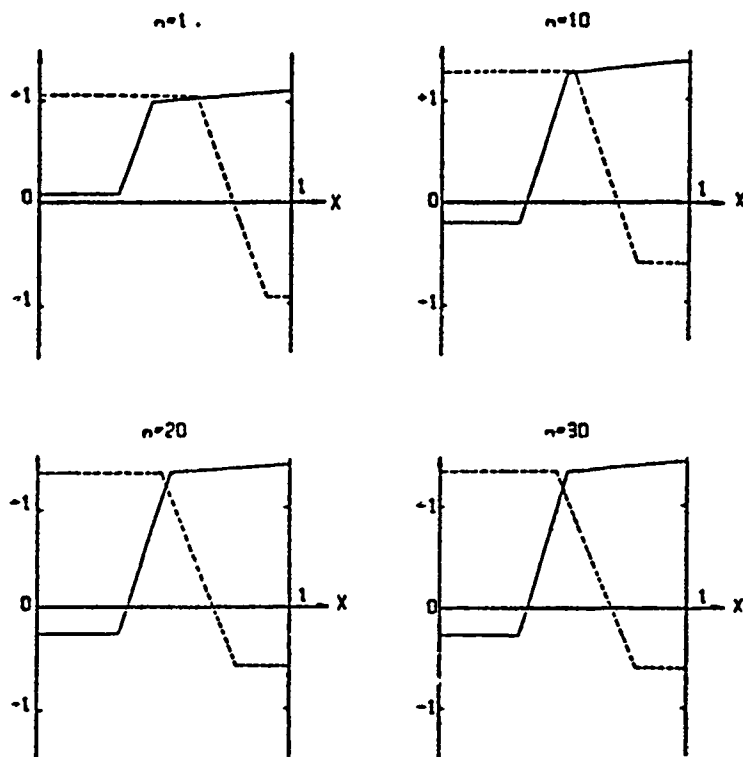


Fig. 13 Cyclic stress distributions for $p = 700$ psi and $\Delta T = 167^{\circ}\text{F}$ (K.H. - uniaxial version with $h = 0.328$)

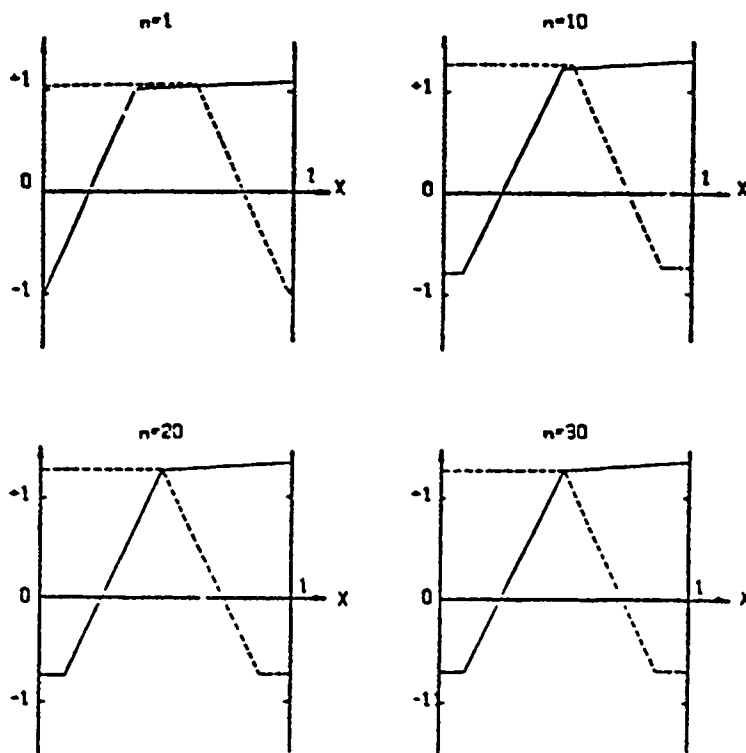


Fig. 14 Cyclic stress distributions for $p = 700$ psi and $\Delta T = 167^{\circ}\text{F}$ (K.H. - uniaxial version with $h = 0$)

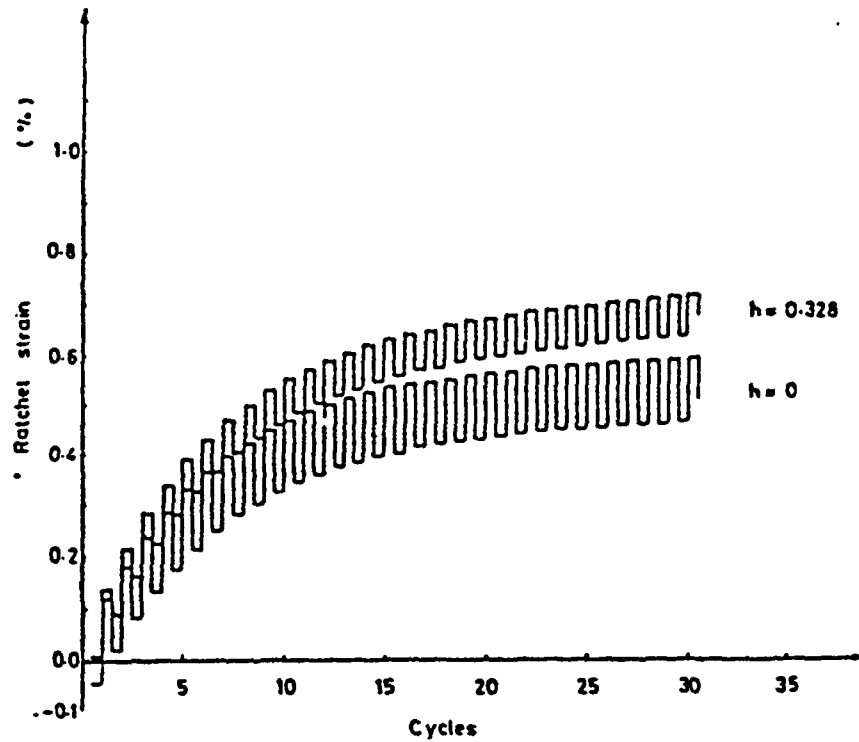


Fig. 15 Ratchet strain growth for $p = 700$ psi and $\Delta T = 167^{\circ}\text{F}$
(K.H. - uniaxial version for both $h = 0$ and $h = 0.328$)

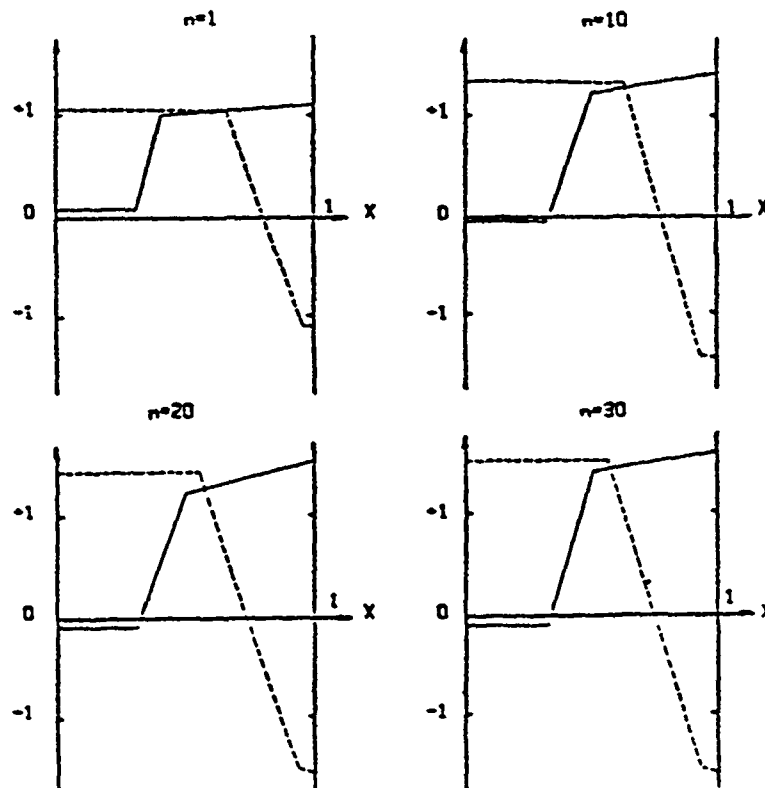


Fig. 16 Cyclic stress distribution for $p = 700$ psi and $\Delta T = 167^{\circ}\text{F}$
(I.H. - uniaxial version with $h = 0.328$)

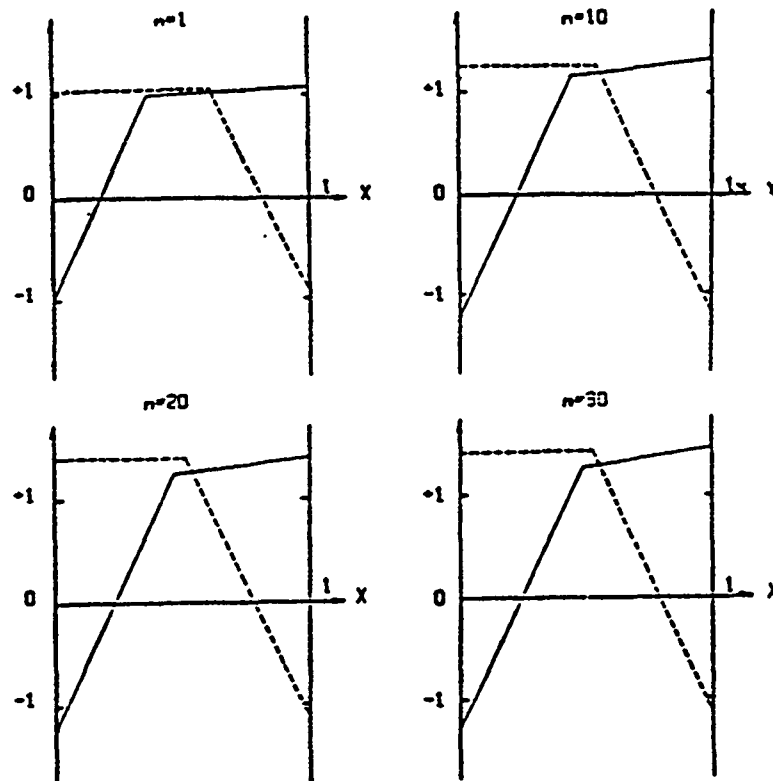


Fig. 17 Cyclic stress distributions for $p = 700$ psi and $\Delta T = 167^\circ\text{F}$ (I.H. - uniaxial version with $h = 0$)

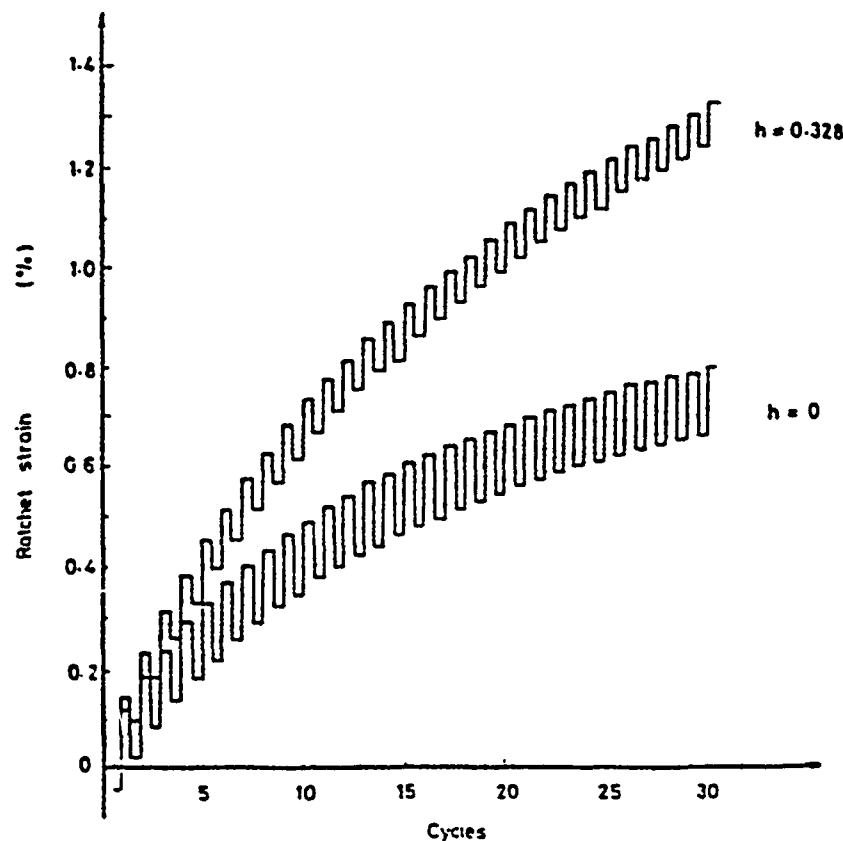


Fig. 18 Ratchet strain growth for $p = 700$ psi and $\Delta T = 167^\circ\text{F}$ (I.H. - uniaxial version for both $h=0$ and $h = 0.328$)

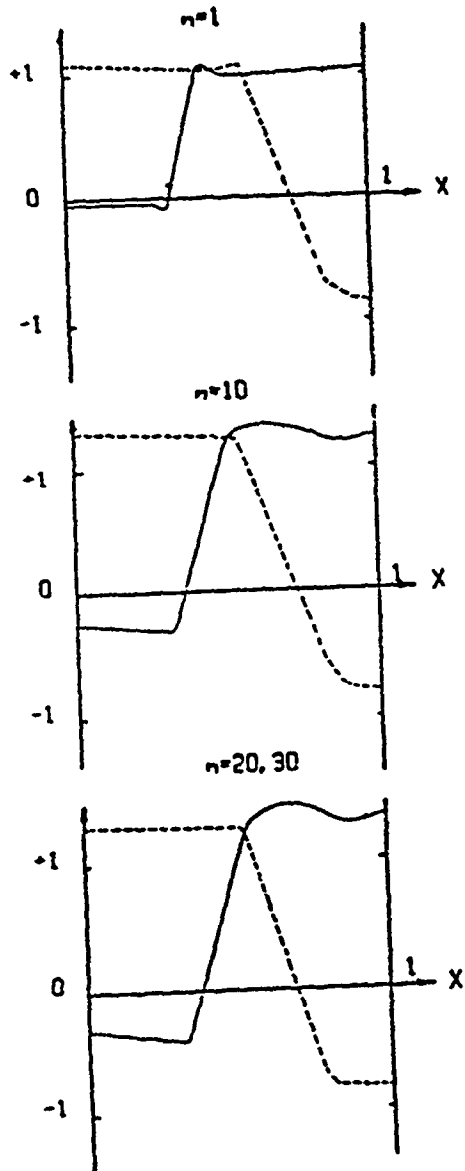


Fig. 19 Cyclic hoop stress distributions for 700 psi/167°F (K.H. - biaxial with $h = 0.328$)

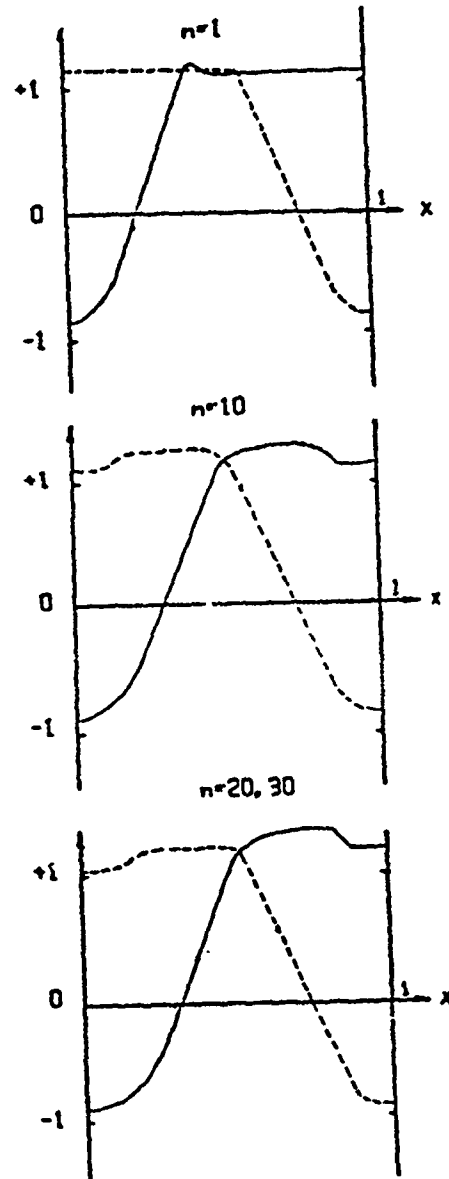


Fig. 20 Cyclic hoop stress distribution for 700 psi/167°F (K.H. - biaxial version with $h = 0$)

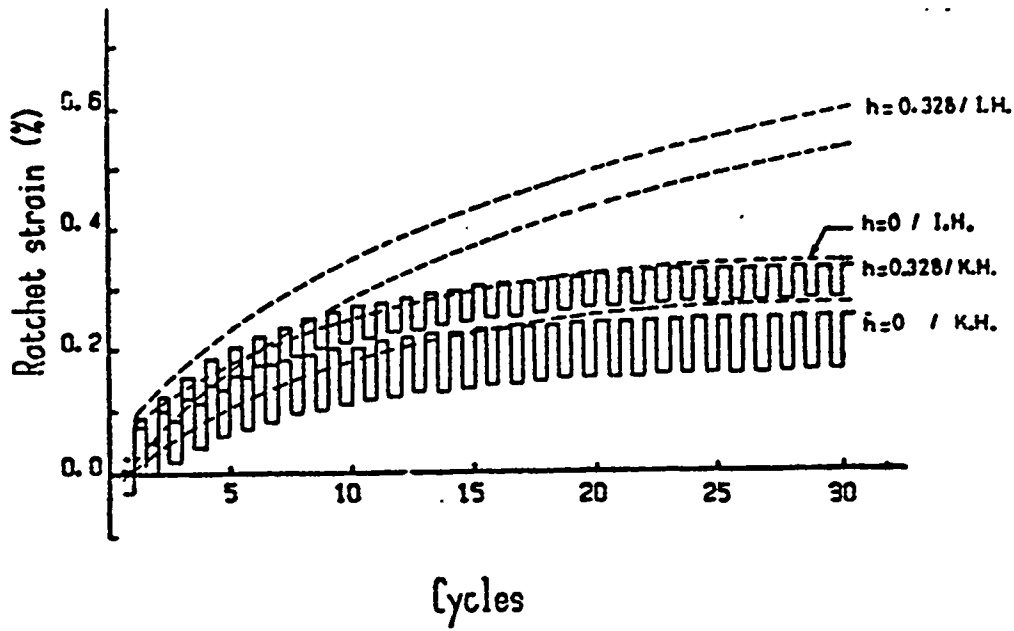


Fig. 21 Ratchet hoop strain growth for 700 psi/167°F for both K.H. and I.H. biaxial programs with $h = 0$ and 0.328

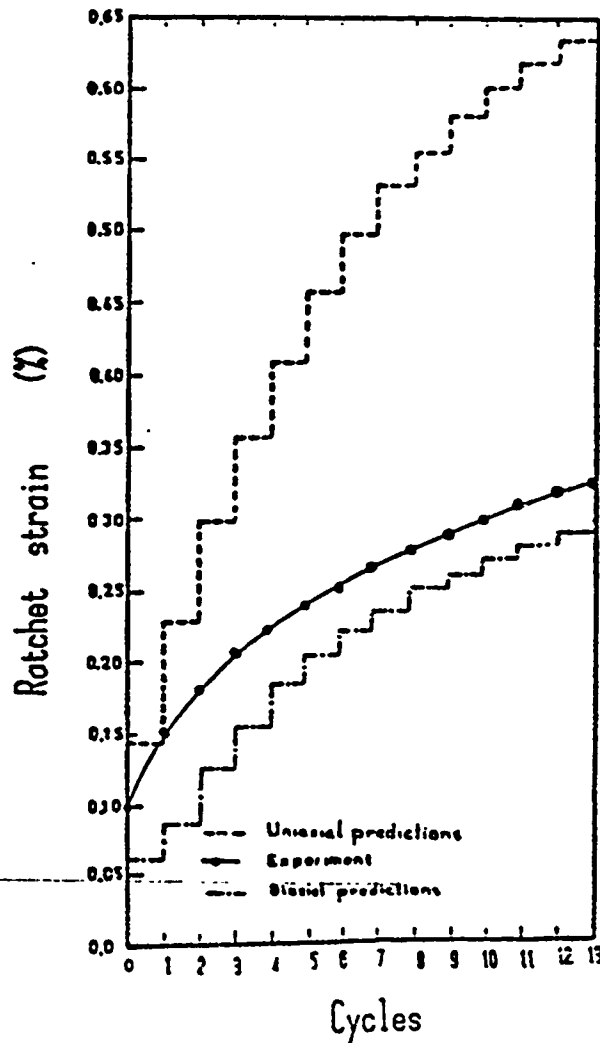


Fig. 22 Uniaxial, biaxial and experimental results for $p = 700$ psi and $\Delta T = 167^\circ F$

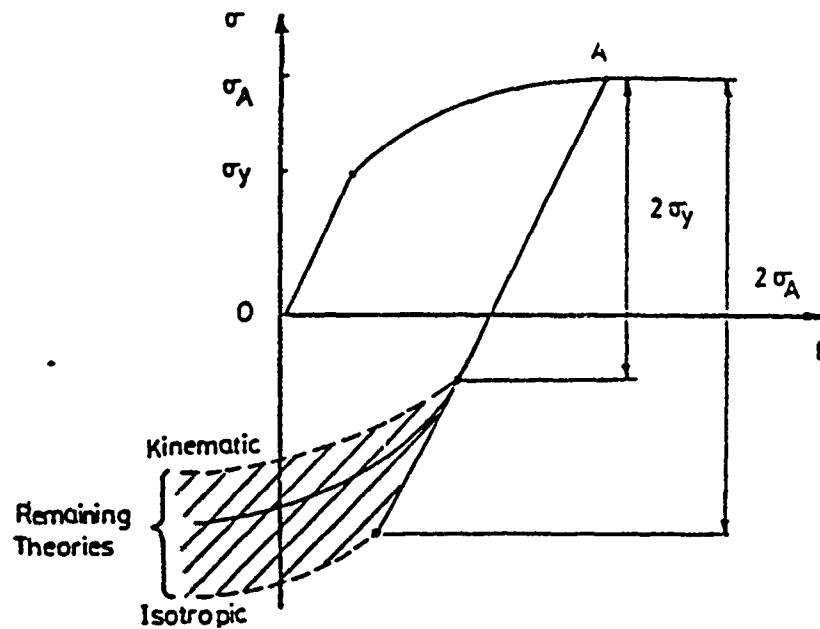


Fig. 23 Typical stress-strain curve for reversed yielding as predicted by various hardening theories

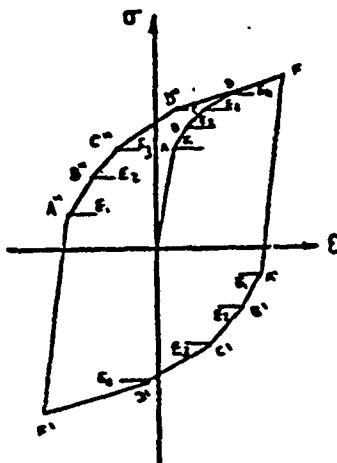


Fig. 24 Mroz's hardening (Mroz /10/)

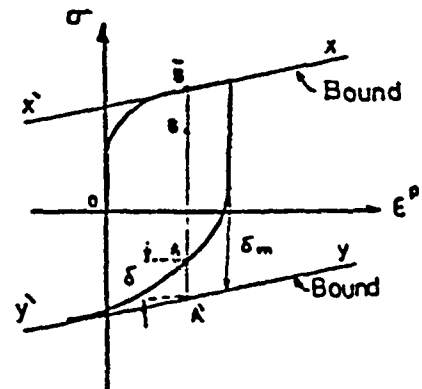


Fig. 25 Dafalias and Popov model (Dafalias and Popov /12/)